5-1-1994

Efficient Beamspace Eigen-Based Direction of Arrival Estimation schemes

Gregory M. Kautz
Purdue University School of Electrical Engineering

Michael D. Zoltowski
Purdue University School of Electrical Engineering

Efficient Beamspace Eigen-Based Direction of Arrival Estimation Schemes

Gregory M. Kautz
Michael D. Zoltowski

TR-EE 94-15
May 1994

School of Electrical Engineering
Purdue University
West Lafayette, Indiana 47907-1285

Efficient Beamspace Eigen-Based Direction of Arrival Estimation Schemes[1]

Gregory M. Kautz and Michael D. Zoltowski

School of Electrical Engineering

1285 Electrical Engineering Building

Purdue University

West Lafayette, IN 47907-1285

'This work was supported by the National Science Foundation under grant no. MIP-9320890 and by AFOSR under contract no. F49620-92-J-0198 in conjunction with Wright Laboratories.

TABLE OF CONTENTS

LIST OF FIGURES

Figure Page

ABSTRACT

The Multiple SIgnal Classification (MUSIC) algorithm developed in the late 70's was the first vector subspace approach used to accurately determine the arrival angles of signal wavefronts impinging upon an array of sensors. As facilitated by the geometry associated with the common uniform linear array of sensors, a root-based formulation was cleveloped to replace the computationally intensive spectral search process and was found to offer an enhanced resolution capability in the presence of two closely-spaced signals. Operation in beamspace, where sectors of space are individually probed via a pre-processor operating on the sensor data, was found to offer both a performance benefit and a reduced computational coinplexity resulting from the reduced data dimension associated with beamspace processing.

Little progress, however, has been made in the development of a cornputationally efficient Root-MUSIC algorithm in a beamspace setting. Two approiaches of efficiently arriving at a Root-MUSIC formulation in beamspace are developed and analyzed in this Thesis. In the first approach, a structural constraint is placed on.the beamforming vectors that can he exploited to yield a.reduced order polynomial whose roots provide information on the signal arrival angles. The second approach is considerably more general, and hence, applicable to any vector subspace angle estimation algorithm. In this approach, classical multirate digital signal processing is applied to effectively reduce the dimension of the vectors that span the signal subspace, leading to an efficient beamspace Root-MUSIC (or ESPRIT) algorithm.

An auxiliary, yet important, observation is shown to allow a real-valued eigenanalysis of the beamspace sample covariance matrix to provide a computational savings

as well as a performance benefit, particularly in the case of correlated signal scenes. A rigorous theoretical analysis, based upon derived large-sample statistics of the signal subspace eigenvectors, is included to provide insight into the operation of the two algorithmic methodologies employing the real-valued processing enhancement. Numerous simulations are presented to validate the theoretical angle bias and variance expressions as well as to assess the merit of the two beamspace approaches.

1. INTRODUCTION

A widely studied problem in radar, sonar, and seismology is the estimation of the arrival angles of wavefronts based upon measurements from an array of sensors. The most profitable techniques of signal localization are baaed upon a vector subspace approach introduced by Schmidt [11] in his MUltiple SIgnal Classification (MUSIC) algorithm. As with most vector subspace formulations **[3,** 11, 20, 23, 24], the measured covariance matrix is eigendecomposed to define two orthogonal spaces, referred to as the signal and noise subspaces. The signal subspace ideally proviides a description of the signal-induced component of the measured covariance. The determination of the arrival angles is then accomplished through the identification and localization of peaks in a spatial spectrum derived from knowledge of the noise subspace.

Root-MUSIC [1, 10] is a variation of MUSIC applicable in a uniformly-spaced, linear array (ULA) scenario that offers significant advantages over Spectral MUSIC [10]. In contrast to Spectral MUSIC, where a nonlinear search over .a one-dimensional multi-modal surface is employed to localize signals, Root-MUSIC is based on a polynomial formulation of the spectral search facilitated by the ULA structure. The rooting of a polynomial is a computational task for which there are numerically robust algorithms amenable to parallel implementation [5]. In addition to this advantage with regard to the search process, Rao and Hari [10] have shown that Root-MUSIC offers improved estimation performance over Spectral MUSIC. Although their performance analysis reveals that the asymptotic mean square error of the source angle estimates obtained with Root-MUSIC is the same as that obtained with Spectral MUSIC, Rao and Hari present simulations in which the MUSIC spectrum exhibits a single peak in the vicinity of two closely-spaced sources while the corresponcling Root-MUSIC polynomial exhibits two clearly distinct signal zeros [10].

As the computational burden of the eigenanalysis of the sensor covariance matrix increases dramatically with the number of sensors, there has been considerable interest in the use of a beamforming preprocessor to reduce the dimensionality of the data snapshot vector while simultaneously maintaining the degree of resolution associated with element space operation. In addition to the computational savings, it has been reported that the inclusion of a. properly designed beamspace preprocessor leads to a more robust estimator with regard to sensor placement perturbations and deviations from the assumed noise model, and aids in the ability to resolve two closely-spaced signals [2, 4, 6, 17, 18, 7]. Operation in parallel allows for the localization of all signals in visible space [13]. These benefits are realized at the expense of a higher MUSIC estimate variance as found in [28], but, once again, a. proper design yields an angle estimate variance in beamspace that is comparable to that obtained with element space processing [29]. The estimate bias, however, can he made smaller in beamspace formulations [29].

These observations motivate the development of a beamspace implementation of Root-MUSIC. Two computationally efficient versions of such are presented in Chapters 2 and 4. In the first approach, a. reduction in the order of the Root-MUSIC polynomial is accomplished by employing a beam set exhibiting common nulls at known locations in visible space. Tho latter approach draws on the field of multirate digital signal processing where the set of beamspace eigenvectors spanning the beamspace noise subspace are latently transformed to their element-space counterparts and decimated. Application of the standard element-space Root-MUSIC algorithm is then possible. As the approach is perfectly general in nature, extensions to include other well-known direction of arrival estimation techniques in beamspace are allowed. As such, a beamspace version of ESPRIT [24] is considered.

In conjuction with the use of these two direction of arrival estimation techniques, the impact of employing conjugate centro-symmetric beamforming vectors on the computational complexity and attainable localization accuracy is studied. The symmetry property is shown in Chapter 2 to allow a real-valued eigendecomposition to

provide valid information on the two orthogonal subspaces. A rigorous performance analysis detailing the effect of processing only the real part of the beamspace sample covariance on the bias and variance of the Spectral MUSIC estimator is contained in Chapter 3. Theoretical analyses of this sort have become increasingly popular due to the time-consuming alternative of computer simulation as well as a means to provide insight into the operation of the estimation algorithm. Kaveh and Barabell [21] were the first to employ the eigenanalysis of the (Wishart distributed) element-space sample covariance matrix to derive a theoretical expression for the resolution threshold, i.e., the minimum Signal-to-Noise (SNR) ratio at which two closely-spaced signals are resolvable, of the MUSIC and Min-Norm algorithms. Later, Lee and Wengrovitz [7] studied the resolution threshold in a beamspace MUSIC setting for a variety of beamforming architectures. Others [33, 34, 28, 29, 35, 36, 37] have extended the analysis to provide the estimate bias and variance for MUSIC as well as a number of other direction finding algorithms.

With regard to notation, vectors are represented by bold, lower-case symbols while matrices are bold, upper-case symbols. The transpose operation is indicated with a superscript "T", while "H" refers to conjugate transpose.

2. DEVELOPMENT OF BEAMSPACE ROOT-MUSIC

2.1 Introduction

To facilitate reduced computational complexity in the development of a beamspace Root-MUSIC setting, procedures are presented for designing orthogonal matrix beamformers composed of conjugate centro-symmetric weight vectors and producing beams exhibiting common out-of-band nulls. The N x N_b Discrete Fourier Transform (DFT) matrix beamformer composed of N_b columns of the N x N DFT matrix, where N is the number of elements, is employed as a prototype matrix beamformer possessing these properties. In Section **2.3,** it is shown that the common out-of-band nulls property enables one to work with a reduced degree polynomial in the final stage of Root-MUSIC. The relationship between the present work and previous work on achieving a reduced degree polynomial in a. beamspace implementation of Root-MUSIC, particularly the pioneering work of Lee and Wengrovitz in [6], is discussed in Section **2.4.** In Section **2.5,** it is shown that the conjugate centro-symmetry of the weight vectors enables one to work with the real part, of the beamspace sample covariance matrix in the eigenanalysis stage of Root-MUSIC, reducing the attendant computational complexity by a factor of four. Procedures for constructing matrix beamformers having the desired features plus additional features such a.s producing beams with reduced out-of-band sidelobes and/or common nulls a.t prescribed locations are developed in Sections 2.6 and 2.7, respectively. In Section 2.8, simulations are presented which illustrate various performance comparisons: beamspace Root-MUSIC versus element space Root-MUSIC, beamspace Root-MUSIC versus beamspace Spectral MUSIC, and reduced out-of-hand sidelobes versus in-band performance.

2.2 The Data Model

In this section, the array data model is presented. The ideal form of the sensor covariance matrix is derived and decomposed into its spectral form to illustrate the operation of the MUSIC algorithm.

The array geometry assumed is that of a uniform linear array of N identical sensors. For the sake of simplicity, the inter-element spacing is taken to be equal to one-half of the wavelength associated with the center frequency of the band of operation. The sources are assumed to be located in the far field so that planar wavefronts are perceived by the array, and all signals are assumed to be narrowband in nature. In this setting, let $\mathbf{x}(n)$ denote the N x 1 sensor space snapshot vector measured at the n-th sampling interval; $\mathbf{x}_i(n)$ denotes the i-th component of $\mathbf{x}(n)$. The response of the i-th sensor to a signal arriving at a. bearing angle θ is

$$\mathbf{x}_i(n) = \mathrm{s}(n) \exp\left(j\pi \left[I - \frac{N = \mathrm{l}}{2} \right] u \right) \qquad i = 1, ..., N \qquad [2.1]$$

where u is the direction sine, u = $sin(\theta)$ [15], and $\mathrm{s}(n)$ is the value of the complex envelope of the signal a.t the n-th sampling. Notice that the exponential term represents a time delay, with reference to the array center, to account for the wavefront motion along the axis of the array.

In the general case of K signals and additive noise, the sensor response is

$$\mathbf{x}_i(n) = \sum_{k=1}^{K} \mathrm{s}_k(n) \exp\left(j\pi \left[i - \frac{N-1}{2} \right] u_k \right) + \mathrm{n}_i(n) \qquad i = 1, ..., \mathrm{N} \qquad [2.2]$$

where the added subscript k, $k = 1, ..., K$, refers to the specific arrival, and $\mathbf{n}_i(n)$ is the value of the noise process for the i-th sensor at the n-th snapshot. The sensor space snapshot vector, $\mathbf{x}(n)$, can then *he* written as

$$\mathbf{x}(n) = [\mathbf{x}_1(n), \mathbf{x}_2(n), \ldots, \mathbf{x}_N(n)]^T = \mathbf{A}\mathbf{s}(n) + \mathrm{n}(n) \qquad [2.3]$$

where

$$\mathrm{n}(n) = [\mathbf{n}_1(n), \ldots, \mathrm{n}_N(n)]^T$$

$$\mathbf{s}(n) = [\mathbf{s}_1(n), \ldots, \mathbf{s}_K(n)]^T$$
$$\mathbf{A} = [\mathbf{a}_N(u_1) \vdots \ldots \vdots \mathbf{a}_N(u_K)]^T$$

and $\mathbf{a}_N(u)$, termed the array manifold vector, is

$$a = \left[\exp\left(-j\frac{N-1}{2}\pi u\right), \exp\left(-j\frac{N-3}{2}\pi u\right), \ldots, \exp\left(j\frac{N-1}{2}\pi u\right)\right]^T. \quad [2.4]$$

For the sake of simplicity, it is assumed that the noise process at each sensor is Gaussian in nature with zero mean and variance σ_n^2. The noise is assumed to be independent over both time and sensor space, and is uncorrelated with respect to the signals. Notice that this restriction on the noise process is not required for proper operation of the MUSIC algorithm - the MUSIC algorithm only requires that the covariance matrix of the noise be known. As a result of these assumptions, the sensor space covariance matrix, R,, is easily shown to be

$$\mathbf{R}_x = \mathbf{E}[\mathbf{x}(n)\mathbf{x}(n)^H] = \mathbf{A}\mathbf{P}_S\mathbf{A}^H + \sigma_n^2\mathbf{I} \quad [2.5]$$

where $\mathbf{P}_S$ is the signal covariance matrix

$$\mathbf{P}_S = \mathbf{E}[\mathbf{s}(n)\mathbf{s}(n)^H]. \quad [2.6]$$

Assuming that no two signals are perfectly correlated, the K x K matrix $\mathbf{P}_S$ is of full rank so that the spectral decomposition of the signal component to the sensor covariance is

$$\mathbf{A}\mathbf{P}_S\mathbf{A}^H = \sum_{k=1}^{N} \lambda_k' \mathbf{e}_k \mathbf{e}_k^H \quad [2.7]$$

where $\mathbf{e}_k$ is the k-th unit-length eigenvector associated with the k-th eigenvalue such that

$$\lambda_1' \geq \lambda_2' \geq \ldots, \lambda_K' > 0 \quad [2.8]$$
$$\lambda_{K+1}' = \lambda_{K+2}' = \ldots = \lambda_N' = 0.$$

Notice that it is inherently assumed that the number of signals is less than the number of sensors. This assumption is necessary for the operation of MUSIC. In addition,

it is easily verified that the spectral decomposition of the sensor covariance matrix contains the same eigenvectors leading to

$$\mathbf{R}_x = \sum_{k=1}^{N} \lambda_k \mathbf{e}_k \mathbf{e}_k^H \qquad [2.9]$$

where

$$\lambda_k = \lambda'_k + \sigma_n^2 \qquad k = 1, ..., N \qquad [2.10]$$

The first K eigenvectors span the same space as that of the set of signal manifold vectors since $\boldsymbol{e;}$, i $= K + 1, ..., N$, span the orthogonal subspace, i.e.,

$$\mathbf{e}_i^H \mathbf{a}_N(u_k) = 0 \quad k = 1, ..., K \quad i = K + 1, ..., N \qquad [2.11]$$

Defining the noise-only subspace a.s that formed from $\mathbf{e}_i$, $i = K + 1, ..., N$, one can construct the projection matrix, $\mathbf{P}_n$, onto the noise-only subspace a.s

$$\mathbf{P}_n = \sum_{i=K+1}^{N} \mathbf{e}_i \mathbf{e}_i^H. \qquad [2.12]$$

The MUSIC spectrum is then defined as [26]

$$\mathbf{S}_{MUSIC} = 1 / (\mathbf{a}_N^H(u) \mathbf{P}_n \mathbf{a}_N(u)). \qquad [2.13]$$

Notice that for directions u coinciding with a signal arrival angle, $u = u_k$, $k = 1, ..., K$, $\mathbf{S}_{MUSIC}(u_k) = \infty$. This property allows one to locate the directions of arrival of the various wavefronts as generated from distinct point sources. Furthermore, notice that this algorithm is intended for use in determining the arrival angles and not in estimating the spatial spectrum as is true for such algorithms as Capon's Minimum Variance or Burg's Maximum Entropy.

2.3 DFT Based Beamspace Root-MUSIC With Reduced Degree Polynomial

In this section, it is shown that if one employs DFT beamformers, the degree of the polynomial solved in the final step of MUSIC is on the order of twice the number of beams rather than twice the number of elements as in element space Root-MUSIC.

The development of this result hinges on the so-called common out-of-band nulls property exhibited by DFT beams to be discussed shortly.

The Discrete Space Fourier Transform (DSFT) [15] of the n-th N x 1 element space snapshot vector as a function of the direction sine is defined as

$$f(u\,;\,n) \;=\; \sum_{k=0}^{N-1} x_k(n)\,\exp[-jk\pi u] \qquad [2.14]$$

Note that for a fixed n, $\mathrm{f}(u\,;\,n)$ is a periodic function of u with period *2*. Typically, the magnitude and phase of $f(u\,;\,n)$ are plotted over the interval $-1 \leq u \leq 1$ corresponding to the angular interval $-90° \leq \theta \leq 90°$; this is referred to as the visible region [15]. Computation of the N-point DFT of the N x I snapshot vector, however, provides N equi-spaced samples of the DSFT over the interval $0 \leq u \leq 2$. This should be kept in mind in the following development.

Defining the N x 1 DFT beamforming weight vector as

$$\mathbf{v}_N(u) \;=\; [1,\, \exp(j\pi u)\,,\, \exp(j2\pi u)\,,\, \ldots,\, \exp(j[N-1]\pi u)]^T\,, \qquad [2.15]$$

it follows that the quantity $\mathbf{v}_N^H(u_o)\mathbf{x}(n)$ is the DSFT of the n-th snapshot evaluated at u $= u_o$. Note that $\mathbf{v}_N(u)$ exhibits a Vandermonde structure (hence the use of the boldface v). The subscript N is intended to denote the dimension of the vector.

Consider an $N \times N_b$ beamforming matrix composed of N_b DFT beamforming vectors of the form in (2.14) with respective pointing-angles equi-spaced by the amount Au $= 2/N$:

$$\mathbf{W}_R^{(m)} \;=\; \frac{1}{\sqrt{N}}\left[\mathbf{v}_N\left(m\frac{2}{N}\right) \vdots\, \mathbf{v}_N\left([m+1]\frac{2}{N}\right) \vdots\, \ldots \vdots\, \mathbf{v}_N\left([m+N_b-1]\frac{2}{N}\right)\right] \qquad [2.16]$$

It is easily ascertained that the N_b columns of $\mathbf{W}_R^{(m)}$ are N_b consecutive columns of the N x N DFT matrix, respectively. The subscript R in $\mathbf{W}_R^{(m)}$ is intended to emphasize that DFT beamforming implies (R)ectangular weighting, i.e., no tapering across the array aperture. This will serve to distinguish the DFT matrix beamformer from matrix beamformers to be examined in a later section which incorporate tapering according to one of the classical windows.

It follows that the N_b x 1 beamspace snapshot vector formed as

$$\mathbf{y}_R^{(m)}(n) = \mathbf{W}_R^{(m)H}\mathbf{x}(n) \qquad [2.17]$$

is composed of N_b successive values of the N point DFT of $\mathbf{x}(n)$. The N_b corresponding beam pointing angles, $m\frac{2}{N}$, $(m+1)\frac{2}{N}$, ..., (in $+ N_b - 1)\frac{2}{N}$, encompass a particular (spatial) sub-band of $0 \leq u \leq 2$ [12, 13] referred to as the m-th sub-band. Again, the subscript R in $\mathbf{y}_R^{(m)}(n)$ is intended to distinguish $\mathbf{y}_R^{(m)}(n)$ from alternative bearnspace snapshot vectors composed of beam outputs with tapering to be examined later. As with $\mathbf{W}_R^{(m)}$, the superscript (m) in $\mathbf{y}_R^{(m)}(n)$ is intended to denote the sub-band under examination by indexing it according to the leading DFT value.

The use of MUSIC/Root-MUSIC to estimate the bearings of sources within the m-th sub-band given M beamspace snapshots constructed a .in (2.17)is now considered. We will here concentrate on the processing of a single sub-band, the m-th sub-band. The source content in different sub-bands may be examined by choosing different sets of N_b consecutive DFT values, i.e., different values of m, computed from a single N point DFT of each snapshot. The processing in each sub-band is identical. Although it is not necessary that the number of DFT values comprising each group be the same, this serves to make the overall procedure highly motlular facilitating efficient parallel implementation [12]. It should be noted that it is important to (allowsome percentage of overlap among the sub-bands or sources may lie in between the "cracks" and go undetected. Also, a.s will be observed in the forthcoming simulations, best performance is achieved for those sources which lie at the center of the band. With 50% overlap among sub-bands, a.source at the edge of one band will lie at. the center of an adjacent sub-band [12].

For the sake of simplicity, it will be assumed that the element level noise is spatially white. Since the columns of $\mathbf{W}_R^{(m)}$ are mutually orthogonal (recall that they are N_b columns of the N x N DFT matrix), it follows that the beamspace noise covariance matrix is a scalar multiple of the N_b x N_b identity matrix. The conventional beamspace MUSIC method thus proceeds as follows. First, given M snapshots a N_b x N_b beamspace sample correlation matrix (SCM) is formed and, subsequently,

spectrally decomposed as

$$\hat{\mathbf{R}}_y^{(m)} = \frac{1}{M}\sum_{n=1}^{M} \mathbf{y}_R^{(m)}(n)\mathbf{y}_R^{(m)H}(n) = \sum_{i=1}^{N_b} \lambda_i \mathbf{e}_i \mathbf{e}_i^H \qquad (N_b \times N_b) \qquad [2.18]$$

That is, in the far right hand side of (2.18) λ_i and $\mathbf{e}_i$ represent the i-th eigenvalue and corresponding eigenvector of the beamspace SCM, i=1,...,N_b. The eigenvalues, A,, i=1,...,N_b, are assumed to he indexed in descending order with respect to magnitude. At this stage, the eigenvalues and corresponding eigenvectors are partitioned according to some criteria, such as AIC or MDL [16], into those which belong to the signal subspace and those which belong to the noise subspace. Let $\hat{K}$ denote the estimated dimension of the signal subspace. The beamspace MUSIC spatial spectral estimate is then constructed a.s

$$\begin{aligned} \mathbf{S}_{MUSIC}^{(m)}(u) &= \left\{ \mathbf{b}_R^{(m)H}(u) \sum_{i=\hat{K}+1}^{N_b} \mathbf{e}_i \mathbf{e}_i^H \mathbf{b}_R^{(m)}(u) \right\}^{-1} \\ &= \left\{ \mathbf{v}_N^H(u) \mathbf{W}_R^{(m)} \sum_{i=\hat{K}+1}^{N_b} \mathbf{e}_i \mathbf{e}_i^H \mathbf{W}_R^{(m)H} \mathbf{v}_N(u) \right\}^{-1} \end{aligned} \qquad [2.19]$$

where $\mathbf{b}_R^{(m)}(u)$ is the N_b x 1 beamspace manifold for the in-th sub-band related to the $N \times 1$ element space manifold as $\mathbf{b}_R^{(m)}(u) = \mathbf{W}_R^{(m)H}\mathbf{v}_N(u)$. The subscript R in $\mathbf{b}_R^{(m)}$(u) is intended to associate it with rectangular weighting; again, the significance will become apparent later. The relationship $\mathbf{b}_R^{(m)}(u) = \mathbf{W}_R^{(m)H}\mathbf{v}_N(u)$ is invoked in the far right-hand side of (2.19) in order to convert the spectral search into a root-finding problem a la Root-MUSIC [1, 10].

Making the substitution $z = e^{j\pi u}$ and, subsequently, exploiting the Vandermonde structure of $\mathbf{v}_N$(u), the quadratic form in brackets in the far right-hand side of (2.19) may be expressed as a polynomial of order $2N - 2$ [1, 10] as

$$p(z) = p_0 + p_1 z + \ldots + p_{N-1} z^{N-1} + \ldots + p_1^* z^{2N-3} + p_0^* z^{2N-2} \qquad [2.20]$$

where the coefficients p_j, j=0,1,...,A'-1. may be computed as sums of the elements along various diagonals of the N x N matrix

$$\mathbf{P} = \mathbf{W}_R^{(m)} \left\{ \sum_{i=\hat{K}+1}^{N_b} \mathbf{e}_i \mathbf{e}_i^H \right\} \mathbf{W}_R^{(m)H}. \qquad [2.21]$$

Specifically, denoting $\mathbf{P}(i,j)$ as the i,j element of $\mathbf{P}$, i=1,...,N, j=1,...,N,

$$p_j = \sum_{i=0}^{j} \mathbf{P}(N-j+i, i+1) \quad j = 0,1,...,N-1 \qquad [2.22]$$

Note that the coefficients of p(z) exhibit conjugate centro-symmetry, i.e., $p_j = p^*_{2N-2-j}$, $j = 0,1,...,2N-2$. As a consequence, it is easily shown that if z_i is a root of $p(z)$, then $1/z_i^*$ is a root of $p(z)$ as well. In the respective cases of either an infinite number of snapshots or no noise, the signal roots $z_k = \exp[j\pi u_k]$, k = 1,...,K, where u_k is the direction sine of the k-th source relative to the array axis, are each a root of $p(z)$ of multiplicity two [1, 10]. Ostensibly, therefore, the roots of $p(z)$ associated with sources may be extracted from the overall set of $2N$-2 roots based on their proximity to the unit circle. However, it turns out that, irrespective of the specific beamspace noise eigenvectors obtained from a give]-I set of snapshots, $p(z)$ formed according to (2.20)-(2.22) has N – N_b roots of multiplicity 2 equi-spaced on the unit circle at locations corresponding to angles outside the m-th sub-band. This claim is now substantiated and exploited to reduce the order of the polynomial to be solved from 2N – 2 to $2N_b - 2$.

Recall that each of the N_b columns of $\mathbf{W}_R^{(m)}$ is a (distinct) column of the N × N DFT matrix. Since the columns of the N x N DFT matrix are mutually orthogonal, each of the $N - N_b$ columns of the N x N DFT matrix not contained in $\mathbf{W}_R^{(m)}$ is orthogonal to each of the N_b columns of $\mathbf{W}_R^{(m)}$. Mathematically,

$$\mathbf{W}_R^{(m)H}\mathbf{v}_N(u_n) = \mathbf{0}_{N_b} \text{ for } u_n \in \left\{0, \frac{2}{N}, \ldots, (m-1)\frac{2}{N}, (m+N_b)\frac{2}{N}, \ldots, (N-1)\frac{2}{N}\right\}. \qquad [2.23]$$

This implies that for each of these $N - N_b$ values of u, which lie outside of the m-th sub-band, the quadratic form in brackets in either term on the right-hand side of (2.19) is identically zero irrespective of the measured eigendata. More importantly, (2.23) implies that $p(z)$ forinecl according to (2.20)-(2.22) has double roots at the following N – N_b locations on tlie unit circle:

$$z_n = \exp\left[j\pi n\frac{2}{N}\right] \quad n \in \{0,1,...,m-1,m+N_b,...,N-1\} \qquad [2.24]$$

These N – N_b double roots may be factored out in order to work with a polynomial of order $2N_b - 2$. This is the goal of the following development.

Consider the polynomial representation of a. single term in brackets in the far right-hand side of (2.19). Throughout the ensuing development, the index i is to be associated with the i-th eigenvectos of $\hat{\mathbf{R}}_y$ where $i \in \left\{\hat{K}+1, ..., N_b\right\}$. Denoting e_{i_k} as the k-th component of $\mathbf{e}_i$, direct substitution yields

$$\mathbf{e}_i^H \mathbf{W}_R^{(m)H} \mathbf{v}_N(u) = \sum_{k=0}^{N_b-1} e_{i_{k+1}}^* \mathbf{v}_N^H \left([m+k]\frac{2}{N}\right) \mathbf{v}_N(u). \qquad [2.25]$$

The polynomial representation of $\mathbf{e}_i^H \mathbf{W}_R^{(m)H} \mathbf{v}_N(u)$, denoted $p_i(z)$, is obtained by invoking the Vandermonde structure of $\mathbf{v}_N(u)$ and the relationship $z = \exp[j\pi u]$. This yields

$$p_i(z) = e_{i_1}^* v_m(z) + e_{i_2}^* v_{m+1}(z) + \ .. + e_{i_{N_b}}^* v_{m+N_b-1}(z) \qquad [2.26]$$

where $v_k(z)$, is the (N – 1)-th order polynomial with coefficients given by the components of $\mathbf{v}_N^*(k\frac{2}{N})$ according to

$$v_k(z) = \sum_{n=0}^{N-1} \exp\left(-j\pi n k \frac{2}{N}\right) z^n, \quad k = m, m+1, ..., m+N_b-1. \qquad [2.27]$$

The N – 1 roots of $v_k(z)$, k=m,...,m + N_b – 1, are located at $z_{n+k} = \exp\left[j\pi(k+n)\frac{2}{N}\right]$ [15], n = 1, 2, ..., N – 1, such that

$$v_k(z) = \exp\left(-j\pi(N-1)k\frac{2}{N}\right) \prod_{n=1}^{N-1} \left(z - \exp\left[j\pi(k+n)\frac{2}{N}\right]\right), \ k = m, ..., m+N_b-1. \qquad [2.28]$$

Comparing the roots of each of the N_b polynomials $v_k(z)$, k=m,m + 1,...,m + N_b – 1, it is found that they have $N - N_b$ roots in common equal to the $N - N_b$ roots listed in (2.24).

Let $c_R^{(m)}(z)$ denote the "common roots" polynomial of order N – N_b whose roots are the N – N_b common soots listed in (2.24):

$$c_R^{(m)}(z) = \prod_{n=m+N_b}^{m+N-1} \exp\left[j\pi n\frac{2}{N}\right] \prod_{n=}^{m-1} \left(z - \exp\left[j\pi n\frac{2}{N}\right]\right) \prod_{n=m+N_b} \left(z - \exp\left[j\pi n\frac{2}{N}\right]\right)$$

$$= \prod_{n=m+N_b}^{m+N-1} \exp\left[j\pi n\frac{2}{N}\right] \prod_{n=m+N_b}^{m+N-1}\left(z - \exp\left[j\pi n\frac{2}{N}\right]\right) = \sum_{i=0}^{N-N_b} c_{R_i}^{(m)*} z^i \qquad [2.29]$$

$\mathbf{c}_R^{(m)*}$ is the $(N-N_b+1)$ x 1 coefficient vector for $\mathbf{c}_R^{(m)}(z)$. Note that the constant term in $\mathbf{c}_R^{(m)}(z)$, i. e., the coefficient of z^0, is unity. It follows that $v_k(z)$ may be factored as

$$v_k(z) = q_k(z)\, c_R^{(m)}(z) \qquad k = m, m+1, ..., m+N_b-1 \qquad [2.30]$$

where $q_k(z)$ is a polynomial of order N_b-1 whose roots are those of $v_k(z)$ not included in the set of common roots listecl in (2.24):

$$q_k(z) = \frac{1}{\sqrt{N}} \prod_{\substack{n=m \\ n\neq k}}^{m+N_b-1} \exp\left(-j\pi n\frac{3}{N}\right) \prod_{\substack{n=m \\ n\neq k}}^{m+N_b-1}\left(z - \exp\left[j\pi n\frac{2}{N}\right]\right), \; k = m, ..., m+N_b-1. \qquad [2.31]$$

$\mathbf{q}_k^*$ is the N_b x 1 coefficient vector for $q_k(z)$. Note that the constant term in $\mathbf{q}_k(z)$, i.e., the coefficient of z^0, is unity.

It follows from the above observations that $p_i(z)$ may be factored as

$$p_i(z) = c_R^{(m)}(z) \cdot \left\{e_{i_1}^* q_m(z) + e_{i_2}^* q_{m+1}(z) + \ldots + e_{i_{N_b}}^* q_{m+N_b-1}(z)\right\} = c_R^{(m)}(z)\, r_i(z). \qquad [2.32]$$

where $r_i(z)$ is the (N_b-1)-th order polynomial within brackets as implied. The roots of $r_i(z)$ are the roots of interest. The N_b x 1 coefficient vector for $r_i(z)$, rf, may be expressed as a simple transformation on the i-th beamspace noise eigenvector $\mathbf{e}_i$. To this end, define $\mathbf{Q}_R^{(m)}$ as a $N_b \times N_b$ matrix for which each column is the coefficient vector for one of the N_b polynomials defined in (2.31):

$$\mathbf{Q}_R^{(m)} = \left[\mathbf{q}_m \vdots \mathbf{q}_{m+1} \vdots \ldots \vdots \mathbf{q}_{m+N_b-1}\right] \qquad [2.33]$$

It follows from ***(2.32)*** that the coefficient vector for $r_i(z)$ may be expressed in compact form as

$$\mathbf{r}_i = \mathbf{Q}_R^{(m)}\mathbf{e}_i \qquad [2.34]$$

Equation ***(2.34)*** implies that we need only modify each of the beamspace noise eigenvectors by the transformation $\mathbf{Q}_R^{(m)}$ prior to forming a beamspace Root-MUSIC polynomial of order $2N_b-2$ in the usual fashion. That is, defining the N_b x N_b matrix

$\mathbf{P}_R^{(m)}$ as

$$\mathbf{P}_R^{(m)} = \mathbf{Q}_R^{(m)} \sum_{i=K+1}^{N_b} \mathbf{e}_i \mathbf{e}_i^H \mathbf{Q}_R^{(m)H} \qquad [2.35]$$

the beamspace Root-MUSIC polynomial of order $2N_b - 2$ for the m-th sub-band is constructed as

$$p^{(m)}(z) = p_0 + p_1 z + \ldots + p_{N_b-1} z^{N_b-1} + \ldots + p_1^* z^{2N_b-3} + p_0^* z^{2N_b-2} \qquad [2.36]$$

where the coefficients are computed in terms of the elements of $\mathbf{P}_R^{(m)}$ in *(2.35)* according to

$$p_j = \sum_{i=0}^{j} \mathbf{P}_R^{(m)}(N_b - j + i, i + 1) \quad j = 0, 1, \ldots, N_b - 1 \qquad [2.37]$$

Note that this mode of operation docs not, require one to clivide the common roots polynomial, $c_R^{(m)}(z)$,in *(2.29)* out of the $(2N-2)$-th order polynomial constructed according to *(2.20)-(2.22)*. The latter polynomial is never formed. Once the beamspace noise eigenvectors are determined, the relevant beamspace Root-MUSIC polynomial of order $2N_b - 2$ is simply constructed according to *(2.35)-(2.37)*.

The property in *(2.23)* was critical to the reduction in polynomial.order from $2N-2$ to $2N_b - 2$. Equation *(2.23)* implies that the N_b DFT beams formed to encompaas the m-th sub-band have $N - N_b$ nulls in common outside the m-th sub-band. The N_b DFT beams are thus said to possess the common out-of-band nulls property. As an illustrative example, Figure 2.1 (a) displays $N_b = 8$ DFT beams encompassing the null-to-null sub-band $-10/N < u < 8/N$ for an $N = 32$ uniform linear array. These were generated from $N_b = 8$ contiguous columns of the 32x32 DFT matrix (allowing for wrap-around in the use of the word "contiguous"). The common out-of-band nulls property is apparent: the beams have $N - N_b = 32 - 8 = 24$ out-of-band nulls in common. Figure 2.1(b) displays the roots of the Root-MUSIC polynomial of order $2N - 2 = 62$ formed according *to (2.20)-(2.22)*with $K = 0$ corresponding to the no source case. In agreement with the preceding development, the $N - N_b = 24$ common out-of-band nulls in Figure 2.1(a) translate into $N - N_b = 24$ roots of multiplicity 2 lying equi-spaced on the unit circle outside the region corresponding to the sub-band.

The beam set in Figure 2.1(a) is employed in the simulations to be presented in a forthcoming section.

Before leaving this section, an important observation is made with regard to the computation of $\mathbf{Q}_R^{(m)}$. Each column of $\mathbf{Q}_R^{(m)}$ is the coefficient vector for a $(N_b - 1)$-th order polynomial having one of the N_b root factorizations in (2.31). Note that there is no need to ever form $\mathbf{C}_R^{(m)}$. For each $q_k(z)$, $k = m, m+1, ..., m+N_b-1$, the locations of the roots are coinpletely specified by the starting DFT point for the sub-band, m, the number of beams N_b, and the number of elements, N. Ostensibly, one can use any algorithm at one's disposal that takes a set of roots and provides the coefficients of the polynomial having these roots. However, for even moderately large values of N, N = 48 for example, the roots arc close enough on the unit circle such that one needs to be concerned about the numerical sensitivity of the algorithm used to determine the corresponding polynomial coefficients. In Appendix A, a. procedure is developed for computing $\mathbf{Q}_R^{(m)}$ that avoids polynomial determination entirely and is less sensitive to the condition number of $\mathbf{Q}_R^{(m)}$. This yields the following expression for $\mathbf{Q}_R^{(m)}$ for the case where N/N_b is an integer.

$$\mathbf{Q}_R^{(m)} = \gamma_m \mathbf{D}\, \mathbf{W}_{N_b}^{*}\, \mathbf{G} \quad \text{where for } i = 1,2,...,N_b\ ,\ k = 1,2,...,N_b: \qquad [2.38]$$

$$\mathbf{D}(i,k) = \exp\left[j\pi \frac{N_b - 1}{N}\left\{i - \frac{N_b + 1}{2}\right\}\right]\ \delta_{ik}$$

$$\mathbf{G}(i,k) = \frac{(-2)^{N_b-1}(-1)^{k-i}}{N_b} \exp\left[j(i-1)\frac{\pi}{N_b}\right] \left\{ \prod_{\substack{n=0 \\ n\neq k-1}}^{N_b-1} \sin\left[\frac{\pi}{2}\left(\frac{N_b - 1}{N} + \frac{2(i-1)}{N_b} - \frac{2(n+m)}{N}\right)\right]\right\}$$

$\mathbf{W}_{N_b}$ denotes the N_b point DFT matrix, a N_b x N_b orthogonal matrix, and δ_{ik} denotes the Kronecker delta such that D is a N_b x N_b diagonal matrix. Also, γ_m is a scalar defined in (A.8) of Appendix A. The expression for γ_m is not repeated here since γ_m has unity magnitude and will thus have no influence on the computation of $\mathbf{P}_R^{(m)}$ according to (2.35)-(2.37). One may thus set γ_m equal to unity. As a final note, with regard to parallelization, it is pointed out that all the sub-hands may be processed

using the same $\mathbf{Q}_R^{(m)}$, i.e., with m set to a particular value such as $m = 0$, for example, provided one translates the angle estimates a.-posteriori to the appropriate sub-band.

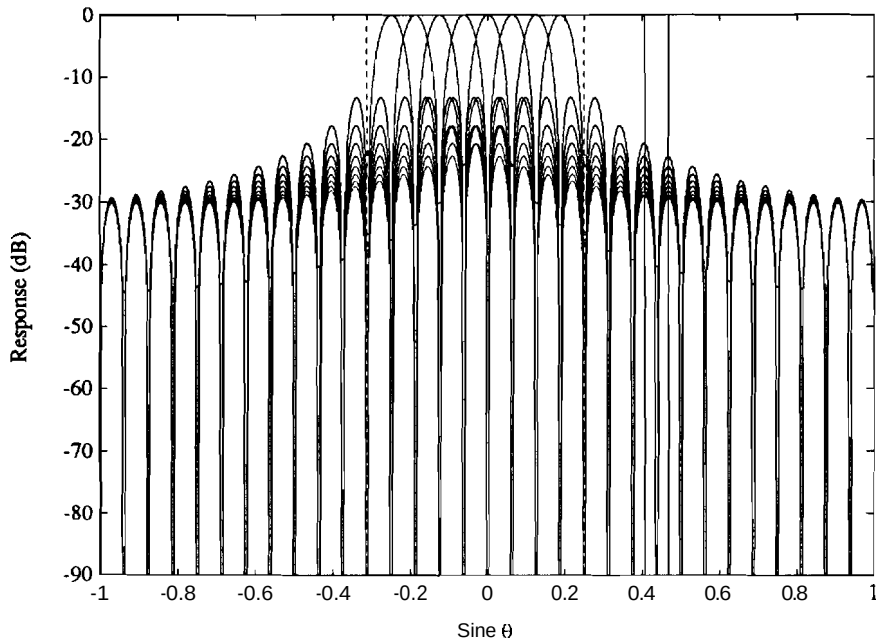

(a)

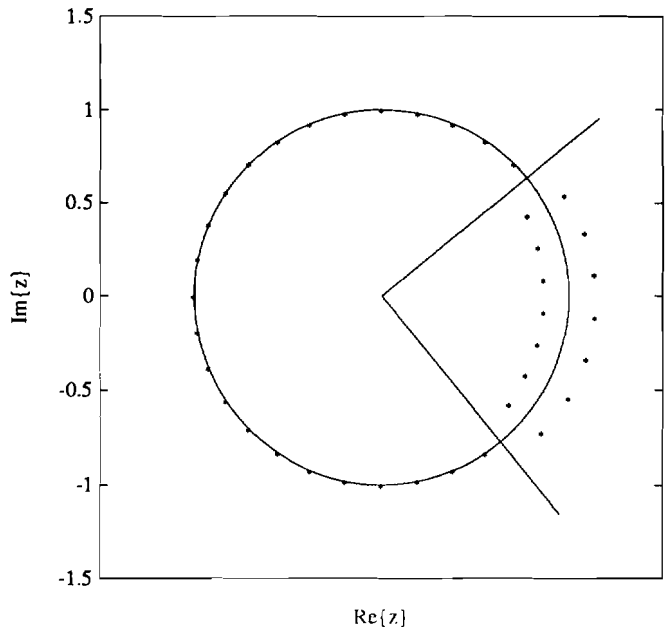

(b)

Figure 2.1 (a) $N_b = 8$ unweighted spatial DFT beams for N=32 element ULA; beams encompass the null-to-null subband $-10/N < u < 8/N$. (Is) Roots of beamspace Root-MUSIC polynomial in no source case.

2.4 Previous Beamforming Methods to Achieve Reduced Degree Polynomial

As the coefficient sequence for a given $v_k(z)$ in (2.30) is just the components of a particular column of $\mathbf{W}_R^{(m)*}$, the polynomial product on the right-hand side of (2.30) dictates that each column of $\mathbf{W}_R^{(m)*}$ is the linear convolution of the coefficient sequence of the corresponding in-band roots polynomial $q_k(z)$ with that of the common out-of-band roots polynomial $c_R^{(m)}(z)$. It follows, therefore, that $\mathbf{W}_R^{(m)}$ may be factored as

$$\mathbf{W}_R^{(m)} = \mathbf{C}_R^{(m)}\mathbf{Q}_R^{(m)} \qquad [2.39]$$

where $\mathbf{Q}_R^{(m)}$ is defined in (2.33) and $\mathbf{C}_R^{(m)}$ is the N x N_b banded, Toeplitz matrix

$$\mathbf{C}_R^{(m)} = \begin{bmatrix} c_{R_0}^{(m)} & 0 & 0 \\ c_{R_1}^{(m)} & c_{R_0}^{(m)} & 0 \\ & & \vdots \\ c_{R_{N-N_b}}^{(m)} & c_{R_{N-N_b-1}}^{(m)} & 0 \\ 0 & c_{R_{N-N_b}}^{(m)} & 0 \\ 0 & 0 & c_{R_0}^{(m)} \\ \vdots & \vdots & \vdots \\ 0 & 0 & c_{R_{N-N_b}}^{(m)} \end{bmatrix} \qquad [2.40]$$

The factorization in (2.39)-(2.40) reveals that the N x N_b DFT matrix beamformer $\mathbf{W}_R^{(m)}$ is similar in structure to the orthogonal matrix beamformers studied by Lee and Wengrovitz in [6]. Lee and Wengrovitz worked with matrix beamformers which may be factored as

$$\mathbf{W} = \mathbf{C}(\mathbf{C}^H\mathbf{C})^{-\frac{1}{2}} \qquad (N \text{ x } N_b) \qquad [2.41]$$

where C exhibits a banded-Toeplitz structure similar to that of $\mathbf{C}_R^{(m)}$ in (2.40):

$$\mathbf{C} = \begin{bmatrix} c_0 & 0 & & 0 \\ c_1 & c_0 & & 0 \\ \vdots & \vdots & \cdot & \vdots \\ c_{N-N_b} & c_{N-N_b-1} & \cdot & 0 \\ 0 & c_{N-N_b} & \cdot & 0 \\ \vdots & \vdots & & \vdots \\ 0 & 0 & & c_{N-N_b} \end{bmatrix} \qquad (N \times N_b) \qquad [2.42]$$

As will be shown shortly, the N x N_b DFT matrix beamformer, $\mathbf{W}_R^{(m)}$, is not. a member of this class of matrix beamformers. However, $\mathbf{W}_R^{(m)}$ may be rotated via a unitary transformation into a member of such. Notwithstanding, similar to the end result in the previous section, Lee and Wengrovitz in [6] showed that a reduced degree Root-MUSIC polynomial, of order $2N_b - 2$, may be achieved employing a mennber of the class of matrix beamformers described by (2.41)-(2.42).

However, the derivation of this result by Lee and Wengrovitz [6] is quite different from that in the previous section for the case of the N x N_b DFT matrix beamformer, $\mathbf{W}_R^{(m)}$. Their derivation is based on decomposing the element space to beamspace transformation $\mathrm{W^H} = (\mathbf{C}^H\mathbf{C})^{-\frac{1}{2}}\mathbf{C}^H$ into the $N_b \times N$ transformation $\mathrm{C^H}$ followed by the N_b x N_b transformation $(\mathbf{C}^H\mathbf{C})^{-\frac{1}{2}}$ and observing that

$$\mathbf{C}^H\mathbf{v}_N(u) = \left\{\mathbf{c}^H\mathbf{v}_{N-N_b+1}(u)\right\}\mathbf{v}_{N_b}(u) \qquad [2.43]$$

where $\boldsymbol{c}$ is defined relative to the elements of C in (2.42) as $\mathrm{c} = [c_0, c_1, \ldots, c_{N-N_b}]^T$ and $\mathbf{v}_{N-N_b+1}(u)$ and $\mathrm{v}_{N_b}(u)$ are defined by (2.15) with N replaced by $\mathrm{N} - N_b + 1$ and N_b, respectively. The right-hand side of (2.43) follows from the banded-Toeplitz structure of C in (2.42) and the Vandermonde structure of $\mathbf{v}_N(u)$ in (2.15). Equation (2.43) states that the beamspace manifold achieved employing the matrix beamformer C alone is a scalar multiple of the N_b x 1 Vandermonde vector $\mathrm{v}_{N_b}(u)$. As a consequence, the beamspace manifold achieved employing the orthogonalized beamformer W in

(2.41) is a scalar multiple of $(\mathbf{C}^H\mathbf{C})^{-\frac{1}{2}}\mathbf{v}_{N_b}(u)$. The reciprocal of the MUSIC spectrum may therefore be expressed as $\mathbf{v}_{N_b}^H(u)\left\{(\mathbf{C}^H\mathbf{C})^{-\frac{1}{2}}\sum_{i=K+1}^{N_b}\mathbf{e}_i\mathbf{e}_i^H(\mathbf{C}^H\mathbf{C})^{-\frac{1}{2}}\right\}\mathbf{v}_{N_b}(u)$ which is easily converted into a polynomial of order $2N_b-2$ similar to the development leading to (2.35)-(2.37).

Zoltowski [18] also studied beamforming matrices of the form described by (2.41)-(2.42) for use in conjunction with a beamspace version of the Iterative Quadratic Maximum Likelihood (IQML) Method of Bresler and Macovski [3]. The property in (2.43), also observed by Zoltowski in [18], is critical to the applicability of IQML in beamspace as IQML is a polynomial based version of the Deterministic ML method. Both Zoltowski [18] and Lee and Wengrovitz [6] note that application of the matrix beamformer $\mathrm{C^H}$ to the elemental data is equivalent to applying the $(\mathrm{N}-N_b+1)\times 1$ beamforming weight vector c to each of N_b identical, overlapping subarrays. Bienvenu and Kopp [2] also consider this type of element, space to beamspace transformation in which beams pointed to the same angle are formed at a. number of identical, overlapping subarrays. Zoltowski [18] points out that the scalar $\mathbf{c}^H\mathbf{v}_{N-N_b+1}(u)$ in (2.43) represents a multiplicative gain factor induced on a. signal arriving from the direction u; $\mathrm{c^H}\mathbf{v}_{N-N_b+1}(u)$ is the beam response associated with the weight vector c at any subarray as a function of u. Bienvenu and Kopp [2], Zoltowski [18], and Lee and Wengrovitz [6] all note that due to the overlap between subarrays, the noise components amongst the N_b beams arc correlated; the $N_b \times N_b$ beamspace noise correlation matrix is a scalar multiple of $\mathbf{C}^H\mathbf{C}$. The $N_b \times N_b$ transformation $(\mathbf{C}^H\mathbf{C})^{-\frac{1}{2}}$ may thus be interpreted as a whitening filter.

Comparing the factorization of $\mathbf{W}_R^{(m)}$ in (2.39) with the factorization of the matrix beamformers studied by Lee and Wengrovitz [6] and Zoltowski [18] in (2.41)-(2.42), one is tempted to associate $(\mathbf{C}^H\mathbf{C})^{-\frac{1}{2}}$ with $\mathbf{Q}_R^{(m)}$ as well as $\mathbf{C}$ with $\mathbf{C}_R^{(m)}$. However, $\mathbf{Q}_R^{(m)} \neq (\mathbf{C}^H\mathbf{C})^{-\frac{1}{2}}$ since $(\mathbf{C}^H\mathbf{C})^{-\frac{1}{2}}$ is Hermitian symmetric while $\mathbf{Q}_R^{(m)}$, defined by (2.31) and (2.33), is not, in general. Thus, $\mathbf{W} = \mathbf{C}_R^{(m)}(\mathbf{C}_R^{(m)H}\mathbf{C}_R^{(m)})^{-\frac{1}{2}}$ is not equal to $\mathbf{W}_R^{(m)} = \mathbf{C}_R^{(m)}\mathbf{Q}_R^{(m)}$, in general. All that can be said is that one is related to the other

via a N_b x N_b unitary transformation since the two have the same N_b-dimensional range space.

The above discussion prompts the consideration of a more general class of orthogonal beamforming matrices exhibiting the common out-of-band nulls property described by

$$\mathbf{W} = \mathbf{C}(\mathbf{C}^H\mathbf{C})^{-\frac{1}{2}}\mathbf{U} \quad (N \times (N_b - J)) \qquad [2.44]$$

where C is N $\times$ N_b exhibiting the banded-Toeplitz structure in (2.42) and U is N_b x $(N_b - \mathbf{J})$, where $0 \leq J \leq N_b - 1$, composed of $N_b - J$ orthogonal columns, i. e.,

$$\mathbf{U}^H\mathbf{U} = \mathbf{I}_{N_b - J} \qquad [2.45]$$

Note that the number of beams formed with a member of this class of matrix beamformers is $N_b' = N_b - J$, where $0 < J < N_b - 1$. The number of common nulls amongst the $N_b' = N_b - J$ beams is $N - N_b = N - (N_b - J) - J = \mathrm{N} - N_b' - J$. Thus, in general, the number of common nulls may be less than the number of elements minus the number of beams formed. This is in contrast to the class of matrix beamformers described by (2.41)-(2.42) for which the number of common nulls is always the maximum amount equal to the number of elements minus the number of beams formed. Matrix beamformers described by (2.44) for which U is not square arise naturally in beamforming scenarios where tapering is employed to achieve low sidelobes. This issue will be addressed shortly.

2.5 Real Covariance Matrix Processing in Beamspace

In this section, it is shown that through proper scaling of the N_b DFT values corresponding to a given sub-band, the eigenanalysis may he restricted to that of the real part of the beamspace sample covariance matrix, $\mathcal{R}e\{\hat{\mathbf{R}}_y\}$. To this end, in the narrowband signal model let the phase of each arriving signal be referenced to the center of the array. In this case, the expected value of the element space sample

covariance matrix may be expressed as

$$\mathbf{R}_x = \mathcal{E}\{\hat{\mathbf{R}}_x\} = \mathcal{E}\left\{\frac{1}{M}\sum_{n=1}^{M} \mathbf{x}(n)\mathbf{x}^H(n)\right\} = \mathbf{A}\mathbf{P}_S\mathbf{A}^H + \sigma_n^2\mathbf{I}_N \qquad [2.46]$$

where $\mathbf{A}$ is the NxK Direction-of-Arrival (DOA) matrix associated with the K signal arrivals,

$$\mathbf{A} = \left[\mathbf{a}_N(u_1) \vdots \mathbf{a}_N(u_2) \vdots \ldots \vdots \mathbf{a}_N(u_K)\right] \qquad [2.47]$$

with columns defined by the N x 1 array manifold

$$\mathbf{a}_N(u) = \left[\exp\left(-j\frac{N-1}{2}\pi u\right), \exp\left(-j\frac{N-3}{2}\pi u\right), \ldots, \exp\left(j\frac{N-1}{2}\pi u\right)\right]^T \qquad [2.48]$$

$\mathbf{P}_S$ in *(2.46)* is the KxK source covariance matrix. Also, σ_n^2 is the noise power at each element; recall that the element noise is assumed to bc spatially white.

Note that $\mathbf{a}_N(u)$ in (2.48) exhibits conjugate centro-symmetry. Mathematically, $\tilde{\mathbf{I}}_N\mathbf{a}_N(u) = \mathbf{a}_N^*(u)$ where $\mathbf{I}_N$ is the NxN reverse permutation matrix

$$\tilde{\mathbf{I}}_N = \begin{bmatrix} 0 & 0 & & 1 \\ 0 & 0 & & 0 \\ \vdots & \vdots & & \vdots \\ 0 & 1 & \cdot & 0 \\ 1 & 0 & & 0 \end{bmatrix} \qquad [2.49]$$

Note that $\tilde{\mathbf{I}}_N\tilde{\mathbf{I}}_N = \mathbf{I}_N$; this property will be exploited a number of times in this section. Finally, note that $\mathbf{a}_N(u)$ and the *DFT* beamforming vector $\mathbf{v}_N(u)$ in *(2.15)* are related as

$$\mathbf{a}_N(u) = \exp\left(-j\frac{N-1}{2}\pi u\right)\mathbf{v}_N(u). \qquad [2.50]$$

With these observations in mind, define the conjugate ccntro-symmetric form of the N x N_b DFT matrix as

$$\tilde{\mathbf{W}}_R^{(m)} = \frac{1}{\sqrt{N}}\left[\mathbf{a}_N\left(m\frac{2}{N}\right) \vdots \mathbf{a}_N\left([m+1]\frac{2}{N}\right) \vdots \ldots \vdots \mathbf{a}_N\left([m+N_b-1]\frac{2}{N}\right)\right]. \qquad [2.51]$$

It follows from the relationship in (2.50) that the Vandermonde and conjugate centro-symmetric forms of the N x N_b DFT matrix beamformer are related through a diagonal

unitary matrix as

$$\check{\mathbf{W}}_R^{(m)} = \mathbf{W}_R^{(m)}\mathbf{\Phi} \qquad [2.52]$$

where

$$\mathbf{\Phi} = (-1)^{\cdot\cdot}\mathrm{diag}\left\{\exp\left(\frac{jm\pi}{N}\right), \ldots, (-1)^{N_b-1}\exp\left(\frac{j(m+N_b-1)\pi}{N}\right)\right\}. \qquad [2.53]$$

If beams are computed via an N point DFT, the elements of $\mathbf{\Phi}$ represent the scalings to be applied to the N_b DFT values corresponding to the m-th sub-band in order to retroactively achieve beamforming with the conjugate centro-symmetric form of the $\mathrm{N} \times N_b$ DFT matrix beamformer.

Now, consider the expected value of the beamspace sample covariance matrix employing the conjugate centro-symmetric form of the $N \times N_b$ DFT matrix, $\tilde{\mathbf{W}}_R^{(m)}$,

$$\tilde{\mathbf{R}}_y = \mathcal{E}\left\{\frac{1}{M}\sum_{n=1}^{M}\tilde{\mathbf{y}}_R^{(m)}(n)\tilde{\mathbf{y}}_R^{(m)H}(n)\right\} = \check{\mathbf{W}}_R^{(m)H}\mathbf{R}_y\check{\mathbf{W}}_R^{(m)} = \mathbf{B}^{(m)}\mathbf{P}_S\mathbf{B}^{(m)T} + \sigma_n^2\mathbf{I}_{N_b}, \qquad [2.54]$$

where $\mathbf{B}^{(m)}$ is the DOA matrix associated with the m-th sub-band

$$\mathbf{B}^{(m)} = \tilde{\mathbf{W}}_R^{(m)H}\mathbf{A} = \left[\tilde{\mathrm{b}}_R^{(m)}(u_1) \vdots \tilde{\mathrm{b}}_R^{(m)}(u_2) \vdots \ldots \vdots \tilde{\mathrm{b}}_R^{(m)}(u_K)\right]. \qquad [2.55]$$

The most important observation of this section is that $\mathbf{B}^{(m)}$ is a real-valued matrix since

$$\mathbf{B}^{(m)} = \tilde{\mathbf{W}}_R^{(m)H}\mathbf{A} = \tilde{\mathbf{W}}_R^{(m)H}\tilde{\mathbf{I}}_N\tilde{\mathbf{I}}_N\mathbf{A} = \check{\mathbf{W}}_R^{(m)T}\mathbf{A}^* = \mathbf{B}^{(m)*} \qquad [2.56]$$

where the conjugate centro-symmetry of the columns of $\check{\mathbf{W}}_R$ and A has been exploited, and the fact that $\tilde{\mathbf{I}}_N\tilde{\mathbf{I}}_N = \mathbf{I}_N$. As a consequence, the expected value of the real part of the beamspace sample covariance matrix may be expressed as;

$$\mathcal{R}e\{\tilde{\mathbf{R}}_y\} = \mathbf{B}^{(m)}\mathcal{R}e\{\mathbf{P}_S\}\mathbf{B}^{(m)T} + \sigma_n^2\mathbf{I}_{N_b}. \qquad [2.57]$$

Note that if $\mathbf{P}_S$ is positive definite, then $\mathrm{Re}\{\mathbf{P}_S\}$ is positive definite as well; the proof of this very straightforward and thus not included here. Thus, assuming the number of sources, K, to be less than the number of beams, N_b, and that no two sources are 100% correlated, the signal-only component of $\mathcal{R}e\{\tilde{\mathbf{R}}_y\}$ in (2.57), $\mathbf{B}^{(m)}\mathcal{R}e\{\mathbf{P}_S\}\mathbf{B}^{(m)}$, is

positive semi-definiteof rank K with a range space equal to the span of the K columns of $\mathbf{B}^{(m)}$. σ_n^2 is then the smallest eigenvalue of $\mathcal{R}e\{\tilde{\mathbf{R}}_y\} = \mathbf{B}^{(m)}\mathcal{R}e\{\mathbf{P}_S\}\mathbf{B}^{(m)T} + \sigma_n^2\mathbf{I}_{N_b}$ of multiplicity $N_b - K$ and the corresponding eigenspace is the orthogonal complement of the range space of $\mathbf{B}^{(m)}$. Denoting $\mathbf{e}_i$, $i = K + 1, \ldots, N_b$, as a.n orthonormal basis for the noise subspace, it follows that $\mathbf{e}_i^H \mathbf{b}_R^{(m)}(u_i) = 0$, i=1,...,$K$. $\mathcal{R}e\{\tilde{\mathbf{R}}_y\}$ thus possesses the asymptotic structure that is a prerequisite for the applicability of the MUSIC algorithm.

Interestingly, the process of taking the real part of the sample covariance matrix in beamspace is equivalent to having first performed a single forward-backward average in element space prior to transforming to beamspace. This claim is substantiated by the following sequence of manipulations.

$$\mathcal{R}e\{\hat{\tilde{\mathbf{R}}}_y\} = \frac{1}{2}\left\{\hat{\tilde{\mathbf{R}}}_y + \hat{\tilde{\mathbf{R}}}_y^*\right\} = \frac{1}{2}\left\{\tilde{\mathbf{W}}_R^{(m)H}\hat{\mathbf{R}}_x\tilde{\mathbf{W}}_R^{(m)} + \tilde{\mathbf{W}}_R^{(m)T}\check{\mathbf{I}}_N\check{\mathbf{I}}_N\hat{\mathbf{R}}_x^*\check{\mathbf{I}}_N\check{\mathbf{I}}_N\tilde{\mathbf{W}}_R^{(m)*}\right\}$$

$$= \tilde{\mathbf{W}}_R^{(m)H}\frac{1}{2}\left\{\hat{\mathbf{R}}_x + \check{\mathbf{I}}_N\hat{\mathbf{R}}_x^*\check{\mathbf{I}}_N\right\}\tilde{\mathbf{W}}_R^{(m)} = \tilde{\mathbf{W}}_R^{(m)H}\hat{\mathbf{R}}_x^{fb}\tilde{\mathbf{W}}_R^{(m)} \qquad [2.58]$$

where $\hat{\mathbf{R}}_x^{fb} = 1/2\{\hat{\mathbf{R}}_x + \check{\mathbf{I}}_N\hat{\mathbf{R}}_x^*\check{\mathbf{I}}_N\}$ is the single forward-backward averaged sample covariance matrix in element space studied by Pillai and Kwon [8], among others. Pillai and Kwon [8] show that in the case of uncorrelated sources performing a single forward-backward average in element space has the effect of reducing the asymptotic bias of the signal eigenvectors by a factor of two; the forward-backward average has the effect of artificially doubling the number of snapshots, M. Similarly, in Appendix C it is shown that in the case of uncorrelated Gaussian sources, the real part of the beamspace sample covariance matrix is Wishart distributed with $2M$ degrees of freedom whereas the beamspace sample covariance matrix itself is complex Wishart distributed with M degrees of freedom. Thus, the snapshot doubling effect may be obtained in beamspace by simply working with the real part of the beamspace sample covariance matrix – no forward-backward average at the element level prior to beamforming is necessary!

The efficacy of working with the real part of the beamspace sample covariance matrix depends solely on the conjugate centro-symmetry of each of the columns of the

matrix beamformer. Note that the matrix beamformer structure described by (2.44)-**(2.45)** does not guarantee conjugate centro-symmetry of the respective columns. For the remainder of the chapter, attention is restricted to the use of conjugate centro-symmetric matrix beamformers so that one may work solely with the real part of the beamspace sample covariance matrix. With regard to the N x N_b DFT matrix beamformer, the tilde used to denote the conjugate centro-symmetric form will be dropped. If the beam outputs are computed via. an N point DFT, it is assumed that the N_b DFT values corresponding to the m-th sub-band have been scaled in accordance with (2.52). This dictates that in the construction of $\mathbf{Q}_R^{(m)}$, each of the polynomials $q_k(z)$, k = m,m + 1, ..., m + N_b – 1, be scaled so that the corresponding coefficient vector exhibit conjugate centro-symmetry. This is possible since in each case the roots lie on the unit circle. Under this condition, $\grave{\mathbf{I}}_{N_b}\mathbf{Q}_R^{(m)} = \mathbf{Q}_R^{(m)*}$. This property will be assumed in the remainder of the chapter and is already accounted for in the expression for $\mathbf{Q}_R^{(m)}$ in (2.38).

2.6 Virtual Tapering

The beamforming operation de-emphasizes out-of-band sources. Ideally, the contributions to the beamspace snapshot vector due to out-of-band sources are negligible. However, the common out-of-band nulls property leads to common peak sidelobe locations amongst the beams outside the band. This is depicted in Figure 2.1 for the case of $N_b = 8$ DFT beams with A' = 32. Note that as a consequence of the inherent rectangular weighting, for each beam the sidelobe peaks start at -13.5 dl3 and only roll off to a minimum of approximately -30 dB. It is thus deduced that strong sources lying at or near a common sidelobe peak location within several beamwidths of either edge of the band may not be sufficiently de-emphasized to be negligible. This is particularly true if the in-band sources are closely-spaced and/or highly correlated. Under such conditions, it is difficult to distinguish between small signal eigenvalues due to the close spacing and/or high correlation amongst the in-band sources, and small signal eigenvalues clue to to partially filtered out-of-band sources.

Consider the following theorem.

Theorem 1. The beamspace manifold, $\mathbf{b}_R^{(m)}(u)$, is a one-to-one vector function of u over the interval $0 \leq u < 2$ except for those $N - N_b$ discrete values of u listed in (2.23) where $\mathbf{b}_R^{(m)}(u) = \mathbf{0}_{N_b}$.

Proof: To prove the theorem, it is shown that the $N_b \times 2$ matrix $[\mathbf{b}_R^{(m)}(u_1) \vdots \mathbf{b}_R^{(m)}(u_2)]$ is of rank 2 when $u_1 \neq u_2$, $0 \leq u_i < 2$, i=1,2, and $u_i \notin \{0, \frac{2}{N}, \ldots, (m-1)\frac{2}{N}, (m+N_b)\frac{2}{N}, \ldots, (N-1)\frac{2}{N}\}$, i=1,2. Under the latter three conditions,

$$\text{rank}\{[\mathbf{b}_R^{(m)}(u_1) \vdots \mathbf{b}_R^{(m)}(u_2)]\} = \text{rank}\{\mathbf{W}_R^{(m)H}[\mathbf{a}_N(u_1) \vdots \mathbf{a}_N(u_2)]\}$$

$$\leq \min\left\{\text{rank}\{\mathbf{W}_R^{(m)H}\}, \text{rank}\{[\mathbf{a}_N(u_1) \vdots \mathbf{a}_N(u_2)]\}\right\} = \text{rank}\{[\mathbf{a}_N(u_1) \vdots \mathbf{a}_N(u_2)]\} = 2$$

where the fact that the columns of $\mathbf{W}_R^{(m)}$ are linearly independent (they are orthonormal) has been used, neither $\mathbf{a}_N(u_1)$ or $\mathbf{a}_N(u_2)$ is in the null space of $\mathbf{W}_R^{(m)}$, and $\mathbf{a}_N(u_1)$ and $\mathbf{a}_N(u_2)$ are linearly independent for $u_1 \neq u_2$ since $\mathbf{a}_N(u)$ is a scalar multipleof the Vanderinonde manifold vector $\mathbf{v}_N(u)$ in accordance with (2.50). The result above dictates that $\mathbf{b}_R^{(m)}(u_1)$ and $\mathbf{b}_R^{(m)}(u_2)$ are linearly independent which proves the Theorem. □

As a consequence of this theorem, it follows that if the total number of in-band and out-of-band sources is less than the number of beams formed to encompass a given sub-band, it is theoretically possible to estimate the direction of any out-of-band source not lying at a common null location as well as the direction of each in-band source. However, if the number of strong out-of-hand sources not sufficiently de-emphasized in the beamforming process combined with the number of in-band sources is greater than the dimension of the beamspace, beamspace Root-MUSIC is rendered totally nonfunctional. The use of tapering is thus explored as a means for reducing out-of-band sidelobes in order to diminish the pejorative effects of strong out-of-band sources lying at or near a common siclelobe peak location.

In order to achieve a reduced degree polynomial, the beams must exhibit common out-of-band nulls. One means of retaining the common out-of-band nulls property is to construct each beam comprising the set of reduced sidelobe beams as a linear

combination of DFT beams. Sidelobe reduction is achieved by exploiting the fact that the respective sidelobes of adjacent DFT beams are 180° out-of-phase. **A** nice feature of this approach is that the components of the beamspace snapshot vector are simply linear combinations of the in-hand DFT values; there is no need to taper at the element level and the initial step remains a.n N point DFT of each snapshot vector. Also, the real-valued nature of the beamspace manifold is retained allowing us to compute the beamspace noise eigenvectors in terms of a real-valued eigenvector decomposition (or singular value decomposition). These claims are substantiated in the following development.

2.6.1 The Cosine Window

Consider the N point DFT of the element space snapshot vector at discrete time n. N_b successive N point DFT values are selected and scaled in accordance with **(2.52).** Tapering at the element level in accorclance with the Cosine window may be alternatively implemented by adding adjacent DFT values pairwise across the m-th sub-band. This yields a $(\mathrm{A}^{\mathrm{r}}{}_{\mathrm{b}} - 1)$ x 1 beamspace snapshot vector denoted $\mathbf{y}_c^{(m)}(n)$. Mathematically, $\mathbf{y}_c^{(m)}(n)$ may be expressed in terms of $\mathbf{y}_R^{(m)}(n)$ as

$$\mathbf{y}_c^{(m)}(n) = \mathbf{T}_c^T \mathbf{y}_R^{(m)}(n) = \{\mathbf{W}_R^{(m)}\mathbf{T}_c\}^H \mathbf{x}(n) = \mathbf{W}_C^{(m)\,H}\mathbf{x}(n) \qquad [2.59]$$

where $\mathbf{W}_C^{(m)} = \mathbf{W}_R^{(m)}\mathbf{T}_c$ and $\mathbf{T}_c$ is the N_b x $(N_b - 1)$ transformation matrix

$$\mathbf{T}_c = \begin{bmatrix} .5 & 0 & & 0 \\ .5 & .5 & & 0 \\ 0 & .5 & \cdot & 0 \\ 0 & 0 & \cdot & 0 \\ \vdots & \vdots & \cdot & \vdots \\ 0 & 0 & & .5 \\ 0 & 0 & & .5 \end{bmatrix}. \qquad [2.60]$$

The fact that this procedure is equivalent to having formed $N_b - 1$ equi-spaced beams with a cosine taper at the element level is substantiated by invoking the definition of

$\mathbf{W}_R^{(m)}$ in (2.50) along with the definition of $\mathbf{a}_N(u)$ in (2.47) to express $\mathbf{W}_C^{(m)}$ as

$$\begin{aligned}\mathbf{W}_C^{(m)} &= \mathbf{W}_R^{(m)}\mathbf{T}_c \\ &= \mathbf{D}_c\left[\mathbf{a}_N\left(m\frac{2}{N}+\frac{1}{N}\right)\vdots\mathbf{a}_N\left([m+1]\frac{2}{N}+\frac{1}{N}\right)\vdots\ldots\vdots\mathbf{a}_N\left([m+N_b-2]\frac{2}{N}+\frac{1}{N}\right)\right]\end{aligned} \quad [2.61]$$

where $\mathbf{D}_c$ is the N x N diagonal matrix

$$\mathbf{D}_c = \mathrm{diag}\left\{\cos\left(\frac{N-1}{2}\frac{\pi}{2N}\right),\cos\left(\frac{N-3}{2}\frac{\pi}{2N}\right),\ldots,\cos\left(\frac{N-3}{2}\frac{\pi}{2N}\right),\cos\left(\frac{N-1}{2}\frac{\pi}{2N}\right)\right\}. \quad [2.62]$$

The elements of $\mathbf{D}_c$ effect a symmetric taper according to a cosine window. Note that the pointing angles of the $N_b - 1$ beams formed with "virtual" tapering according to a cosine window in this manner are located at the midpoints between the pointing angles of the N_b DFT beams.

Note that the columns of the N x (N_b-1) beamforming matrix $\mathbf{W}_C^{(m)} = \mathbf{W}_R^{(m)}\mathbf{T}_c$ are not orthogonal as $\mathbf{W}_C^{(m)H}\mathbf{W}_C^{(m)} = \mathbf{T}_c^T\mathbf{T}_c$. Orthogonalization of the beams may be achieved by post-multiplying $\mathbf{W}_C^{(m)}$ by the transformation $(\mathbf{T}_c^T\mathbf{T}_c)^{-\frac{1}{2}}$ creating

$$\mathbf{W}_{C_O}^{(m)} = \mathbf{W}_R^{(m)}\mathbf{T}_c(\mathbf{T}_c^T\mathbf{T}_c)^{-\frac{1}{2}} = \mathbf{C}_R^{(m)}\left\{\mathbf{Q}_R^{(m)}\mathbf{T}_c(\mathbf{T}_c^T\mathbf{T}_c)^{-\frac{1}{2}}\right\} \qquad (Nx(N_b-1)) \quad [2.63]$$

where (2.39) has been substituterl. Thus, $\mathbf{W}_{C_O}^{(m)}$ is a member of the class of orthogonal matrix beamformers described by (2.44)-(2.45). Note that the columns of $\mathbf{W}_{C_O}$ exhibit conjugate centro-symmetry as well since

$$\tilde{\mathbf{I}}_N\mathbf{W}_{C_O}^{(m)} = \tilde{\mathbf{I}}_N\mathbf{W}_R^{(m)}\mathbf{T}_c(\mathbf{T}_c^T\mathbf{T}_c)^{-\frac{1}{2}} = \mathbf{W}_R^{(m)*}\mathbf{T}_c(\mathbf{T}_c^T\mathbf{T}_c)^{-\frac{1}{2}} = \mathbf{W}_{C_O}^{(m)*} \quad [2.64]$$

where the fact that $\mathbf{T}_c$ is real-valued has been exploited. Hence, one may work solely with the real part of the beamspace sample covariance matrix.

Observing the far right-hand side of (2.63) and recalling the results and discussion in the previous sections, it follows that the beamspace Root-MUSIC procedure with orthogonalized, virtual cosine tapering is as follows. First,, construct the $(N_b - 1) \times (N_b - 1)$ beamspace sample covariance matrix

$$\hat{\mathbf{R}}_c^{(m)} = \frac{1}{M}\sum_{n=1}^{M}\mathbf{y}_C^{(m)}(n)\mathbf{y}_C^{(m)H}(n) = \mathbf{T}_c^T\mathcal{R}e\{\hat{\mathbf{R}}_y^{(m)}\}\mathbf{T}_c \quad [2.65]$$

where $\hat{\mathbf{R}}_y^{(m)}$ is the N_b x N_b beamspace sample covariance matrix formed from the N_b DFT beam outputs. Second, compute an eigenvector decomposition of the "whitened" beamspace sample covariance matrix $(\mathbf{T}_c^T\mathbf{T}_c)^{-\frac{1}{2}}\hat{\mathbf{R}}_c^{(m)}(\mathbf{T}_c^T\mathbf{T}_c)^{-\frac{1}{2}}$:

$$(\mathbf{T}_c^T\mathbf{T}_c)^{-\frac{1}{2}}\hat{\mathbf{R}}_c^{(m)}(\mathbf{T}_c^T\mathbf{T}_c)^{-\frac{1}{2}} = \sum_{i=1}^{N_b-1} \lambda_i \mathbf{e}_i\mathbf{e}_i^T \qquad [2.66]$$

Third, partition the eigenvectors into those which belong to the signal subspace and those which belong to the noise subspace. Let $\hat{K}$ denote the dimension of the estimated signal subspace. Fourth, construct a $(2N_b - 2)$-th order polynomial denoted $p_C^{(m)}(z)$ according to (2.35)-(2.37) with $\mathbf{P}_R^{(m)}$ replaced by

$$\mathbf{P}_c^{(m)} = \mathbf{Q}_R^{(m)}\mathbf{T}_c(\mathbf{T}_c^T\mathbf{T}_c)^{-\frac{1}{2}} \left\{ \sum_{i=\hat{K}+1}^{N_b-1} \mathbf{e}_i\mathbf{e}_i^T \right\} (\mathbf{T}_c^T\mathbf{T}_c)^{-\frac{1}{2}}\mathbf{T}_c^T\,\mathbf{Q}_R^{(m)H}. \qquad [2.67]$$

The final step is then to determine the signal roots of $p_C^{(m)}(z)$ in the usual fashion.

Alternatively, one may compute a generalized eigenvector decomposition as

$$\left\{\mathbf{T}_c^T\mathcal{R}e\{\hat{\mathbf{R}}_y^{(m)}\}\mathbf{T}_c\right\}\bar{\mathbf{e}}_i = \lambda_i\mathbf{T}_c^T\mathbf{T}_c\,\bar{\mathbf{e}}_i \qquad i = 1, 2, ..., N_b - 1 \qquad [2.68]$$

and replace $\mathbf{P}_c^{(m)}$ in the above procedure by

$$\bar{\mathbf{P}}_c^{(m)} = \mathbf{Q}_R^{(m)}\mathbf{T}_c \left\{ \sum_{i=\hat{K}+1}^{N_b-1} \bar{\mathbf{e}}_i\bar{\mathbf{e}}_i^T \right\} \mathbf{T}_c^T\,\mathbf{Q}_R^{(m)H}. \qquad [2.69]$$

Since it is easily shown that that $\bar{\mathbf{e}}_i = (\mathbf{T}_c^T\mathbf{T}_c)^{-\frac{1}{2}}\mathbf{e}_i$, i=1,2,...,$N_b$-1, it follows that the two procedures are equivalent.

2.6.2 The Hanning and Hamming Windows

Virtual tapering according to a. raised cosine winclow may be effected by letting the $N_b \times (N_b - 2)$ matrix

$$\mathbf{T}_H = \begin{bmatrix} \alpha & 0 & & 0 \\ 1 & \alpha & & 0 \\ \alpha & 1 & \cdot & 0 \\ 0 & \alpha & \cdot & 0 \\ \vdots & \vdots & & \vdots \\ 0 & 0 & & \alpha \\ 0 & 0 & & 1 \\ 0 & 0 & & \alpha \end{bmatrix} \qquad [2.70]$$

take on the role of $\mathbf{T}_c$ in the version of beamspace Root-MUSIC incorporating tapering developed above. The Hanning window is effected with $\alpha = .5$ while the Hamming window is effected with $\alpha = .5(.46/.54) = .426$. This claim is substantiated by again invoking the definition of $\mathbf{W}_R^{(m)}$ in *(2.50)* along with the definition of $\mathbf{a}_N(u)$ in *(2.47)* to express $\mathbf{W}_H^{(m)} = \mathbf{W}_R^{(m)}\mathbf{T}_H$ as

$$\begin{aligned} \mathbf{W}_H^{(m)} &= \mathbf{W}_R^{(m)}\mathbf{T}_H \qquad [2.71] \\ &= \mathbf{D}_H \left[\mathbf{a}_N\left([m+1]\frac{2}{N}\right) \vdots \mathbf{a}_N\left([m+2]\frac{2}{N}\right) \vdots \ldots \vdots \mathbf{a}_N\left([m+N_b-2]\frac{2}{N}\right)\right] \end{aligned}$$

where $\mathbf{D}_H$ is the $A' \times N$ diagonal matrix

$$\mathbf{D}_H = \text{diag}\left\{1-\alpha\cos\left(\frac{\pi}{2N}\right), 1-\alpha\cos\left(\frac{3\pi}{2N}\right), \ldots, 1-\alpha\cos\left(\frac{3\pi}{2N}\right), 1-\alpha\cos\left(\frac{\pi}{2N}\right)\right\}. \qquad [2.72]$$

It is apparent that $\alpha = .5$ yields virtual Hanning tapering while $\alpha = .5(.46/.54) = .426$ yields virtual Hamming tapering a.s stated above.

Similar to (2.63), the orthogonalized version of the Hamming or Hanning beamforming matrix may be expressed as

$$\mathbf{W}_{H_O}^{(m)} = \mathbf{W}_R^{(m)}\mathbf{T}_H(\mathbf{T}_H^T\mathbf{T}_H)^{-\frac{1}{2}} = \mathbf{C}_R^{(m)}\left\{\mathbf{Q}_R^{(m)}\mathbf{T}_H(\mathbf{T}_H^T\mathbf{T}_H)^{-\frac{1}{2}}\right\} \quad N \times (N_b - 2). \qquad [2.73]$$

It follows that $\mathbf{W}_{H_O}^{(m)}$ is a member of the class of orthogonal matrix beamformers described by (2.44)-(2.45). It is also easily shown that the columns of $\mathbf{W}_{H_O}$ exhibit conjugate centro-symmetry as well.

As an illustrative example, Figure 2.2(a) displays the $N_b - 2 = 6$ beams formed via virtual Hamming tapering for the case of an $N = 32$ element ULA. Each beam was synthesized by weighting and summing three adjacent beams out of the $N_b = 8$ DFT beams plotted in Figure 2.1(a) in accordance with (2.70) and (2.73) with $\alpha = .426$. In each beam pattern plotted in Figure 2.2(a), observe the equi-ripple sidelobe behavior characteristic of the spatial frequency response of the Hamming window. Note that by construction, the $N_b - 2 = 6$ beams depicted in Figure 2.2(a) have the same $N - N_b = 32 - 8 = 24$ out-of-band common nulls possessed by the $N_b = 8$ beams plotted in Figure 2.1(a). This set of beams represents an example where the number of common nulls is two less the maximum amount equal to the number of elements minus the number of beams ($23 < 32 - 8 = 25$). Figure 2.2(b) displays the $N_b - 2 = 6$ beams formed by applying the orthogonalizing transformation $(\mathbf{T}_H^T \mathbf{T}_H)^{-\frac{1}{2}}$ to the set of $N_b - 2 = 6$ beams plotted in Figure 2.2(a). Comparing Figures 2.2(a) and 2.2(b), it is observed that orthogonalization of the beams gives rise to an increase in out-of-band sidelobe level between 5 and 10 dB and a substantial increase in in-band sidelobe level. Note that high in-band sidelobes are not undesirable. Also, the number and respective locations of the common out-of-band nulls are not affected by orthogonalization.

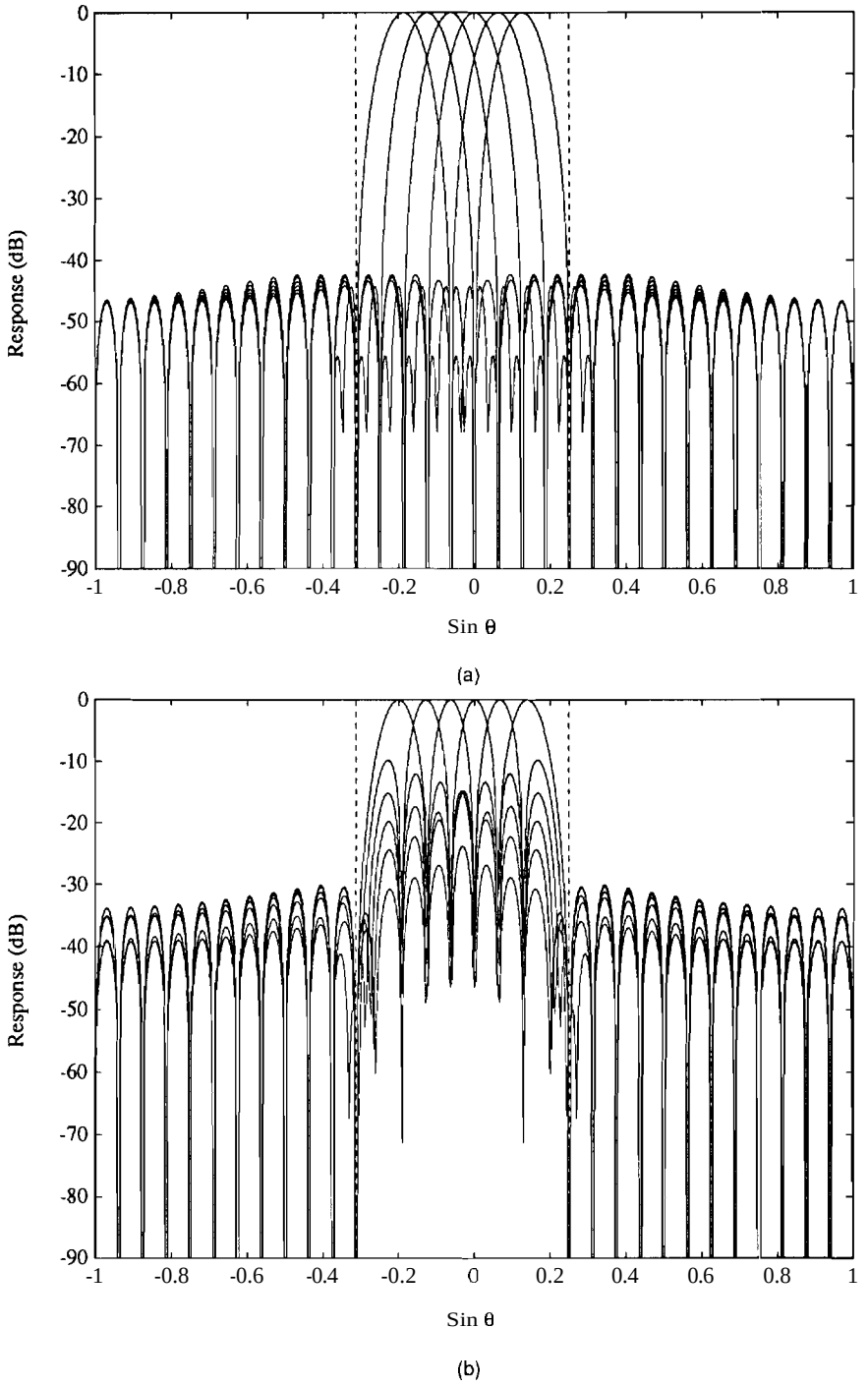

Figure 2.2 (a) Six equi-spaced beams formed via, virtual Hamming tapering. (b) Orthogonalized set of beams derived from those in (la).

2.7 Construction of Interference Cancellation Matrix Beamformer

The premise of this section is that with the information gained through initial probing of multiple, overlapping sub-bands via. DFT based beamspace Root-MUSIC (with or without virtual tapering), we are interested in focusing on a particular sub-band and have estimates of the directions of out-of-band sources. For the purposes of this section, these out-of-band sources are referred to as interferers. The goal then is to design a matrix beamformer for the sub-band of interest exhibiting the common out-of-band nulls property, so that one may work with a reduced degree polynomial, but with a subset of the common nulls aligned with the directions of out-of-band interferers. The issue then becomes where do we position the remaining common out-of-band nulls. Since simulations show that the N x N_b DFT matrix beamformer yields the best performance throughout the sub-band, in comparison to that of weighted beamformers, the interference cancellation matrix beamformer is designed so as to emulate the N x N_b DFT matrix beamformer as much as possible. In fact, we will find that we are able to do so well enough that despite the induced nulls, virtual tapering may be effected by adding weighted beam outputs exactly as described in Section 2.5. This is important for scenarios in which low out-of-band sidelobes as well as hard nulls at specified out-of-band locations are desired. Such scenarios arise in radar, for example, when the radar has to deal with diffuse sources such as clutter and nonspecular multipath as well as point jammers.

As in previous developments, let N_b denote the number of beams formed to encompass the sub-band of interest. Further, let the sub-band of interest be referred to as the m-th sub-band and denote the A' x N_b out-of-band interference cancellation matrix beamformer as $\mathbf{W}_I^{(m)}$. Note that relative to the initial probing phase, it is expected that N_b should be smaller as some rough information on the locations of in-band sources is available [6, 7]. In accordance with the discussion above, select an $N \times N_b$ DFT matrix beamformer $\mathbf{W}_R^{(m)}$ lor which the corresponding beam set

encompasses the sub-band of interest. $\mathbf{W}_I^{(m)}$ is then designed to emulate $\mathbf{W}_R^{(m)}$ as much as possible.

Let u_{I_i}, i=1,...,J, denote the directions in which J out-of-band nulls are to be formed. The null constraints to be satisfied may be mathematically expressed as

$$\mathbf{W}_I^{(m)H}\,\mathbf{a}_N(u_{I_i}) = \mathbf{0}_J \quad i = 1, ..., J. \tag{2.74}$$

Further, let $\mathbf{c}_I^{(m)}(z)$ denote the $(N-N_b)$-th order common roots polynomial. It follows that J of the $N-N_b$ roots of $\mathbf{c}_I^{(m)}(z)$ are $z_i = \exp[j\pi u_{I_i}]$, i=1,...,J. Let $\mathbf{C}_I^{(m)}$ denote the $N \times N_b$ banded-Toeplitz matrix constructed from the coefficients of $\mathbf{c}_I^{(m)*}(z)$ according to (2.42). Imposition of the common out-of-band nulls property relegates $\mathbf{W}_I^{(m)}$ to be a member of the class of matrix beamformers described by (2.44)-(2.45) so that it may be factored as

$$\mathbf{W}_I^{(m)} = \left[\mathbf{w}_1 \vdots \mathbf{w}_2 \vdots \ldots \vdots \mathbf{w}_{N_b}\right] = \mathbf{C}_I^{(m)}(\mathbf{C}_I^{(m)H}\mathbf{C}_I^{(m)})^{-\frac{1}{2}}\mathbf{U} \tag{2.75}$$

where U is a $N_b \times N_b$ unitary matrix. U is square since the number of common nulls is constrained to be the maximum amount equal to the number of elements minus the number of beams. Basically, our problem at this point is to determine the remaining $N - N_b - J$ roots of $\mathbf{c}_I^{(m)}(z)$ and $\mathbf{U}$ so as to minimize $\|\mathbf{W}_R^{(m)} - \mathbf{W}_I^{(m)}\|_F^2$, where F denotes the Frobenius norm, under the structural const,ra.intin (2.75).

The approach is to first determine $\mathbf{c}_I^{(m)}(z)$. To this end, construct the k-th column of $\mathbf{W}_I^{(m)}$, denoted $\mathbf{w}_k$ where $k \in \{1, ..., N_b\}$, so that it is "close" in a least squares sense to the k-th column of $\mathbf{W}_R^{(m)}$, $\mathbf{a}_N([m + k]_{\frac{2}{N}})$, under the constraint that the corresponding beam exhibit nulls at the J prescribed interference locations and the same $N_b - 1$ in-band nulls exhibited by the beam corresponding to $\mathbf{a}_N([m + k]_{\frac{2}{N}})$. $\mathbf{c}_I^{(m)}(z)$ is then computed as tlie ratio of $w_k(z)$ to $q_{m+k}(z)$, where $q_{m+k}(z)$ is defined by (2.31) (with the coefficients normalized to exhibit conjugate centro-symmetry).

In order to solve for $\mathbf{w}_k$, let $\{\mathbf{f}_1, \mathbf{f}_2, \ldots, \mathbf{f}_{N-N_b-J}\}$ denote an orthonormal basis defined as

$$\text{span}\{\mathbf{f}_1,\ldots,\mathbf{f}_{N-N_b-J}\} = \text{span}\left\{\mathbf{a}_N\left(\frac{2m}{N}\right),\ldots, \right. \quad [2.76]$$

$$\left.\mathbf{a}_N\left(\frac{2[m+k-1]}{N}\right), \mathbf{a}_N\left(\frac{2[m+k+1]}{N}\right), \ldots \mathbf{a}_N\left(\frac{2[m+N_b-1]}{N}\right), \mathbf{a}_N(u_{I_1}),\ldots,\mathbf{a}_N(u_{I_J})\right\}^{\perp}$$

where $\perp$ denotes orthogonal complement. It follows from the null constraints on the beam formed with $\mathbf{w}_k$ that $\mathbf{w}_k$ must lie in the subspace described by (2.76). Thus, denoting $\mathbf{F} = [\mathbf{f}_1 \vdots \mathbf{f}_2 \vdots \ldots \vdots \mathbf{f}_{N-N_b-J}]$, an N x $(N - N_b - J)$ matrix, it follows that $\mathbf{w}_k = \mathbf{Fd}$, where d is an $(N - N_b - J)$ x 1 vector. d is determined as the solution to

$$\min_{\mathbf{d}} \left\| \mathbf{a}_N\left([m+k]\frac{2}{N}\right) - \mathbf{w}_k \right\|_2^2 = \left\| \mathbf{a}_N\left([m+k]\frac{2}{N}\right) - \mathbf{Fd} \right\|_2^2. \quad [2.77]$$

The solution is simply the least square error (LSE) solution to the linear system of equations $\mathbf{Fd} = \mathbf{a}_N([m+k]\frac{2}{N})$, $\mathbf{d} = \mathbf{F}^H\mathbf{a}_N([m+k]\frac{2}{N})$. Since the columns of $\mathbf{F}$ are orthonormal, $\mathbf{w}_k = \mathbf{FF}^H\mathbf{a}_N([m+k]\frac{2}{N})$.

Recall that the solution for $\mathbf{w}_k$ computed above guarantees that the corresponding beam exhibits the same $N_b - 1$ in-band nulls exhibited by the beam corresponding to $\mathbf{a}_N([m+k]\frac{2}{N})$. Thus, the corresponding polynomial $w_k(z)$ may be factored as $q_{m+k}(z)\,c(z)$ where $q_{m+k}(z)$ is defined by (2.31) and c(z) is a polynomial of order $N - N_b$. We will take the polynomial c(z) to be the common roots polynomial $c_I^{(m)}(z)$. That is,

$$c_I^{(m)}(z) = \frac{w_k(z)}{q_{m+k}(z)}. \quad [2.78]$$

Accordingly, the length $N - N_b + 1$ sequence $\{\mathbf{c}_I^{(m)}\}$ may be computed by simply deconvolving the length N_b sequence $\{\mathbf{q}_{m+k}\}$ out of the length N sequence $\{\mathbf{w}_k\}$.

Given the sequence $\{\mathbf{c}_I^{(m)}\}$ determined above, one may construct the banded-Toeplitz matrix $\mathbf{C}_I^{(m)}$ according to (2.40) or (2.42). At this point, we have $\mathbf{W}_I^{(m)} = \mathbf{C}_I^{(m)}\,\mathbf{Q}_I^{(m)}$ and desire to choose $\mathbf{Q}_I^{(m)}$ so as to minimize $\|\mathbf{W}_R^{(m)} - \mathbf{C}_I^{(m)}\,\mathbf{Q}_I^{(m)}\|_F^2$. One is tempted to choose $\mathbf{Q}_I^{(m)} = \mathbf{Q}_R^{(m)}$, where $\mathbf{Q}_R^{(m)}$ is defined in (2.33), as this restricts the in-band nulls of the beam generated by each column of $\mathbf{W}_I^{(m)} = \mathbf{C}_I^{(m)}\,\mathbf{Q}_R^{(m)}$ to be the same as that of the corresponding column of $\mathbf{W}_R^{(m)}$. Note that this claim is

substantiated by the interpretation of the product $\mathbf{C}_I^{(m)}\ \mathbf{Q}_R^{(m)}$ as a convolution as discussed in Section 2.4. However, the columns of $\mathbf{W}_I^{(m)} = \mathbf{C}_I^{(m)}\ \mathbf{Q}_R^{(m)}$ are not, in general, mutually orthogonal. Orthogonality may be achieved by post-multiplying by $\left(\mathbf{Q}_R^{(m)H}\mathbf{C}_I^{(m)H}\mathbf{C}_I^{(m)}\mathbf{Q}_R^{(m)}\right)^{-\frac{1}{2}}$ leading to the general form

$$\mathbf{W}_I^{(m)} = \mathbf{W}_O\mathbf{\Gamma} \qquad [2.79]$$

where $\mathbf{\Gamma}$ is a N_b x N_b unitary matrix and

$$\mathbf{W}_O = \mathbf{C}_I^{(m)}\mathbf{Q}_R^{(m)}\left(\mathbf{Q}_R^{(m)H}\mathbf{C}_I^{(m)H}\mathbf{C}_I^{(m)}\mathbf{Q}_R^{(m)}\right)^{-\frac{1}{2}}. \qquad [2.80]$$

It is easily verified that the form of $\mathbf{W}_I^{(m)}$ in (2.79)-(2.80) satisfies $\mathbf{W}_I^{(m)H}\mathbf{W}_I^{(m)} = \mathbf{I}_N$, as desired. $\mathbf{\Gamma}$ is then chosen as the solution to the following constrained optimization problem

$$\min_{\mathbf{\Gamma}} \left\| \mathbf{W}_R^{(m)} - \mathbf{W}_I^{(m)} \right\|_F^2 = \left\| \mathbf{W}_R^{(m)} - \mathbf{W}_O\mathbf{\Gamma} \right\|_F^2 \qquad [2.81]$$

$$\text{subject to: } \mathbf{\Gamma}^H\mathbf{\Gamma} = \mathbf{\Gamma}\mathbf{\Gamma}^H = \mathbf{I}_{N_b}.$$

Equation (2.81) is recognized as an orthogonal Procrustes rotation problem [5]. The solution may be coinputed as follows. First, compute the SVD of the N_b x N_b matrix $\mathbf{W}_R^{(m)H}\mathbf{W}_O$, where $\mathbf{W}_O$ is given by (2.79). If $\mathbf{W}_R^{(m)H}\mathbf{W}_O = \mathbf{U}\mathbf{\Sigma}\mathbf{V}^H$ is the SVD, the solution to (2.81) is $\mathbf{\Gamma} = \mathbf{U}\mathbf{V}^H$.

Note that the above development assumed the conjugate centro-symmetric form of the N x N_b DFT matrix beamformer in (2.51). In the factorization $\mathbf{W}_R^{(m)} = \mathbf{C}_R^{(m)}\ \mathbf{Q}_R^{(m)}$, this implies that $\mathbf{c}_R^{(m)}$ and each column of $\mathbf{Q}_R^{(m)}$ are scaled to be conjugate centro-symmetric. This is possible since the corresponding polynomial in each case has all of its roots on the unit circle. It follows then that $\check{\mathbf{I}}_{N_b}\mathbf{Q}_R^{(m)} = \mathbf{Q}_R^{(m)*}$ and $\check{\mathbf{I}}_{N-N_b+1}\mathbf{c}_R^{(m)} = \mathbf{c}_R^{(m)*}$ which, in turn, yields the property $\check{\mathbf{I}}_N\mathbf{C}_R^{(m)}\check{\mathbf{I}}_{N_b} = \mathbf{C}_R^{(m)*}$. Based on these properties of $\mathbf{Q}_R^{(m)}$, $\mathbf{c}_R^{(m)}$, and $\mathbf{C}_R^{(m)}$, it may be proved that the interference cancellation matrix beamformer constructed according to the procedure developed above satisfies $\check{\mathbf{I}}_N\mathbf{W}_I^{(m)} = \mathbf{W}_I^{(m)*}$. Therefore, similar to the case with the $N \times N_b$ *DFT* matrix beamformer, one may work with the real part of the beamspace SCM $\hat{\mathbf{R}}_I^{(m)} = \mathbf{W}_I^{(m)H}\hat{\mathbf{R}}_x\mathbf{W}_I^{(m)}$

Thus, relative to the beamspace Root-MUSIC procedure based on the use of the $N \times N_b$ DFT matrix beamformer, the only difference when employing $\mathbf{W}_I^{(m)}$ determined according to the above procedure, is that $\mathbf{W}_I^{(m)}$ takes on the role of $\mathbf{W}_R^{(m)}$ and $\mathbf{Q}_I^{(m)} = \mathbf{Q}_R^{(m)}(\mathbf{Q}_R^{(m)H}\mathbf{C}_I^{(m)H}\mathbf{C}_I^{(m)}\mathbf{Q}_R^{(m)})^{-\frac{1}{2}}\mathbf{\Gamma}$ takes on the role of $\mathbf{Q}_R^{(m)}$. Otherwise, the procedure is exactly the same with the major computations being a N_b x N_b real-valued EVD and the rooting of a polynomial of order $2N_b - 2$.

As an illustrative example, an interference cancellation matrix beamformer was constructed according to the above procedure to probe the same sub-band encompassed by the $N_b = 8$ DFT beams depicted in Figure 2.1(a) under the constraint that each beam exhibit a null at each of the two common out-of-band peak sidelobe locations indicated in Figure 2.1(a). Figure 2.3(a) displays the $N_b = 8$ beams generated by the interference cancellation matrix beamformer thus created. It is observed that the beams exhibit $N - N_b = 24$ common out-of-band nulls as desired. Away from the region of the two prescribed out-of-band nulls, the beam patterns are observed to be very similar to the DFT beam patterns displayed in Figure 2.1(a). Although it cannot be discerned from the magnitutle plot, the beams exhibit the same sidelobe phase relationships exhibited by the DFT beams in that the respective sidelobes of adjacent beams are 180° out-of-phase. This property may be exploited to achieve reduced out-of-band sidelobes via virtual tapering in exactly the same way it is achieved with DFT beams. This claim is substantiated by the beam set plotted in Figure 2.3(b) corresponding to virtual cosine tapering. Here each beam is the sum beam created by adding an adjacent pair of the $N_b = 8$ beams plotted in Figure 2.3(b). Figure 2.3 demonstrates the efficacy of the interference cancellation matrix beamformer design procedure developed in this section.

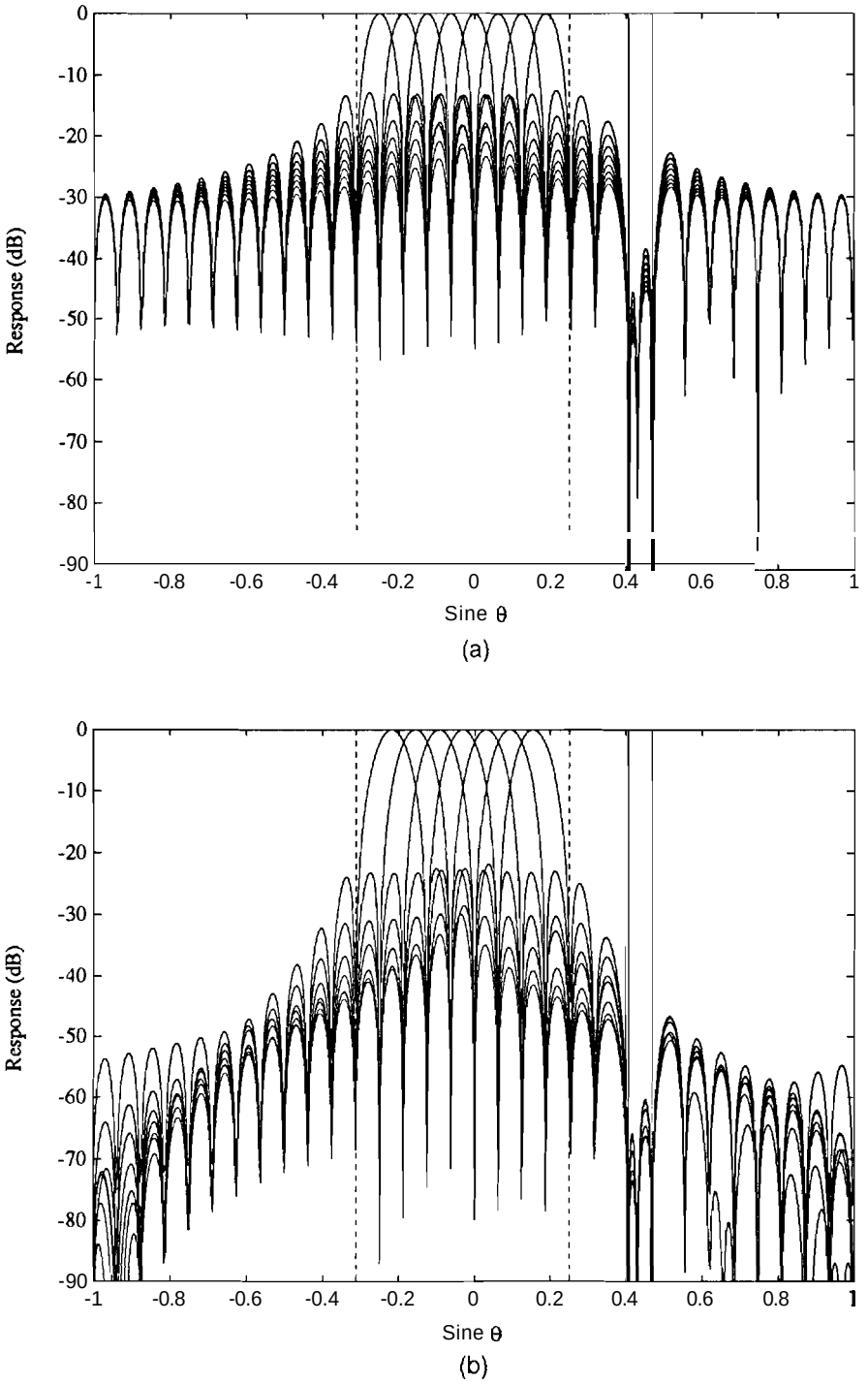

Figure 2.3 (a) "Adaptetl" beams derivctl from those in Figure 2.1(a) via interference cancellation matrix beamforming method. Each beam exhibits a null in each of the two interference locations. (b) Seven beams derived from those in (a); each beam is the sum of an adjacent pair of beams.

2.8 Computer Experiments/Simulations

Simulations involving an N = 32 element ULA with half-wavelength spacing were conducted to ascertain the efficacy of the Beamspace Root-MUSIC algorithm developed in this chapter. The sources were mutually uncorrelated in all test cases. The stated SNR for a particular source is that per element; the noise was spatially white. All sample biases and sample standard cleviations cited were computed from 250 independent runs and are in units of degrees. Finally, separation by half-Rayleigh implies a separation of $1/N$ in the $u = \sin\theta$ domain corresponding to half of the 3 dB beamwidth.

Figure 2.4 compares the performance of element space Root-MUSIC with that of beamspace Root-MUSIC using the beam set in Figure 2.1(a) for the case of two in-band sources separated by half-Rayleigh and a strong source located a.t a common peak sidelobe just outside the band. In the $u = \sin\theta$ domain, the beam pointing angles are $(-8 + 2i)/N$, i=0,1,...,7. The in-band sources were equi-powered with $\mathrm{SNR}_1 = \mathrm{SNR}_2 = 3$ dB and were located approximately mid-band at $u_1 = 0$ and $u_2 = 1/N$. The out-of-band source was located a.t $u_3 = 9/N$ with $\mathrm{SNR}_3 = 20$ dB. Recall that u $= 8/N$ is a common null location marking the edge of the: band; the next common null location is u $= 10/N$. Finally, for each trial run the number of snapshots was M = 32 and the number of signals assumed was three.

The respective sample standard deviations obtained with beamspace Root-MUSIC is observed to be nearly identical to that obtained with element space Root-MUSIC for each of the two in-band sources. However, the sample bias is significantly lower for beamspace Root-MUSIC. Comparing the root plot in Figure 2.4(a) with that in Figure 2.4(b), note that the in-band signal roots obtained with beamspace Root-MUSIC are closer to the unit circle than those obtained with element space Root-MUSIC. Note that for element space Root-MUSIC, the major computations are the eigendecomposition of a complex-valued 32 x 32 matrix and the rooting of a polynomial of order $2N - 2 = 62$. On the other hand, the major computations for beam space

Root-MUSIC are the eigendecomposition of a real-valued S x S matrix and the rooting of a polynomial of order $2N_b - 2 = 14$.

In accordance with the discussion in Section 2.6, beamspace Root-MUSIC is able to accurately localize the strong out-of-band source. It is important to note, however, a reduction in the number of assumed signals from three to two has a severe pejorative effect on the performance of beamspace Root-MUSIC with respect to the in-band sources. This is demonstrated in the simulation results presented in Figure 2.8(a) for the case of a weaker out-of-band source located at the fourth common peak sidelobe outside the band! The results in Figure 2.S will be discussed shortly. On the other hand, an increase in the number of assumed signals from three to four has relatively little effect on performance. Thus, a.s with spectral MUSIC in either element space or beamspace, in drawing the line of demarcation between the signal and noise eigenvalues, it's critical to err on the side of overestimation of the number of sources.

Of course, element space Root-MUSIC significantly outperforms beamspace Root-MUSIC with regard to localizing the out-of-band source a.t $u_3 = 9/N$. In fact, the sample bias and sample standard deviation of element space Root-MUSIC for this source is so small that one cannot discern the scatter of the associated roots in the root plot of Figure 2.5(b). (The cluster of roots closest to the origin in Figure 2.5(b) are not signal roots.) It should be pointed out, though, if desired the source at $u_3 = 9/N$ may be more accurately localizecl with beamspace Root-MUSIC by processing an adjacent sub-band.

In their performance analysis of Root-MUSIC in element space, Rao and Hari [10] show that the error in each of the signal zeros of the Root-MUSIC polynomial has a largely radial component. A purely radial error in a given signal zero has no effect on the corresponding source angle estimate but causes the corresponding signal peak in the MUSIC spatial spectrum to be less pronounced. Thus, although Rao and Hari show that the asymptotic mean square error of the source angle estimates obtained with Root-MUSIC is the same as that. obtained with Spectral MUSIC, they point out that "implicit in the derivation of the mean square error for Spectral MUSIC

is the assumption that corresponding to each source there is a. peak in the spatial spectrum." As Rao and Hari point out, this "is a. stronger assumption than distinct z-plane roots." They demonstrate the improved performance of Root-MUSIC over Spectral MUSIC by presenting simulations in which the MUSIC spectrum exhibits a single peak in the vicinity of two closely-spaced sources while the corresponding Root-MUSIC polynomial exhibits two clearly distinct signal zeros. Thus, the main advantage of Root-MUSIC over Spectral MUSIC in element space is with respect to probability of resolution. Nest, simulations show that the same is true in beamspace.

Figure 2.5 compares the probability of resolution of beamspace Root-MUSIC with that of Beamspace Spectral MUSIC over a range of SNR values for two equi-powered, uncorrelated sources separated by half-Rayleigh. The following parameters were common to each trial run. The two sources were located a.t $u_1 = 1/(2N)$ and $u_2 = -1/(2N)$; recall that $N = 32$. $N_b = 4$ consecutive beams out of the eight beams displayed in Figure 2.1(a), with tlie first beam having a. pointing angle of u $= -4/N$, were employed yielding $2N_b - 2 = 6$ roots per run, 3 reciprocal-magnitude pairs. For each trial run, beamspace Root-MUSIC and beamspace Spectral MUSIC were both supplied with the same $M = 4$ snapshots. For each of 17 different SNR values, the empirical probability of resolution for either algorithm was computed from 1000 independent trials. For beamspace Spectral MUSIC, tlie two sources were said to be resolved if the beamspace MUSIC spectrum exhibited a local maximum in each of the two half-beamwidth sectors, $-1/N < u < 0$ and $0 < u < 1/N$. Note that a source is located at the center of each of these two half-beamwidth sector:;. In accordance with the relationship $z = \exp[j\pi u]$, the corresponding resolution criterion for Beamspace Root-MUSIC was as follows: the two sources were declared resolved if the beamspace Root-MUSIC polynomial yielded a. root in each of two swaths of the complex z-plane described by $\exp[-j\pi/N] \leq \arg\{z\} \leq \exp[-j\pi/20N]$ n $.8 \leq |z| \leq 1$ and $\exp[j\pi/20N] \leq \arg\{z\} \leq \exp[j\pi/N]$ $\in$ $.8 \leq |z| \leq 1$, respectively. Thus a minimum angular separation of one-twentieth of a beamwidth between the two signal roots, and that each have a. magnitude between 0.8 and unity, for the two sources was

imposed to declare a resolved signal. The resulting probability of resolution curves are displayed in Figure 2.5.

Comparing the probability of resolution curves in Figure 2.5, it is observed that the performance of beamspace Root-MUSIC is about 4 dB better on average than beamspace Spectral MUSIC. That is, on average, beamspace Spectral MUSIC requires about 4 dB more SNR per element than beamspace Root-MUSIC to achieve roughly the same probability of resolution. In accordance with the resolution criteria described above, the performance differential is clue to runs in which the beamspace MUSIC spectrum exhibits a single peak while the corresponding beamspace Root-MUSIC polynomial exhibits two clearly distinct signal zeros. Figure 2.6 shows the overlaid results of five independent runs where this was the case when the SNR of each source was -3 dB. (Note that with regard to beamspace Spectral RIUSIC, four different line types were usecl so that the solid line was used twice.) The respective positions of each of the actual signal roots are indicated by a radial line in the beamspace Root-MUSIC scatter plot. In each of the five runs, tlie beamspace MUSIC spectrum exhibited a peak in the vicinitv of one of the sources, but not in the direction of the other. The source it worked well for varied among the five runs. A11 examination of the two corresponding signal reciprocal-magnitude root pairs for a given run reveals one pair to be close to the unit circle while tlie other pair was significantly removed from the unit circle. (This is hard to discern with the results of five runs overlaid.) The simulation results presented in Figures 2.5 and 2.6 illustrate the improved performance of beamspace Root-MUSIC over beamspace Spectral MUSIC.

Figure 2.7 tracks the performance of beamspace Root-MUSIC a.s the position of two equi-powered sources with half-Rayleigh separation is varied from the center to the upper edge of the band. This is clone for the beam set displayed in Figure 2.1(a) and for each of three beam sets derived from that in Figure 2.1(a) by virtual tapering according to either the cosine, Hanning, or Hamming windows. Recall that $u = -10/N$ and $u = 8/N$ are common null locations marking the upper and lower edges of the band, respectively. The center of the band is thus $u = -1/N$. For each

trial run, the SNR for each source was 6 dl3 and the algorithm was supplied with M = 16 snapshots. The sample bias and sample standard deviation curves obtained for the "left" source (i.e., the source having the smaller value of u) are displayed in Figures 2.7(a) and 2.7(b), respectively. The abscissa in either figure is the u = $\sin\theta$ bearing of the "left" source. Finally, note that regardless of the beam set employed, the initial step is the computation of $N_b = 8$ successive 32 point DFT values. Virtual tapering according to the cosine, Hanning, or Hamming windows was accomplished by adding successive, weighted DFT values as discussed in Section 2.6.

Figure 2.7 evokes a number of observations. First, the beam set displayed in Figure 2.1(a) corresponding to no tapering is observed to yield the best performance over the entire half-band. The performance obtained with each of the four beam sets is observed to degrade towards the edge of the sub-band; the performance of the Hamming window beam set is observed to fall off first. As we approach the edge of the sub-band, we have *a* dynamic range problem in that the "left" source is "passed" with significantly more gain than the "right" source; when the "left" source is at u = $7/N$, the "right" source is at the common null position $u = 8/N$. These results emphasize the importance of overlapping the sub-bands. Note that with 50% overlap among sub-bands, a source a.t the edge of one band will lie at the center of an adjacent sub-band [12]. Thus, 50% overlap among sub-bands is recommended.

Although no tapering yielded the best performance in the previous set of simulation results, it is important to keep in mind that no tapering also provides the least amount of out-of-band source filtering. This phenomenon is illustrated in Figure 2.8. Figure 2.8 displays the performance of beamspace Root-MUSIC assuming two sources in the case of two in-band sources separated bv half-Rayleigh and a strong out-of-band source located at a common peak sidelobe. The in-band sources were equi-powered with $\mathrm{SNR}_1 = \mathrm{SNR}_2 = 6$ dB and were located at $u_1 = 0$ and $u_2 = 1/N$. The out-of-band source was located at $u_3 = -17/N$ with $\mathrm{SNR}_3 = 18$ dB. Note that u = $-17/N$ is the location of the fourth common peak sidelobe away from the lower edge of the band marked by the common null location at $u = -10/N$. The position

of the actual signal root associated with tlie out-of-band source at $u_3 = -17/N$ is indicated by a radial line in Figures 2.8(a) and 2.8(b) as are the actual signal roots associated with the two in-band sources. For each trial run the number of snapshots was **M = 32.** Finally, the performance achieved with no tapering and that achieved with virtual Hamming tapering are displayed in Figures 2.8(a) and 2.8(b), respectively.

Despite the fact that the out-of-band source was located a number of beamwidths away from the edge of the band, discounting its contribution to the:eigenstructure of the beamspace sample correlation matrix is observed to be a fatal mistake in the case of no tapering. In 38 out of tlie 250 runs, the in-band signal roots were aligned at the same phase angle corresponding to an unresolved situation. The signal roots obtained in the other 212 runs were heavily biased. In contrast, tlie use of Hamming tapering provides adequate filtering of the out-of-band source as evidenced by the root scatter plot displayed in Figure 2.8(b). Of course, performance in the case of no tapering may be improved dramatically by increasing the number of assumed signals from two to three. However, the point is that is it is imperative to do so with no tapering while good performance is achieved with virtual Hamming tapering without resorting to such. This has implications with regard to avoiding a situation in which the number of in-band sources and inadequately filtered out-of-band sources is greater than the dimension of tlie beamspace.

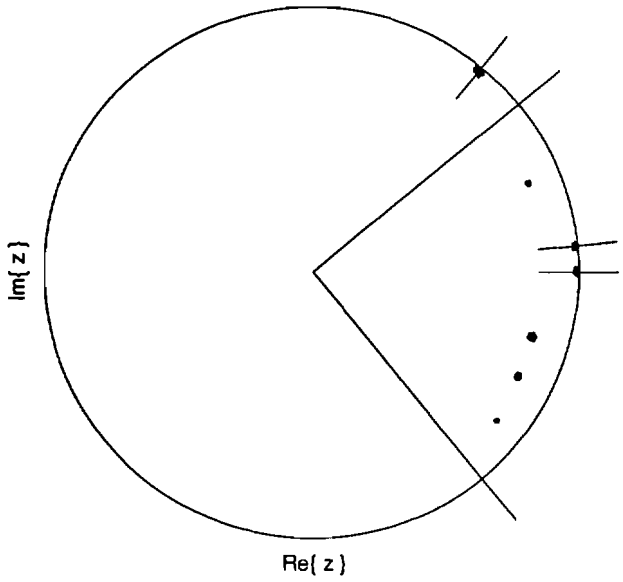

Source angle	Bias (deg.)	Std. Dev. (deg.)
$u_1 = 0$	-0.00827	0.0827
$u_2 = 1/N$	0.00100	0.0903
$u_3 = 9/N$	-0.01145	0.1382

(a)

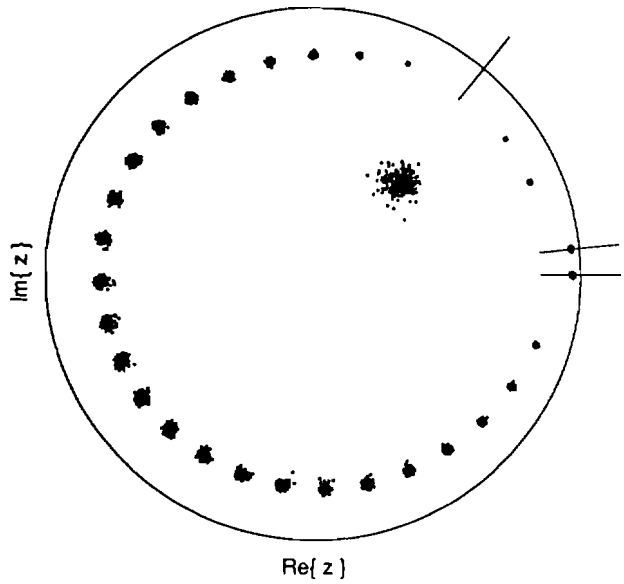

Source angle	Bias (deg.)	Std. Dev. (deg.)
$u_1 = 0$	-0.01959	0.0794
$u_2 = 1/N$	0.01300	0.0857
$u_3 = 9/N$	-0.00002	0.0049

(b)

Figure 2.4 Beamspace Root-MUSIC vs. Element-space Root-MUSIC for beam set of Figure 1. (a) Beamspace Root-MUSIC. (b) Element-space Root-MUSIC

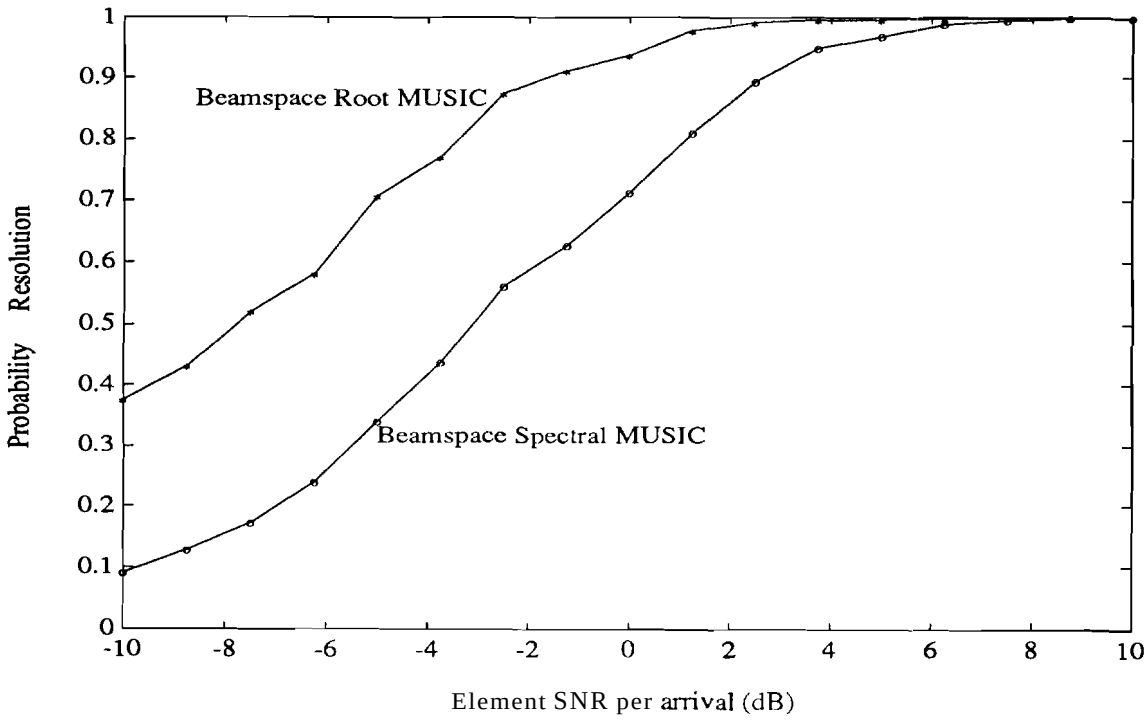

Figure 2.5 Empirical probability of resolution versus SNR curves: Beamspace Root-MUSIC versus beamspace spectral MUSIC with two equi-powered and uncorrelated in-band sources located at $-1/(2N)$ and $1/(2N)$. $N_b = 4$ out of the eight beams displayed in Figure 2.1(a).

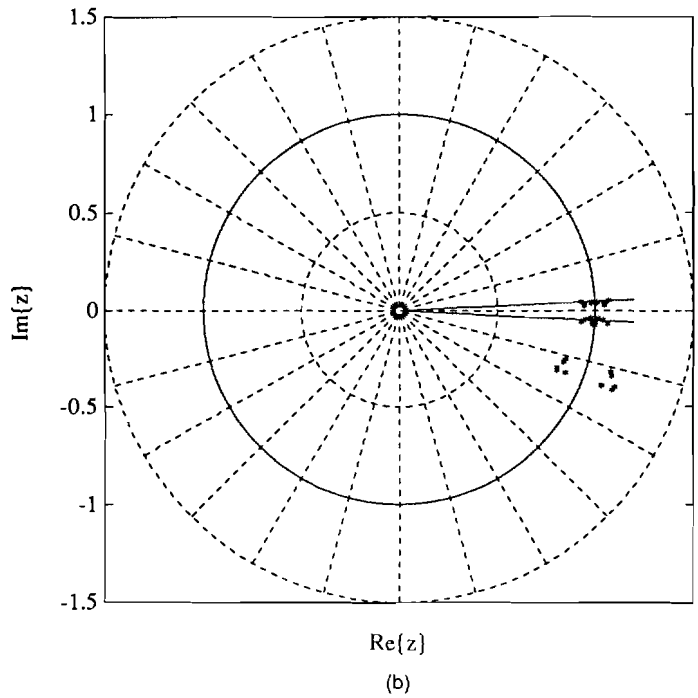

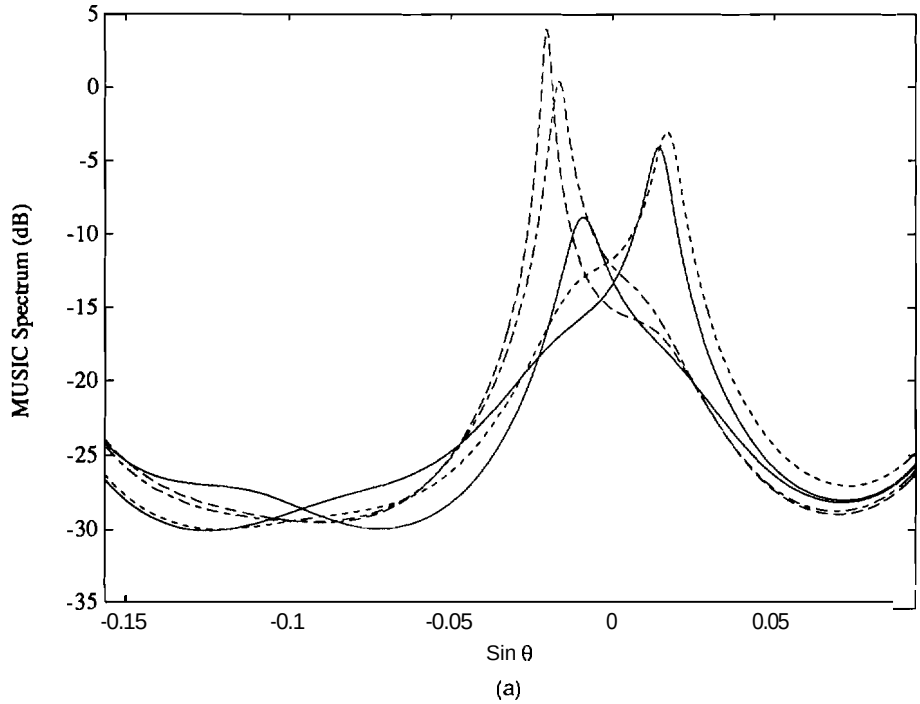

Figure 2.6 Beamspace Root-MUSIC versus beamspace spectral MUSIC. Same scenario as that in Figure 2.5 except SNR = 0dB. (a) Root scatter plot obtained from five independent runs. (b) Corresponding beamspace spectra.

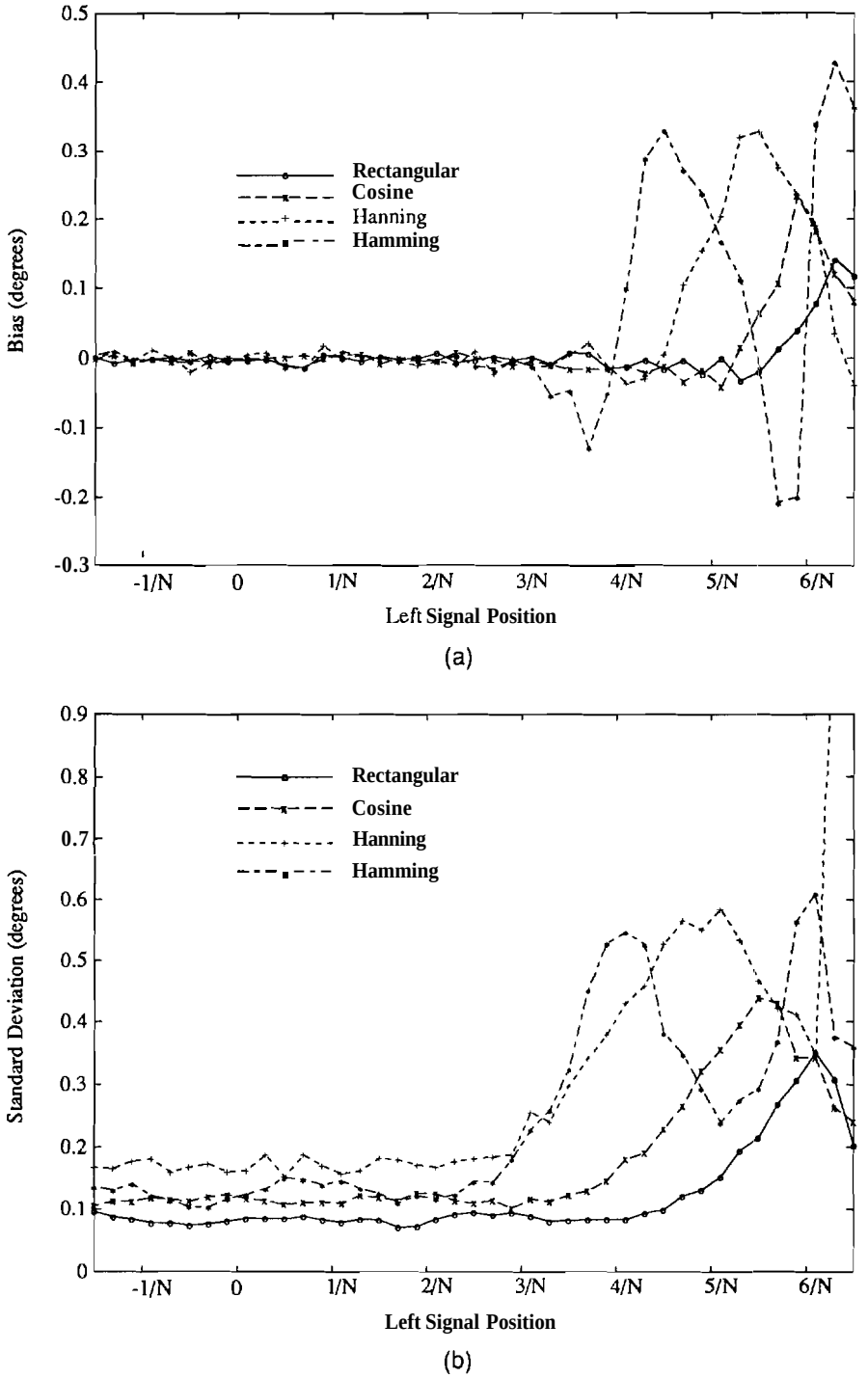

Figure 2.7 Performance of beamspace Root-MUSIC as a function of position of two uncorrelated half-Rayleigh sources (SNR = 6dB) within the subband $-10/N < u < 8/N$. $N_b = 5$ beams generated with weighting applied to the set shown in Figure 2.1(a). Statistics for the "left" source computed from 250 runs. (a) Sample bias. (b) Sample standard deviation.

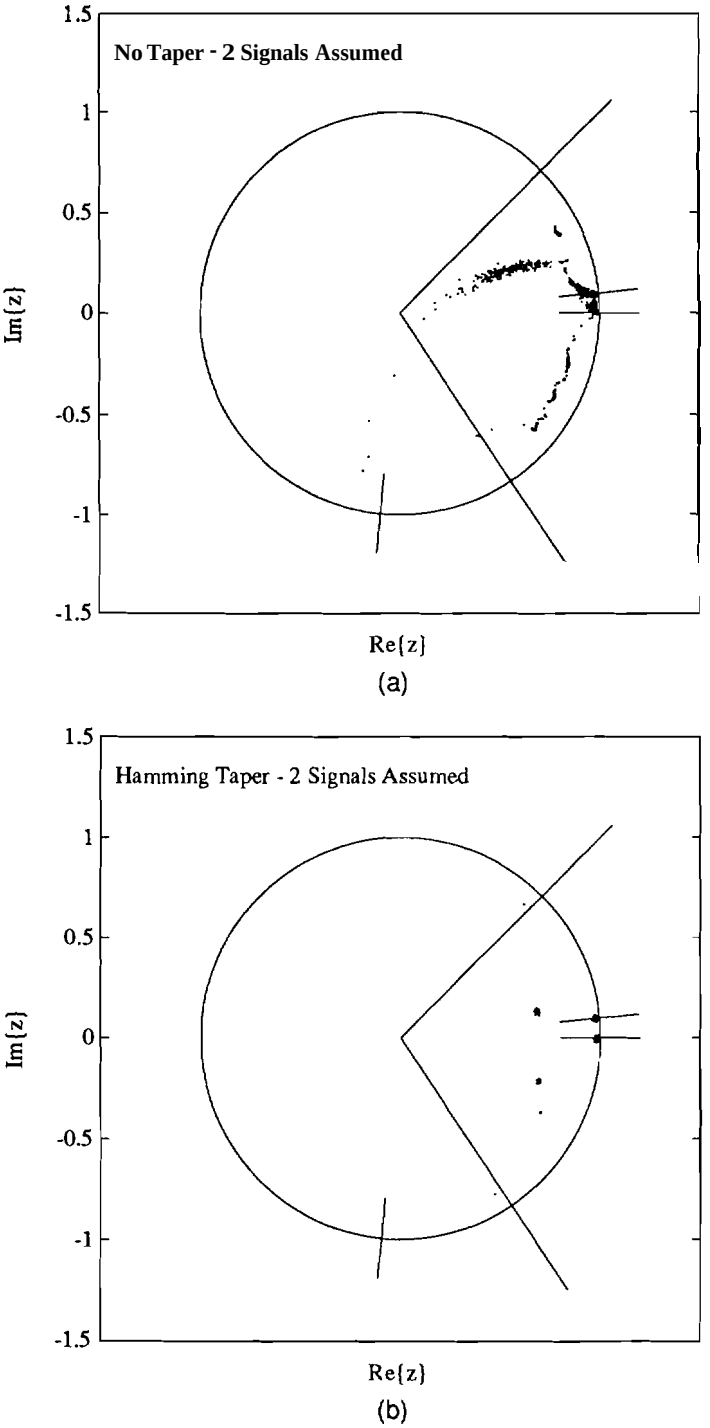

Figure 2.8 Beamspace Root-MUSIC scatter plots associated with the use of the rectangular and Hamming-weighted beam sets of Figures 2.1 (a) and (b). Two 6dB uncorrelated sources were located at 0 and $1/N$ while an 18dB out-of-band source was positioned at $-17/N$. The roots in 250 trial runs were computed assuming only 2 signals present. (a) no (rectangular) tapering, (b) Hamming taper

2.9 Summary

Procedures were presented for designing orthogonal matrix beamformers composed of conjugate centro-symmetric weight vectors and producing beams exhibiting coinmon out-of-band nulls, for use in conjunction with Root-MUSIC. The former property enables one to work with the real part of the beamspace sample covariance matrix in the eigenanalysis stage of Root-MUSIC, while the latter property yields a reduced degree polynomial in the final stage of Root-MUSIC. It should be noted that the use of conjugate centro-symmetric weight vectors allows one to work with the real part of the beamspace sample covariance matrix irrespective of the angle-of-arrival estimation algorithm employed. A number of matrix beamformers possessing the desirable features were derived from the N x N_b DFT matrix beamformer. For example, matrix beamformers yielding reduced out-of-band sidelobes were constructed by adding weighted, adjacent columns of the N x N_b DFT matrix beamformer. In addition, a procedure was developed for constructing a matrix beamformer possessing the aforementioned properties which allows the designer to specify a subset of the common null locations.

Note that all of the results in this chapter are easily modified if instead of the N x N_b DFT matrix beamformer $\mathbf{W}_R^{(m)}$ defined in (2.16), the prototype matrix beamformer was defined with each of the N_b corresponding pointing angles translated by the some fraction of the spatial DFT spacing $2/N$. All of the necessary properties are retained under such a translation. That is, it is not necessary to center the beams on DFT bins.

3. PERFORMANCE ANALYSIS OF BEAMSPACE ROOT-MUSIC EMPLOYING CONJUGATE SYMMETRIC BEAMFORMERS

3.1 Introduction

The quality of all high-resolution angle estimators is known to deteriorate as the correlation amongst the signals increases. A popular approach, used in element-space formulations, is to employ spatial smoothing [30, 31, 32]. A beamspace analogy to forward/backward averaging in element-space was noted in the previous chapter. There, the use of conjugate symmetric beamformers in conjunction with a uniformly-spaced linear array allows one to compute the noise eigenvectors as the "smallest" eigenvectors of the real part of the beamspace sample covariance matrix. It was shown that the effect of taking the real part of the beamspace covariance is equivalent to that obtained by first applying a forward/backward average in element-space prior to the beamspace transformation. Thus, a means to achieve signal decorrelation, as well as a savings in computation, is to employ a real eigenanalysis in beamspace. It should be noted that the class of conjugate centro-symmetric weight vectors is a very general one encompassing aperture tapering in accordance with any of the classical windows, Hamming, Kaiser, Chebyshev, etc. , and the class of discrete prolate spheroidal sequences as well [39, 25].

Due to the fact that the real part of the beamspace sample covariance matrix is not Wishart distributed, in general, it was not possible to merely cull previously derived results. However, the approach taken here is similar in nature to the pioneering work of Pillai and Kwon [8]. In [8], the asymptotic distribution of the element-space eigenvectors for a spatially sinoothed sample covariance matrix were derived and used to determine the bias and variance of the MUSIC null spectrum. The results in [8] cannot be directly transformed to apply to the case at hand unless the beamforming

preprocessor is a square matrix. Even in this non-typical case, the results would have to be adjusted to insure that the eigenvectors exhibit the required conjugate symmetry.

The spectral formulation of MUSIC is considered but, as shown in [10], the derived asymptotic variance applies to the Root-MUSIC form. As there is no specific uniform placement of sensors as dictated for application of Root-MUSIC, only a symmetric placement of sensors is assumed so that one can reap the computational/performance benefits associated with the processing of only the real-part of the beamspace sample covariance matrix.

An outline of Chapter **3** follows. The asymptotic statistics of the signal subspace eigenvectors pertaining to the real part of the beamspace sample covariance matrix are presented in Section 3.2.1 and derived in Appendix D. Targetting a beamspace MUSIC application, the asymptotic bias and variance of the beamspace MUSIC estimator incorporating real processing are derived in Section 3.2.2, followed by an observation and validation of the theoretical result's in Sections **3.3** and **3.4.** Realizing the need to attenuate clutter or strong signals that exist at distant locations in a sector-based processing scheme, the localization performance of several tapered beamforming architectures are studied in Section **3.5.**

For notational simplicity, the Spectral MUSIC algorithm incorporating the eigenvectors derived from the real-part of the beamspace sample covariance is termed as REAL-BS-MUSIC while that incorporating the eigenvectors of the complex covariance as COMPLEX-BS-MUSIC. Also, the notation "(m)" used to denote the processing of a particular (nz'th) subband is omitted.

3.2 Performance Analysis of Real Covariance Beamspace MUSIC

In this section, we derive the theoretical performance of the REAL-13s-MUSIC algorithm based upon a. finite sample estimate of the beamspace covariance. Aside from the computational advantages of processing only the real part of the beamspace covariance, a performance benefit, in terms of the estimation accuracy, was observed

through computer simulations as noted in the previous chapter. A theoretical analysis serves two purposes: (1) to offer an alternative to computationally burdensome computer simulations and (2) to provide a means to gain general insight into the operation of a particular direction finding algorithm and beamforming architecture.

Although the approach of using only the real part of the beamspace covariance matrix is general in nature so that it applies to all direction finding techniques used in conjunction with a symmetric array, we here consicler the application to spectral MUSIC only. The extension to other classes of algorithms is straightforward. The approach taken here, as similar to earlier studies [33, 34, 35, 36, 37], consists of two steps. First, the statistics of the eigenvalues and corresponding eigenvectors of the real part of the beamspace sample covariance matrix are derived. Second, the mean and variance of the angle estimate of beamspace MUSIC is obtained from a Taylor series expansion of the null spectrum. In Section 3.2.1, the statistics of the sample eigenvalues and eigenvectors in the signal subspace are derived, while the analysis of the MUSIC angle estimate is considered in Section 3.2.2.

3.2.1 Statistics of the Signal Subspace Eigenvalues and Eigenvectors

As a result of the normal distribution of the beamspace snapshot vector, the distribution of the complex sample covariance is Wishart [44]. It is well known that the asymptotic distribution of the non-repeated signal subspace eigenvalues and corresponding eigenvectors are normal [44]. Kaveh and Barabell [21] modified the asymptotic analysis to account for the unit length nature of the eigenvectors to derive the distribution of the MUSIC null spectrum. This led to a theoretical determination of the threshold SNR a.t which two closely spaced signals are resolved. Others [7, 33, 34] have employed the eigenvector statistics to determine the localization accuracy of MUSIC.

Note that the real part of the beamspace covariance matrix is not, in general, Wishart distributed. However, if the sources are uncorrelated the real part of the

sample covariance is effectively (real) Wishart with $2M$ degrees of freedom (see Appendix C). This compares with the M degrees of freedom of the (complex) Wishart distribution of the complex sample covariance. Recall that M is the number of snapshots. Pillai and Kwon [S] encountered and solved a problem that is similar. in nature to the one posed here in the prediction of the resolution threshold for element-space MUSIC incorporating spatial smoothing. Using a similar approach, one can show that the signal subspace eigenvalues and eigenvectors of the real part of the beamspace covariance matrix are also normal in an asymptotic sense. This leads to the main contribution of this chapter.

Theorem **2:** The asymptotic statistics of the error in the signal subspace eigenvectors, $\Delta\mathbf{e}_i = \hat{\mathbf{e}}_i - \mathbf{e}_i$, $i = 1, \ldots, K$, for the real part of the beamspace covariance matrix where (2.54) applies are

$$\mathcal{A}\mathrm{E}\{M\Delta\mathbf{e}_i\} = -\frac{1}{2}\sum_{\substack{k=1\\k\neq i}}^{N_b} \frac{\lambda_i\lambda_k}{(\lambda_i-\lambda_k)^2}\mathbf{e}_i + \frac{1}{2}\sum_{\substack{k=1\\k\neq i}}^{K} \frac{|\mathbf{e}_i^T\mathbf{R}_I\mathbf{e}_k|^2}{(\lambda_i-\lambda_k)^2}\mathbf{e}_i,\ i = 1,\ldots,K \quad [3.1]$$

$$\mathcal{A}\mathrm{E}\{M\,\Delta\mathbf{e}_k\Delta\mathbf{e}_\ell^T\} = \sum_{\substack{m=1\\m\neq k}}^{N_b}\sum_{\substack{n=1\\n\neq \ell}}^{N_b} \frac{\Gamma_{mn\ell k}}{(\lambda_k-\lambda_m)(\lambda_\ell-\lambda_n)}\mathbf{e}_m\mathbf{e}_n^T, \quad [3.2]$$

$$\begin{aligned}\Gamma_{mn\ell k} &= \frac{1}{2}\mathcal{R}e\{\,(\mathbf{e}_m^T\mathbf{R}_y\mathbf{e}_k)(\mathbf{e}_n^T\mathbf{R}_y^*\mathbf{e}_\ell)\,\} + \frac{1}{2}\mathcal{R}e\{\,(\mathbf{e}_m^T\mathbf{R}_y\mathbf{e}_\ell)(\mathbf{e}_n^T\mathbf{R}_y^*\mathbf{e}_k)\,\}\\ &= \frac{1}{2}\{\,\lambda_k\lambda_\ell\delta_{m\ell}\delta_{nk} + \lambda_k\lambda_m\delta_{mn}\delta_{k\ell}\\ &\quad + (\mathbf{e}_m^T\mathbf{R}_I\mathbf{e}_\ell)(\mathbf{e}_k^T\mathbf{R}_I\mathbf{e}_n)(1-\delta_{m\ell})(1-\delta_{kn})\\ &\quad + (\mathbf{e}_m^T\mathbf{R}_I\mathbf{e}_n)(\mathbf{e}_k^T\mathbf{R}_I\mathbf{e}_\ell)(1-\delta_{mn})(1-\delta_{k\ell})\,\}, \text{ and}\end{aligned} \quad [3.3]$$

$$\mathbf{R}_I = \mathcal{I}m\{\mathbf{R}_y\} = \mathbf{B}\,\mathcal{I}m\{\mathbf{P}_S\}\,\mathbf{B}^T, \quad [3.4]$$

where the notation AE refers to the asymptotic, in M, expectation.

Proof: See appendix D.

For purposes of comparison, the statistics of the corresponding quantities derived from the complex sample covariance are [34]

$$\mathcal{A}\mathcal{E}\{M\,\Delta\mathbf{e}_i^c\} = -\frac{1}{2}\sum_{\substack{k=1\\k\neq i}}^{N_b} \frac{\lambda_i^c\lambda_k^c}{(\lambda_i^c-\lambda_k^c)^2}\mathbf{e}_i^c \quad [3.5]$$

$$\mathcal{A}\mathrm{E}\{M\,\Delta\mathbf{e}_k^c\Delta\mathbf{e}_\ell^{cH}\} = \delta_{k\ell}\sum_{\substack{m=1\\m\neq k}}^{N_b}\frac{\lambda_m^c\lambda_k^c}{(\lambda_k^c-\lambda_m^c)^2}\,\mathbf{e}_m^c\mathbf{e}_m^{cH} \quad \text{and} \qquad [3.6]$$

$$\mathcal{A}\mathrm{E}\{M\,\Delta\mathbf{e}_k^c\Delta\mathbf{e}_\ell^{cT}\} = \frac{-\lambda_k^c\lambda_\ell^c}{(\lambda_k^c-\lambda_\ell^c)^2}\,\mathbf{e}_\ell^c\mathbf{e}_k^{cT}\,(1-\delta_{k\ell}), \qquad [3.7]$$

where $\mathbf{E}_S^c = [\mathrm{ef}|\mathbf{e}_2^c|\ldots|\mathbf{e}_K^c]$ and the superscript "c" has been included to refer to the eigenquantities originating from the complex beamspace sample covariance.

Notice that for the case of uncorrelated signals, the beamspace covariance is real-valued so that $\mathbf{R}_I = \mathbf{0}$. Thus, in the uncorrelated signal case, the expressions for the asymptotic bias in the signal eigenvectors are the same while the eigenvector variance statistics are similar in structure with the only difference being the multiplication factor $\frac{1}{2}$; the asymptotic variance of the eigenvectors is reduced by a factor of 2 when the real part of the covariance matrix is eigendecomposed. This fact would seem to indicate that a performance benefit in terms of the MUSIC angle estimate should be realized in an uncorrelatecl signal scene. We will observe that this statement is true in the case of the bias of the angle estimate (also proven by an alternate approach in Appendix C) but it is not true for the case of the variance of the angle estimate. In situations where the signals arc correlated with complex-valued terms on the off-diagonal of the source correlation matrix $\mathbf{P}_S$, it is not readily apparent that taking the real part results in a localization performance benefit. This issue will be addressed in more detail in the next section.

3.2.2 Mean and Variance of the Spectral MUSIC Angle Estimate

The derivation of the mean and variance of the Spectral MUSIC angle estimate is presented in this section. The approach taken is identical to that in [34] so little explanation or detail is included. As successfully applied elsewhere [33, 34, 35], the first derivative of the MUSIC null spectrum, i.e., the denominator of the MUSIC spatial spectrum, with respect to the location angle θ, is expanded in a Taylor series. Xu and Buckley [34] employed a multivariate second-order expansion of the derivative of the null spectrum in terms of the error in the i^{th} angle estimate, $\Delta\theta_i$, as well as the error in the signal subspace eigenvectors to derive both the bias and variance

of the estimator. The notable difference between the case at hand and that of the element-space version in [34] is that their expansion dealt with the differentiation of a real-valued function of complex-valued terms whereas our expression contains only real-valued variables. However, the expressions for the eigenvector statistics for real covariance processing are more complex, so the analysis is much more tedious. As similar to that in [34], we assume that the first and second derivatives of the beamspace manifold vector, $\dot{\mathbf{b}}(\theta)$ and $\ddot{\mathbf{b}}(\theta)$, respectively, exist.

As only the statistics of the signal subspace eigenvectors are available, one must consider the form of the MUSIC null spectrum, $D(\mathbf{E}_S, \theta)$, expressed as

$$D(\mathbf{E}_S, \theta) = \mathbf{b}^T(\theta) \left[\mathbf{I}_{N_b} - \mathbf{E}_S \mathbf{E}_S^T\right] \mathbf{b}(\theta), \qquad [3.8]$$

where $\mathbf{E}_S = \left[\mathbf{e}_1 \vdots \mathbf{e}_2 \vdots \ldots \vdots \mathbf{e}_K\right]$. The expansion of the null spectrum derivative is

$$\dot{D}(\hat{\mathbf{E}}_S, \hat{\theta}_i) = \dot{D}(\mathbf{E}_S, \theta_i) + \left\{ \ddot{D}(\mathbf{E}_S, \theta_i)\, \Delta\theta_i + \sum_{k=1}^{K} \left(\nabla_{\mathbf{e}_k} \dot{D}(\mathbf{E}_S, \theta_i)\right) \Delta\mathbf{e}_k \right\} +$$

$$\frac{1}{2!} \left\{ \dddot{D}\,(\mathbf{E}_S, \theta_i)\, (\Delta\theta_i)^2 + 2 \sum_{k=1}^{K} \left(\nabla_{\mathbf{e}_k} \ddot{D}(\mathbf{E}_S, \theta_i)\right) (\Delta\mathbf{e}_k \Delta\theta_i) + \right.$$

$$\left. \sum_{k=1}^{K} \sum_{\ell=1}^{K} \Delta\mathbf{e}_k^T \left(\nabla_{\mathbf{e}_\ell} [\nabla_{\mathbf{e}_k} \dot{D}(\mathbf{E}_S, \theta_i)]^T\right)^T \Delta\mathbf{e}_\ell \right\} + S. \qquad [3.9]$$

where the differentiation of D is with respect to 0, i.e., $\dot{D}(\hat{\mathbf{E}}_S, \hat{0},) = \frac{\partial}{\partial\theta} \dot{D}(\hat{\mathbf{E}}_S, \theta)\,|_{\theta=\hat{\theta}_i}$, $\mathbf{E}_S$ is an N_b x K matrix composed of the signal subspace eigenvectors, ∇ represents the vector gradient, and S is composed of the higher order terms. Carrying through the differentiation of the quantities in (3.9) using the definition in equation (3.8) leads to

$$\begin{aligned}
\dot{D}(\mathbf{E}_S, \theta_i) &= \dot{D}(\hat{\mathbf{E}}_S, \hat{\theta}_i) = 0 \\
\ddot{D}(\mathbf{E}_S, \theta_i) &= 2\dot{\mathbf{b}}(\theta_i) \left[\mathbf{I}_{N_b} - \mathbf{E}_S \mathbf{E}_S^T\right] \mathbf{b}(\theta_i) \\
\dddot{D}\,(\mathbf{E}_S, \theta_i) &= 6\ddot{\mathbf{b}}(\theta_i) \left[\mathbf{I}_{N_b} - \mathbf{E}_S \mathbf{E}_S^T\right] \dot{\mathbf{b}}(\theta_i) \\
\nabla_{\mathbf{e}_k} \dot{D}(\mathbf{E}_S, \theta_i) &= -2\dot{\mathbf{b}}(\theta_i) \mathbf{e}_k^T \mathbf{b}(\theta_i) - 2\mathbf{b}(\theta_i) \mathbf{e}_k^T \dot{\mathbf{b}}(\theta_i) \\
\nabla_{\mathbf{e}_k} \ddot{D}(\mathbf{E}_S, \theta_i) &= -4\dot{\mathbf{b}}(\theta_i) \mathbf{e}_k^T \dot{\mathbf{b}}(\theta_i) - 2\ddot{\mathbf{b}}(\theta_i) \mathbf{e}_k^T \mathbf{b}(\theta_i) - 4\mathbf{b}(\theta_i) \mathbf{e}_k^T \ddot{\mathbf{b}}(\theta_i) \\
\left(\nabla_{\mathbf{e}_\ell} [\nabla_{\mathbf{e}_k} \dot{D}(\mathbf{E}_S, \theta_i)]^T\right)^T &= -2[\mathbf{b}(\theta_i) \dot{\mathbf{b}}^T(\theta_i) + \dot{\mathbf{b}}(\theta_i) \mathbf{b}^T(\theta_i)] \delta_{k\ell}.
\end{aligned}$$

One can show that, with the aid of the asymptotic relations in the previous section, the first bracketted term in equation (3.0) is $O(\frac{1}{\sqrt{M}})$, i.e., if the random variable x is $O(\frac{1}{\sqrt{M}})$ then in the limit of M, (Ad x) is finite. Compare this to the meaning of $o(\frac{1}{\sqrt{M}})$ which indicates that such a random variable falls to zero in the limit faster than $\frac{1}{\sqrt{M}}$. In addition, the second bracketted term of (3.9) is $O(\frac{1}{M})$, while S is $o(\frac{1}{M})$.

The variance of the MUSIC angle estimate is obtained by working with the $O(\frac{1}{\sqrt{M}})$ term of the Taylor series expansion. In the same style as in [34] using the statistics of the error in the signal subspace eigenvectors described by equations; (3.1) and (3.2), the asymptotic variance of the REAL-BS-MUSIC estimator is derived as

$$\begin{aligned} \mathcal{A}\mathrm{Var}(\sqrt{M}\Delta\theta_i) &= \sum_{k=1}^{K} \frac{\lambda_k \sigma_n^2}{(\lambda_k - \sigma_n^2)^2} (\mathbf{e}_k^T \mathrm{b}(\theta_i))^2 \qquad [3.10] \\ &= \sigma_n^2 \mathrm{b}^T(\theta_i) \left\{ \sum_{k=1}^{K} \frac{\mathbf{e}_k \mathbf{e}_k^T}{\lambda_k - \sigma_n^2} + \sigma_n^2 \sum_{k=1}^{K} \frac{\mathbf{e}_k \mathbf{e}_k^T}{(\lambda_k - \sigma_n^2)^2} \right\} \mathrm{b}(\theta_i) \; i = 1, \ldots, K. \end{aligned}$$

As will be shown shortly, this result shows a remarkable resemblance to that obtained when eigendecoinposing the complex-valued covariance. It will be found useful to express (3.11) a.s diagonal elements of matrices a.s in [33]. In the decomposition of (2.57), it can be shown that

$$\begin{aligned} \sum_{k=1}^{K} \frac{\mathbf{e}_k \mathbf{e}_k^T}{\lambda_k - \sigma_n^2} &= \left\{ \mathbf{B} \mathbf{P}_{S_R} \mathbf{B}^T \right\}^{\dagger} = \mathbf{B}^{\dagger^T} \mathbf{P}_{S_R}^{-1} \mathbf{B}^{\dagger} \\ \sum_{k=1}^{K} \frac{\mathbf{e}_k \mathbf{e}_k^T}{(\lambda_k - \sigma_n^2)^2} &= \mathbf{B}^{\dagger^T} \mathbf{P}_{S_R}^{-1} \mathbf{B}^{\dagger} \mathbf{B}^{\dagger^T} \mathbf{P}_{S_R}^{-1} \mathbf{B}^{\dagger} = \mathbf{B}^{\dagger^T} \mathbf{P}_{S_R}^{-1} (\mathbf{B}^T \mathbf{B})^{-1} \mathbf{P}_{S_R}^{-1} \mathbf{B}^{\dagger}, \end{aligned}$$

where † denotes the Moore-Penrose pseutlo-inverse, $\mathbf{P}_{S_R}$ is the real part of the source correlation and $\mathbf{B}^{\dagger}$ is the left pseudoinverse of B, i.e., $\mathbf{B}^{\dagger} = (\mathbf{B}^T \mathbf{B})^{-1} \mathbf{B}^T$. Also notice that

$$\mathbf{B}^{\dagger} \mathbf{B} = \mathrm{I}_{\cdot\cdot} \qquad \mathbf{B}^{\dagger} \mathrm{b}(\theta_i) = \delta_i,$$

where δ_i is a. K x 1 vector where the i^{th} entry is 1 and the remaining components are zero. With these results, one can convert (3.11) to matrix form as

$$\mathcal{A}\mathrm{Var}(\sqrt{M}\Delta\theta_i) = \frac{\sigma_n^2}{\ddot{D}(\theta_i, \mathbf{E}_S)} \left[\mathbf{P}_{S_R}^{-1} + \sigma_n^2 \mathbf{P}_{S_R}^{-1} (\mathbf{B}^T \mathbf{B})^{-1} \mathbf{P}_{S_R}^{-1} \right]_{ii}, \qquad [3.11]$$

where $[\mathbf{H}]_{ij}$ denotes the (i,j) element of H and $\ddot{D}(\theta_i, \mathbf{E}_S)$ can alternatively be expressed as

$$\ddot{D}(\theta_i, \mathbf{E}_S) = 2\dot{\mathbf{b}}^T(\theta_i)(\mathbf{I}_{N_b} - \mathbf{B}\mathbf{B}^\dagger)\dot{\mathbf{b}}(\theta_i).$$

For comparitive purposes, the associated asymptotic variance for COMPLEX-BS-MUSIC is simply [33]

$$\mathcal{A}\mathrm{Var}(\sqrt{M}\Delta\theta_i^c) = \frac{\sigma_n^2}{\ddot{D}(\theta_i, \mathbf{E}_S^c)} \left[\mathbf{P}_S^{-1} + \sigma_n^2 \mathbf{P}_S^{-1}(\mathbf{B}^T\mathbf{B})^{-1}\mathbf{P}_S^{-1}\right]_{ii}, \qquad [3.12]$$

where $\ddot{D}(\theta_i, \mathbf{E}_S^c) = \ddot{D}(\theta_i, \mathbf{E}_S)$. The only difference is in the source covariance term. Much can be said about the expected performance of the two processing methodologies as will be seen shortly.

The bias of the MUSIC estimate is obtained, again, via a technique similar to that used in [34]. Taking the expectation of equation (3.9), using the asymptotic eigenvector error expressions of (3.1) and (3.2), and "matricizing" the result leads to

$$\begin{aligned}\mathcal{A}\mathrm{E}(M\Delta\theta_i) \;=\; & -\frac{\dddot{D}(\mathbf{E}_S, \theta_i)}{6\,\ddot{D}(\mathbf{E}_S, \theta_i)}\mathcal{A}\mathrm{Var}(\Delta\theta_i) \\ & - \frac{\sigma_n^2(N_b - K - 2)}{\ddot{D}(\mathbf{E}_S, \theta_i)}(\mathbf{B}^\dagger\dot{\mathbf{b}}(\theta_i))^T[\mathbf{P}_{S_R}^{-1} + \sigma_n^2\mathbf{P}_{S_R}^{-1}(\mathbf{B}^T\mathbf{B})^{-1}\mathbf{P}_{S_R}^{-1}]\boldsymbol{\delta}_i \\ & - \sum_{k=1}^{K}\sum_{\substack{\ell=1 \\ \ell\neq k}}^{K}\sum_{\substack{j=1 \\ j\neq\ell \\ j\neq k}}^{K} \frac{(\mathbf{e}_k^T\mathbf{R}_I\mathbf{e}_\ell)\,(\mathbf{e}_k^T\mathbf{R}_I\mathbf{e}_j)\,(\dot{\mathbf{b}}^T(\theta_i)\mathbf{e}_\ell\mathbf{e}_j^T\mathbf{b}(\theta_i))}{\ddot{D}(\mathbf{E}_S, \theta_i)\,(\lambda_k - \lambda_\ell)\,(\lambda_k - \lambda_j)} \end{aligned} \qquad [3.13]$$

The details of deriving this expression are tedious and are thus not included. The corresponding result for the COMPLEX-BS-MUSIC case converted to matrix form is [34]

$$\begin{aligned}\mathcal{A}\mathrm{E}(M\Delta\theta_i^c) = \; & -\frac{\dddot{D}(\mathbf{E}_S, \theta_i)}{6\,\ddot{D}(\mathbf{E}_S, \theta_i)}\mathcal{A}\mathrm{Var}(M\Delta\theta_i^c) \\ & - \frac{2\,\sigma_n^2(N_b - K - 1)}{\ddot{D}(\mathbf{E}_S, \theta_i)}(\mathbf{B}^\dagger\dot{\mathbf{b}}(\theta_i)^T)\mathcal{R}e\{\mathbf{P}_S^{-1} + \sigma_n^2\mathbf{P}_S^{-1}(\mathbf{B}^T\mathbf{B})^{-1}\mathbf{P}_S^{-1}\}\boldsymbol{\delta}_i. \end{aligned} \qquad [3.14]$$

The differences between these two expressions are (i) the scaling factor on the second term, (ii) the dependence on $\mathcal{R}e\{\mathbf{P}_S\}$ or $\mathbf{P}_S$ in the second term, and (iii) the presence of the third term in (3.13). Note that the latter term is only nonzero in scenarios involving at least three correlated sources.

3.3 Observations of the Theoretical Variance Equations

In this section, we look at several signal scenarios in an attempt to quantify the relative perforinance of the two algorithm types. The observations are made solely through the use of the theoretical expressions of the preceding section. Due to the more complex nature of the expressions for the bias, we limit the observations to apply to the estimate variance only. The relative performance with respect to the bias will be addressed via specific examples in Section **3.4.** We begin with the two-source case and then proceed into the general situation of three or more sources which we will separate into the correlated and uncorrelated classes. We will concentrate on the matrix formulations of the theoretical variance as given in equations **3.11** and **3.12.**

For the general correlated two-source case. the source covariance matrix $\mathbf{P}_S$ has the structure

$$\mathbf{P}_S = \begin{bmatrix} \sigma_1^2 & \rho^* \sigma_1 \sigma_2 \\ \rho \sigma_1 \sigma_2 & \sigma_2^2 \end{bmatrix}, \qquad [3.15]$$

where σ_1 and σ_2 are the powers of the two signals and ρ is the complex correlation coefficient. This signal model is representative of the low angle tracking scenario [38] where a low altitude target gives rise to both a direct and ground-reflected path signal. The two returns are highly-correlated and closely spaced in angle. In this situation, the magnitude of p, $0 \leq |\rho| \leq 1$, is often "close" to **1** and the phase depends on the path difference between the direct and specular path signals. Note that the restriction that $\mathbf{P}_S$ be a full rank matrix previously mentioned requires that $|\rho| < 1$. However, note that the real covariance technique outlined earlier would still function properly in the case of a rank one $\mathbf{P}_S$ as long as an imaginary component exists in ρ, i.e., the phase of p is not either 0 or π.

The following theorem shows that the REAL-BS-MUSIC algorithm offers a lower variance estimate relative to that of the COMPLEX-BS-MUSIC formulation for the general two-source scenario.

Theorem **3.** In the presence of two non-coherent sources, the asymptotic variances

of the REAL-BS-MUSIC and COMPLEX-BS-MUSIC estimators are related by

$$\mathcal{A}\mathrm{Var}(\sqrt{M}\Delta\theta_i) \leq \mathcal{A}\mathrm{Var}(\sqrt{M}\Delta\theta_i^c) \quad i = 1,2 \qquad [3.16]$$

with equality when the sources are uncorrelated or the correlation phase is 0 or π.

Proof: With regard to the structure of the general two-source correlation matrix of equation (3.15), the inverses $\mathbf{P}_S^{-1}$ and $\mathbf{P}_{S_R}^{-1}$ exist as guaranteed by the non-coherency of the signals and are

$$\mathbf{P}_S^{-1} = \frac{1}{\sigma_1^2\sigma_2^2(1-|\rho|^2)}\begin{bmatrix} \sigma_2^2 & -\rho\sigma_1\sigma_2 \\ -\rho^*\sigma_1\sigma_2 & \sigma_1^2 \end{bmatrix},$$

$$\mathbf{P}_{S_R}^{-1} = \frac{1}{\sigma_1^2\sigma_2^2(1-\rho_R^2)}\begin{bmatrix} \sigma_2^2 & -\rho_R\sigma_1\sigma_2 \\ -\rho_R\sigma_1\sigma_2 & \sigma_1^2 \end{bmatrix},$$

where ρ_R denotes the real part of the correlation coefficient, satisfying $|\rho_R| \leq |\rho|$ with equality if and only if the phase is 0 or π. The matrix $(\mathbf{B}^T\mathbf{B})^{-1}$ is a real-valued, positive definite matrix of the form $\left[(\mathbf{B}^T\mathbf{B})^{-1}\right]_{kl} = \beta_{kl}$. Substituting these expressions into (3.11) and (3.12) and simplifying leads to the following results for the first signal

$$\mathcal{A}\mathrm{Var}(\sqrt{M}\Delta\theta_1) = \frac{\sigma_n^2}{\ddot{D}(\theta_1,\mathbf{E}_S)}\left[\frac{1}{\sigma_1^2\sigma_2^2(1-\rho_R^2)} + \sigma_n^2\frac{\beta_{11}\sigma_2^2 - 2\beta_{12}\rho_R\sigma_1\sigma_2 + \beta_{22}\rho_R^2\sigma_1^2}{\sigma_1^4\sigma_2^2(1-\rho_R^2)^2}\right]$$

$$\mathcal{A}\mathrm{Var}(\sqrt{M}\Delta\theta_1^c) = \frac{\sigma_n^2}{\ddot{D}(\theta_1,\mathbf{E}_S^c)}\left[\frac{1}{\sigma_1^2\sigma_2^2(1-|\rho|^2)} + \sigma_n^2\frac{\beta_{11}\sigma_2^2 - 2\beta_{12}\rho_R\sigma_1\sigma_2 + \beta_{22}|\rho|^2\sigma_1^2}{\sigma_1^4\sigma_2^2(1-|\rho|^2)^2}\right]$$

As a result of $\ddot{D}(\theta_1,\mathbf{E}_S^c) = \ddot{D}(\theta_1,\mathbf{E}_S)$, $|\rho|^2 \geq \rho_R^2$, and $(1-|\rho|^2) \leq (1-\rho_R^2)$, it follows that $\mathcal{A}\mathrm{Var}(\sqrt{M}\Delta\theta_1^c) \geq \mathcal{A}\mathrm{Var}(\sqrt{M}\Delta\theta_1)$. Equality is seen to exist whenever $|\rho| = |\rho_R|$. Reversing the indices of the two signals proves the result for the second signal. Thus, aside from the computational savings of decomposing only the real part of the beamspace covariance, a performance benefit is expected a.s well □.

As similar to the two source case, the presence of uncorrelated signals, or more generally, in the case of a non-existent imaginary component to the source correlation matrix, no performance advantage relative to the variance in an asymptotic sense is realized for more than two signals. However, empirical results, as presented in the

following section, indicate that the bias in the angle estimate is usually smaller when processing only the real part. As noted earlier, the interplay of the various terms in (3.13) make it difficult to make general observations regarding the theoretical bias.

In the more general case of three or more correlated signals, the only claim one can make is that in a moderately high SNR situation, the asymptotic variance of REAL-BS-MUSIC is less than or equal to that of COMPLEX-BS-MUSIC. This observation is validated through the use of the matrix expressions of (3.11) and (3.12) as follows. As $\ddot{D}(\mathbf{E}_S, \theta_i)$ is exactly equal to $\ddot{D}(\mathbf{E}_S^c, \theta_i)$, one need only compare the terms in the numerators. We are attempting to prove $\mathrm{Var}(\Delta\theta_i) \stackrel{?}{\leq} \mathrm{Var}(\Delta\theta_i^c)$, which is true whenever [28]

$$\mathcal{R}e\left[\sigma_n^2\mathbf{P}_S^{-1} + \sigma_n^4\mathbf{P}_S^{-1}(\mathbf{B}^T\mathbf{B})^{-1}\mathbf{P}_S^{-1}\right] - \left[\sigma_n^2\mathbf{P}_{S_R}^{-1} + \sigma_n^4\mathbf{P}_{S_R}^{-1}(\mathbf{B}^T\mathbf{B})^{-1}\mathbf{P}_{S_R}^{-1}\right] \stackrel{?}{\geq} 0, \quad [3.17]$$

$$\sigma_n^2\left[\mathcal{R}e\{\mathbf{P}_S^{-1}\} - \mathbf{P}_{S_R}^{-1}\right] + \sigma_n^4\left[\mathcal{R}e\{\mathbf{P}_S^{-1}(\mathbf{B}^T\mathbf{B})^{-1}\mathbf{P}_S^{-1}\} - \mathbf{P}_{S_R}^{-1}(\mathbf{B}^T\mathbf{B})^{-1}\mathbf{P}_{S_R}^{-1}\right] \stackrel{?}{\geq} 0, \quad [3.18]$$

i.e., the difference of the two matrices is positive semi-definite[1]. Denoting the real and imaginary components of $\mathbf{P}_S$ as $\mathbf{P}_{S_R}$ and $\mathbf{P}_{S_I}$, respectively, where $\mathbf{P}_{S_R} = \mathbf{P}_{S_R}^T$ and $\mathbf{P}_{S_I} = -\mathbf{P}_{S_I}^T$, one can show that

$$\mathbf{P}_S^{-1} = [\mathbf{P}_{S_R} + \mathbf{P}_{S_I}\mathbf{P}_{S_R}^{-1}\mathbf{P}_{S_I}]^{-1} - j[\mathbf{P}_{S_R} + \mathbf{P}_{S_I}\mathbf{P}_{S_R}^{-1}\mathbf{P}_{S_I}]^{-1}\mathbf{P}_{S_I}\mathbf{P}_{S_R}^{-1}.$$

With regard to equation (3.18) observe that $\mathcal{R}e\{\mathbf{P}_S^{-1}\} - \mathbf{P}_{S_R}^{-1} \geq 0$, is equivalent to the condition that $\mathbf{P}_{S_R} - [\mathcal{R}e\{\mathbf{P}_S^{-1}\}]^{-1} \geq 0$. Indeed this is the case

$$\begin{aligned}\mathbf{P}_{S_R} - [\mathcal{R}e\{\mathbf{P}_S^{-1}\}]^{-1} &= \mathbf{P}_{S_R} - [\mathbf{P}_{S_R} + \mathbf{P}_{S_I}\mathbf{P}_{S_R}^{-1}\mathbf{P}_{S_I}] \\ &= -\mathbf{P}_{S_I}\mathbf{P}_{S_R}^{-1}\mathbf{P}_{S_I} \\ &= \mathbf{P}_{S_I}^T\mathbf{P}_{S_R}^{-1}\mathbf{P}_{S_I} \geq 0.\end{aligned}$$

The remaining term in equation (3.18), $\mathcal{R}e\{\mathbf{P}_S^{-1}(\mathbf{B}^T\mathbf{B})^{-1}\mathbf{P}_S^{-1}\} - \mathbf{P}_{S_R}^{-1}(\mathbf{B}^T\mathbf{B})^{-1}\mathbf{P}_{S_R}^{-1}$, is indefinite, so that one cannot conclude that $\mathrm{Var}(\Delta\theta_i)$ is less than $\mathrm{Var}(\Delta\theta_i^c)$. However,

[1] If the real-valued matrix $\mathbf{A}$ is positive semi-definite, then $\mathbf{y}^T\mathbf{A}\mathbf{y} \geq 0 \ \forall\mathbf{y}$. Selecting y as $\boldsymbol{\delta}_i$ yields the desired result.

note that $\sigma_n^2 \mathbf{P}_{S_R}^{-1}$ is loosely interpreted as being proportional to 1/SNR relative to the $1/(\text{SNR})^2$ nature of $\sigma_n^4 \mathbf{P}_{S_R}^{-1}(\mathbf{B}^T\mathbf{B})^{-1}\mathbf{P}_{S_R}^{-1}$. Thus, in cases where the signal power is sufficiently large relative to the noise, the first term in equation (3.18) dominates so that $\text{Var}(\Delta\theta_i) \leq \text{Var}(\Delta\theta_i^c)$.

3.4 Validation of the Theoretical Expressions

Computer simulations were carried out in order to verify the theoretical expressions for the bias and variance of the REAL-BS-MUSIC angle estimate as well as to provide additional insight into the comparison of the REAL-BS-MUSIC and COMPLEX-BS-MUSIC algorithm formulations. A uniform linear array of $N = 32$ half-wavelength spaced sensors was employed in conjunction with $N_b = 4$ conjugate centro-symmetric weight vectors to form beams with no tapering at sine space angles of $u = \sin 6 = -4/N, -2/N, 0, \text{and}, 2/N$. Two sources were included in each simulation and were angularly separated by half of the 3 dB beamwidth in sine space. Unless otherwise noted, the sample biases and standard deviations were coinputed over 250 independent trials. As noted on the figures, solid/dashed lines represent the theoretical curves while the empirical results are indicated with a "x"/"o" corresponding to the COMPLEX-BS-MUSIC/REAL-BS-MUSIC algorithms.

Figures 3.1 and 3.2 present the theoretical bias and standard deviation as well as the empirical standard deviation of the left-hand signal for the case of a highly correlated signal set. The strengths of the equipowered sources was 8 dB on a per sensor basis while the magnitude of the correlation coefficient, ρ, was set at 0.9. The phase of ρ was varied from 0 to 180 degrees to examine the dependence of performance on the phase.

The theoretical standard deviation curves plotted in Figure 3.1 predict a roughly quadratic. improvement in performance of REAL-BS-MUSIC over COMPLEX-BS-MUSIC as the correlation coefficient approaches the state of being purely imaginary at a phase difference of 90 deg. Also, in accordance with prior discussion, there is no difference in performance when the correlation coefficient is purely reitl as is the

case at phase differences of 0 cleg and 180 cleg. With respect to the estimate bias, the theoretical performance curves in Figure 3.2 predict that REAL-BS-MUSIC offers a lower bias than COMPLEX-BS-MUSIC for phase differences less than 150 deg with the greatest improvement occurring at a phase difference of 0 deg. The magnitude of the bias, however, is very small, almost negligible: high-bias conditions occur in situations where the systein parameters of two or more signals lie in the region of the resolution threshold. In this situation, the signals are on the edge of merging into one displayed peak in the MUSIC spectrum. We will return to this issue as well as present a comparison of the theoretical and empirical bias results shortly.

The theoretical standard deviation curves and corresponding simulation results plotted in Figure **3.3** substantiate claims made earlier that REAL-BS-MUSIC offers no improvement over COMPLEX-BS-MUSIC with respect to variance in the case of uncorrelated sources wherein the source covariance matrix is purely real. Note that the simulation results closely track the theoretically predicted performance as the number of snapshots decreases to as small as 20 with equi-powered 12 dB source SNR's. In contrast to the situation with variance, the theoretical bias curves in Figure 3.4 predict that REAL-BS-MUSIC offers a slightly lower bias in the case of uncorrelated sources than that achieved with COMPLEX-BS-MUSIC with the differential between the two increasing as the number of snapshots decreases or as the SNR is lowered. Once again, note that the bias is very small.

The theoretical and empirical results of Figure 3.4 begin to deviate as the number of snapshots reduces to 20. Recall that the theoretical expression:; for the bias and variance are asymptotic in nature so that a deviation is to be expected. However, the expressions are still valid if the source SNR's arc sufficiently large – this is the main point of Figure **3.5** where the number of snapshots was held constant at 20 while the source SNR was varied. Notice the deviation at the low end of the SNR scale. The deviation is caused by the fact that the simulation parameters are in the vicinity of the resolution threshold. In this region of operation, the two signal. peaks are on the verge of merging into a single peak in the MUSIC spectrum. When only peak exists,

the signals are said to be unresolved. A plot of the empirical probability of resolution, i.e., the percentage of cases where two signals are resolved, is shown in Figure ***3.7.*** Here we see that the onset of the deviation in the theoretical and empirical results directly corresponds to the SNR location where unresolved cases begin to appear. Also note that Figure ***3.7*** shows that REAL-BS-MUSIC is substantially more capable of resolving two signals than the COMPLEX-BS-MUSIC formulation.

Figure ***3.6*** shows the empirical and theoretical mean of the two MUSIC angle estimators that apply to the simulation results of Figures ***3.5*** and ***3.7.*** This figure clearly shows the merging of the two signal peaks as the SNR is reduced. It is necessary to go to this extreme to generate a high-bias case.

Once again, these simulations show the value of employing the REAL-BS-MUSIC algorithm over CONIPLEX-BS-MUSIC. The deviation between the theoretical and empirical curves is expected as due to earlier comments. Although the theoretical curves may not track the corresponding simulation curves, it is obvious that the theoretical expressions as are still valuable as the general trends are indicative of the obtained empirical results.

A few other comments regarding the cause of the deviation in the high-bias case are in order. The theoretical expressions are asymptotic in nature so that one may expect that the experimental and theoretical curves may be more in agreement if the number of snapshots is increased. This deviation, however, was found to exist with large M. Nor is there a. problem of not using a sufficient number of trials to estimate the bias, i.e., the variance of the bias estimate is too large – the same observations were made when using a greater number of trials. It is believed that the method of generating the empirical results is also flawed in nature. Unresolved cases where one centrally located peak is resolved must be included in the tabulation of the empirical statistics, but some trials show a single peak whose location bears little relation to one or both signals. However, these cases are still considered.

The simulations thus validate the theoretical performance expressions and illustrate the performance gains achieved via the use conjugate centro-symmetric beamforming vectors and executing beamspace MUSIC with only the: real part of the beamspace sample covariance matrix.

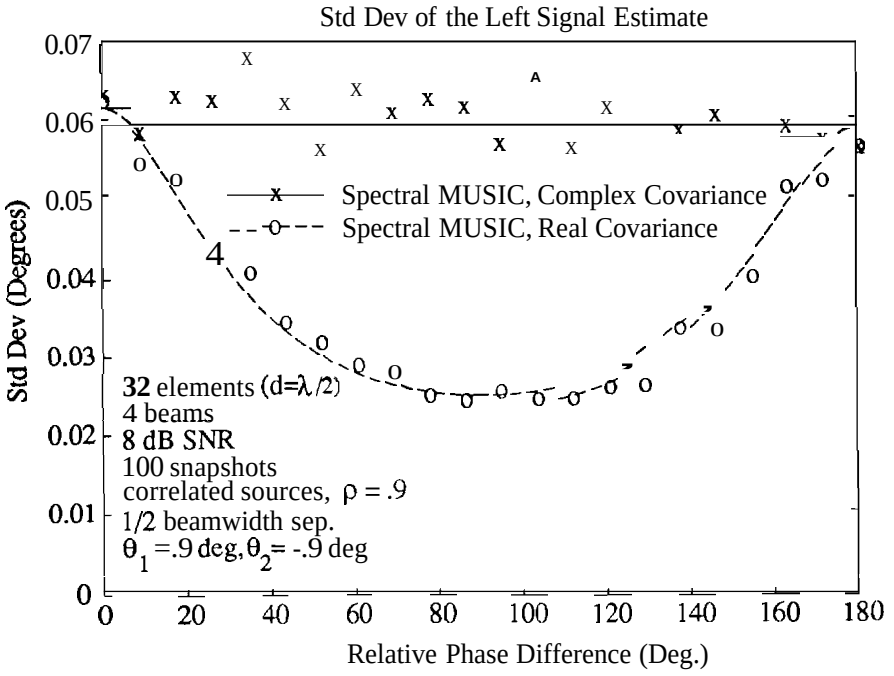

Figure 3.1 Real vs. complex processing: standard deviation as function of phase difference between two correlated signals.

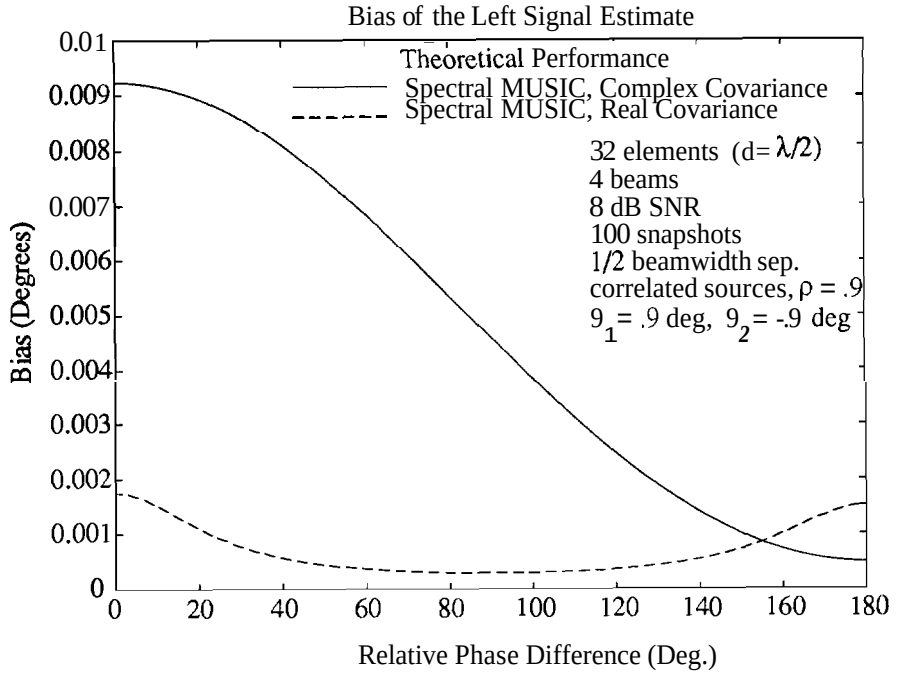

Figure 3.2 Real vs. complex processing: bias as function of phase difference between two correlated signals.

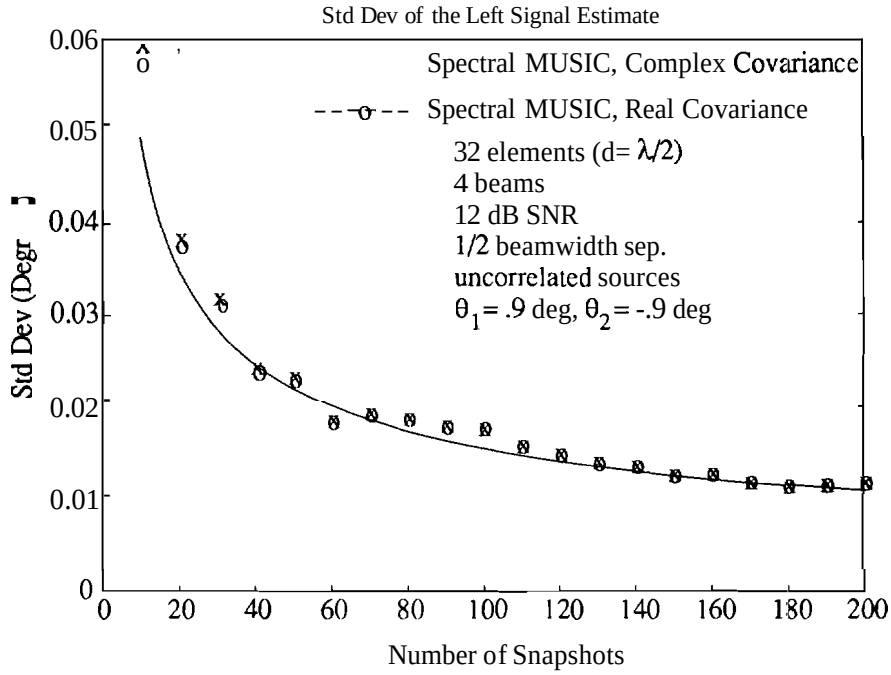

Figure **3.3** Real vs. complex processing: standard deviation as function of snapshots for two uncorrelated signals.

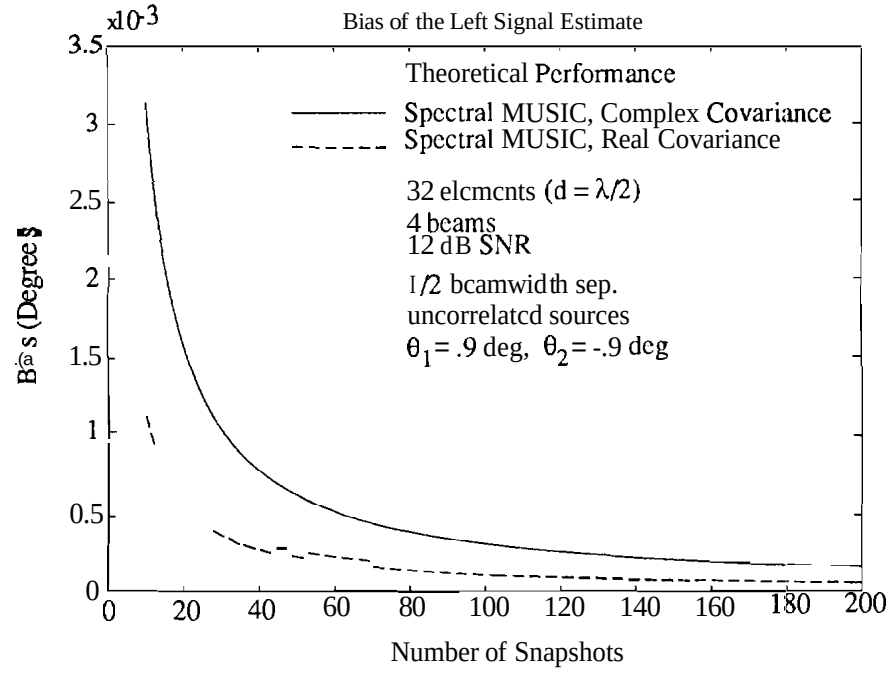

Figure **3.4** Real vs. complex processing: bias as function of snapshots for two uncorrelated signals.

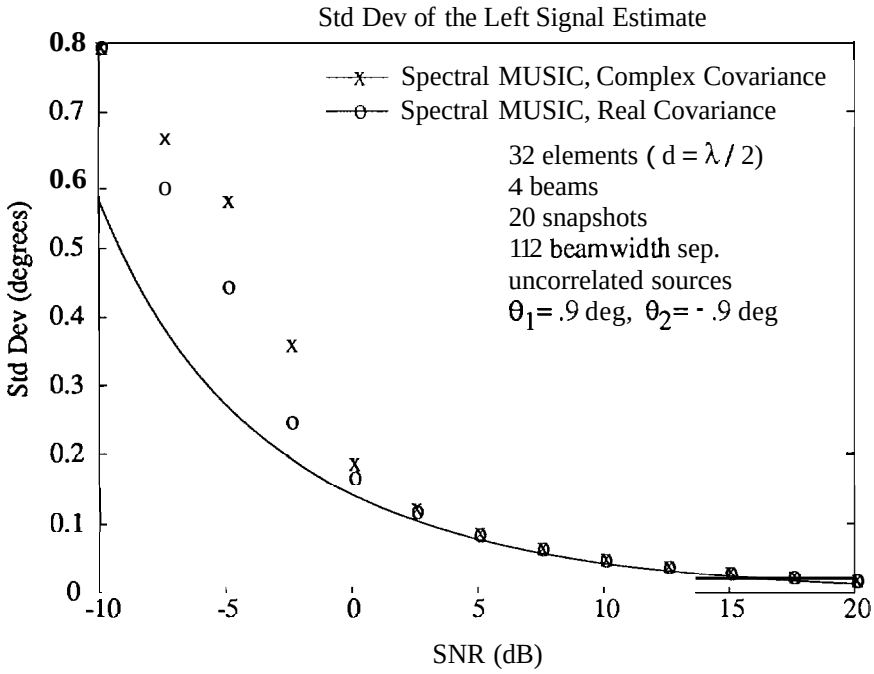

Figure 3.5 Real vs. complex processing: standard deviation as function of SNR for two uncorrelated signals.

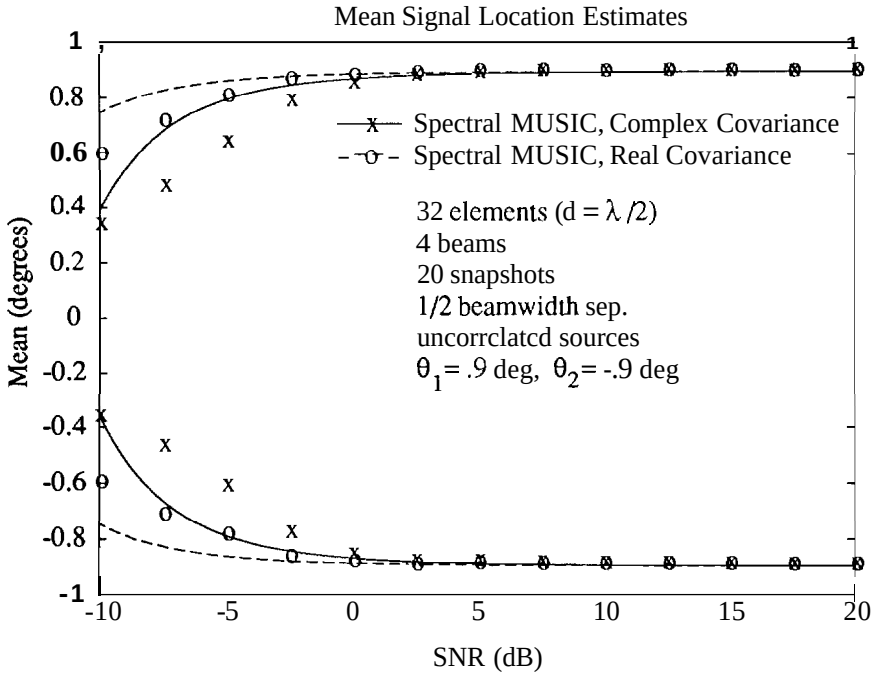

Figure 3.6 Real vs. complex processing: bias as function of SNR for two uncorrelated signals.

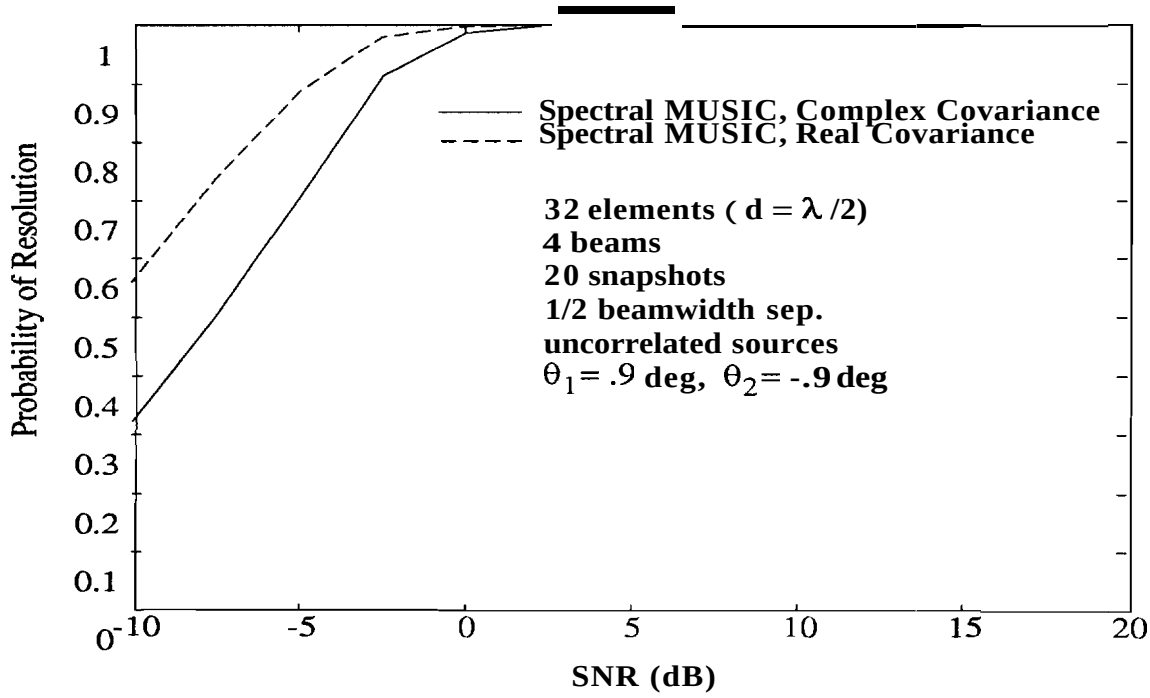

Figure 3.7 Real vs. complex processing: probability of resolution as function of SNR for two uncorrelated signals.

3.5 Merit of Employing Tapered Beamformers

Realizing the need to de-emphasize extended clutter returns and high-strength signals that arrive from directions outside of the spatial sector of interest: the use of tapered beamformers is advised. The presence of these additional signals decrease the number of degrees of freedom and, in the worst case, yields a non-functional MUSIC estimator due to the non-existence of a noise only subspace. A few candidate tapering architectures and their effect on the angle estimate bias and variance are investigated in this section. We assume a linear, equi-spaced array to take advantage of a computationally efficient implementation scheme.

Stoica and Nehorai [28] showed that the element-space MUSIC algorithm has an associated estimator variance that is less than or equal to that for a beamspace formulation with equality when the A' x N_b beamspace transformation $\mathbf{W}$ satisfies $\mathbf{W}\mathbf{W}^{\mathrm{H}} = \mathbf{I}_N$, i.e., N_b = N. Noticing that a full N x N spatial DFT matrix satisfies this constraint, we shall compare the performance of the candidate architectures against that using the N x N spatial DFT matrix. Notice that if the columns of the DFT matrix are made to be conjugate centro-symmetric, the real part of the associated beamspace covariance can be employed thus taking advantage of the lower bias in the case of uncorrelated signals. Although the N x N DFT transformation may provide a lower variance estimate, the use of a smaller dimension transformation matrix leads to a lower SNR resolution threshold [7] in addition to the lower computational requirements associated with the eigendecomposition.

In addition to beamforming with a N x N_b matrix $\mathbf{W}_{R_{N_b}}$ representing N_b successive columns of the N x N un-weighted DFT, i.e., the (R)ectangular taper, we consider the use of cosine and Hamming tapers of Section 2.6. As observed in Section 2.6, the cosine and Hamming tapers can be realized in the beamspace domain by summing weighted successive DFT beams. Specifically, the A' x N_b Hamming-weighted and N x (N_b – 1) cosine-weighted transformations are, respectively,

$$\mathbf{W}_{H_{N_b}} = \mathbf{W}_{R_{N_b+2}}\,\mathbf{T}_H^T \qquad [3.19]$$

$$\mathbf{W}_{C_{N_b-1}} = \mathbf{W}_{R_{N_b}} \mathbf{T}_C^T \quad [3.20]$$

$$\mathbf{T}_H = \begin{bmatrix} 0.23 & 0.54 & 0.23 & 0 & 0 & \dots & 0 & 0 & 0 \\ 0 & 0.23 & 0.54 & 0.23 & 0 & \dots & 0 & 0 & 0 \\ \vdots & \vdots & \vdots & \vdots & \vdots & \dots & \vdots & \vdots & \vdots \\ 0 & 0 & 0 & 0 & 0 & \dots & 0.23 & 0.54 & 0.23 \end{bmatrix} \quad N_b \times (N_b+2) \quad [3.21]$$

$$\mathbf{T}_C = \begin{bmatrix} 0.5 & 0.5 & 0 & 0 & \dots & 0 & 0 \\ 0 & 0.5 & 0.5 & 0 & \dots & 0 & 0 \\ \vdots & \vdots & \vdots & \vdots & \dots & \vdots & \vdots \\ 0 & 0 & 0 & 0 & . & 0.5 & 0.51 \end{bmatrix} \quad (N_b-1) \times N_b. \quad [3.22]$$

Note that we intend $\mathbf{W}_{R_{N_b+2}}$ to be an N x $(N_b + 2)$ matrix cornposed of $N_b + 2$ successive columns of the symmetrized spatial DFT matrix, with an extra beam on each side of the window relative to $\mathbf{W}_{R_{N_b}}$, so that the pointing angles of the beams via, $\mathbf{W}_{H_{N_b}}$ are aligned with those of $\mathbf{W}_{R_{N_b}}$. Thus, application of $\mathbf{W}_{H_{N_b}}$ yields a beamspace snapshot of the same dimension as that obtained with $\mathbf{W}_{R_{N_b}}$. On the other hand, the cosine-tapered transformation yields a beamspace snapshot of dimension $N_b - 1$. To see the effect of the sector size on the theoretical bias and variance, a N x $(N_b - 2)$ Hamming-weighted beamformer, $\mathbf{W}_{H_{N_b-2}}$, is also investigated.

Note that the sets of beamforming vectors are not orthogonal. Thus the beamspace noise, i.e., the element-space noise vector operated on by the tapered beamspace transformation, is not uncorrelated from beam-to-beam. In order for the theoretical expressions of Section **3.3** to be valid, one must orthogonalize the tapered beamforming matrices. This is accomplished quite simply: the resulting effective beamforming matrices with a re-definition of notation. are

$$\mathbf{W}_{H_{N_b}} = \mathbf{W}_{R_{N_b+2}} \mathbf{T}_H^T (\mathbf{T}_H \mathbf{T}_H^H)^{-1/2} \quad [3.23]$$

$$\mathbf{W}_{C_{N_b-1}} = \mathbf{W}_{R_{N_b}} \mathbf{T}_C^T (\mathbf{T}_C \mathbf{T}_C^H)^{-1/2}. \quad [3.24]$$

Plots of the spatial response patterns of the three (effective) tapering techniques is provided in Figures 3.8 a), b), and c). Note that the beamspace dimensionality is $N_b = 8$ for an $N = 32$ sensor array. As observed in Figure 3.8, the weighting functions

provided at least 15 dB of additional attenuation across the region of space outside of the sector $\sin 0 \in [-10/N, 8/N]$.

The theoretical bias and variance of the MUSIC angle estimate were computed and plotted in Figures 3.9 and 3.10 for the case of two uncorrelated and equi-powered signals separated by half the Rayleigh resolution $(1/N)$. Although only M = 16 snapshots were assumed, the signal strength (6 dB) was sufficient to yield an accurate prediction of performance, i.e., we are operating above the resolution threshold. The bias and variance of the left signal estimate was plotted against the sine-space midpoint position of the two signals.

The N_b consecutive, un-weighted DFT beams are as effective as the full N dimensional DFT transformation at locations where the sine-space center of the two signals are aligned with a lobe of a particular DFT lseam. The deviation in the bias and variance curves is minimal outside of these regions so that the savings in computation and anticipated reduction in the resolution threshold suggests the use of a lower dimensional beamformer. The poor performance at the edges of the sector is driven by the reduced signal power, proportional to $|\mathrm{b}(\theta)|^2$. Thus, in a search operation, sectors should be overlapped by somewhere between 25% and 50% to provide adequate performance.

As expected, the Hamming and cosine tapering architectures reduce the localization performance, but only slightly. The $\mathrm{A}^{\mathrm{r}}_{\mathrm{b}}$ Hamming beams, for example, are less sensitive in relation to the standard DFT beams to small variations in signal positioning within the sector. Obviously, then, MUSIC prefers the use of beams with, individually, high resolution. Note, though, that the presence of strong signals outside the sector of interest would warrant tapering as these signals, if unaccounted for in the estimation of the signal subspace dimensionality, may result in poorer performance for the unweighted beamformer as was shown in Section 2.8.

Comparison of the two Hamming taper cases suggests that a larger dimension beamformer is desired in terms of the expected bias and variance. This is a result of the additional signal information in the extra beams. I-Iowever, if the power of the

signals are in the region of the resolution threshold, the noise will dominate in these additional beams and provide no beneficial information. Thus, the use of fewer beams leads to a reduced resolution threshold. In conclusion, the need for the increased rejection of sidelobe clutter/high strength signals is achieved through tapering with only a modest decrease in the bias and variance performance of in-band signals relative to either the N_b or N dimensional unweighted spatial DFT beamformer.

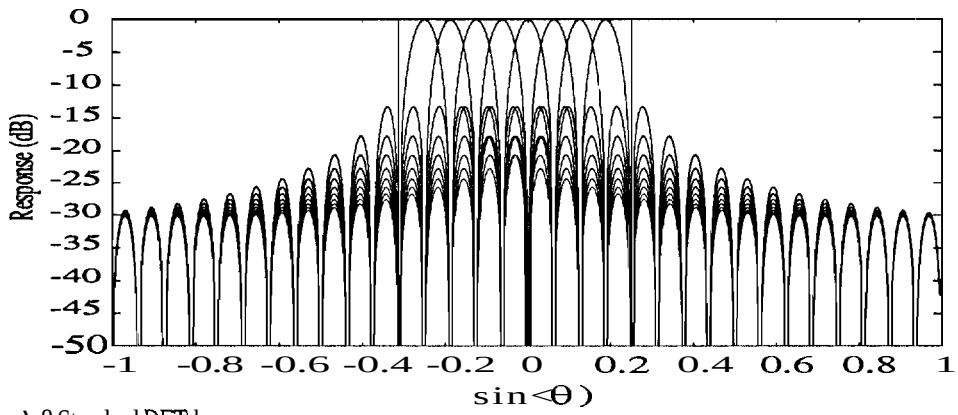

a) 8 Standard DFT beams

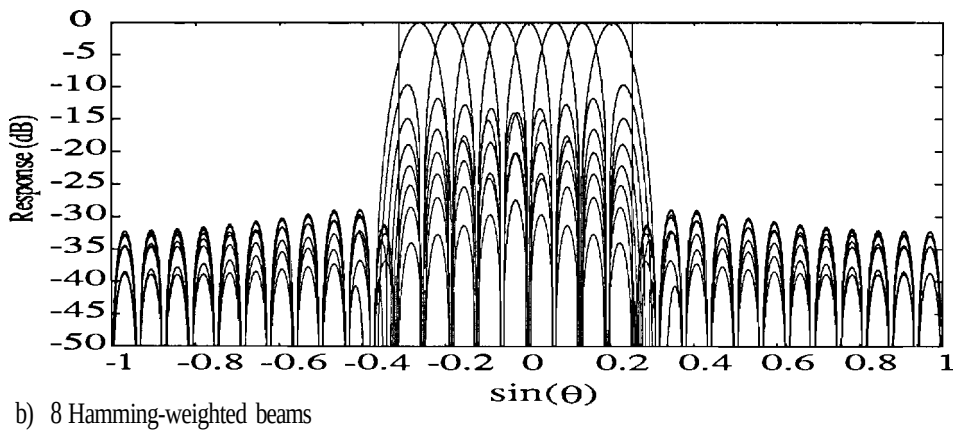

b) 8 Hamming-weighted beams

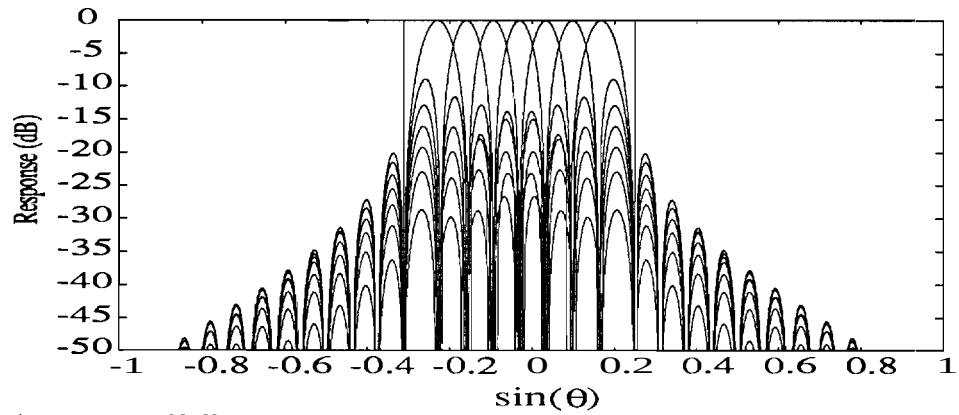

c) 7 Cosine-weighled beams

Figure **3.8** Candidate beamforming architectures for sector-based processing.

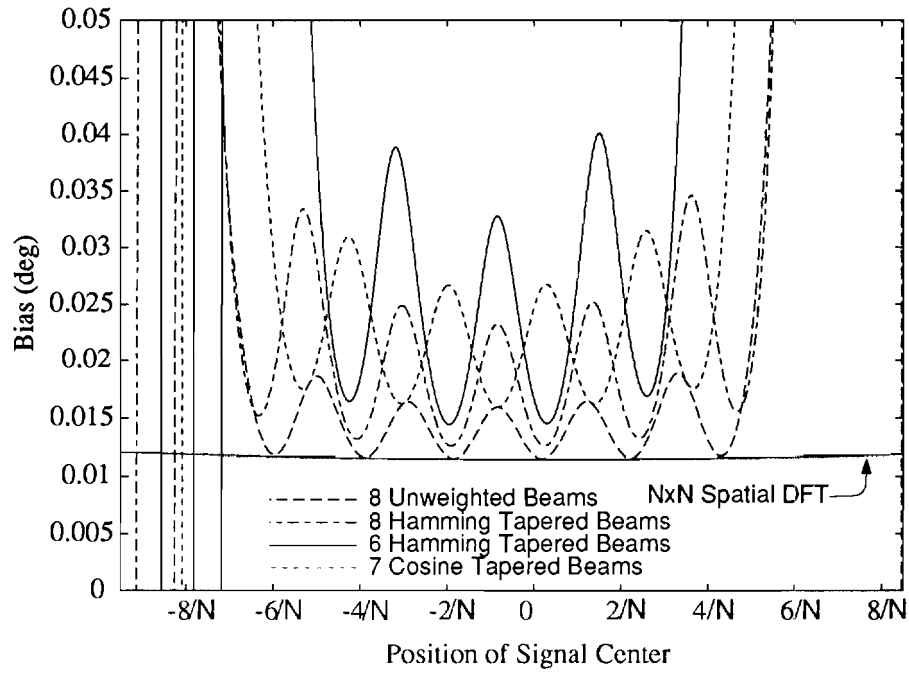

Figure 3.9 Theoretical bias of left signal estimate for various beamforming preprocessors.

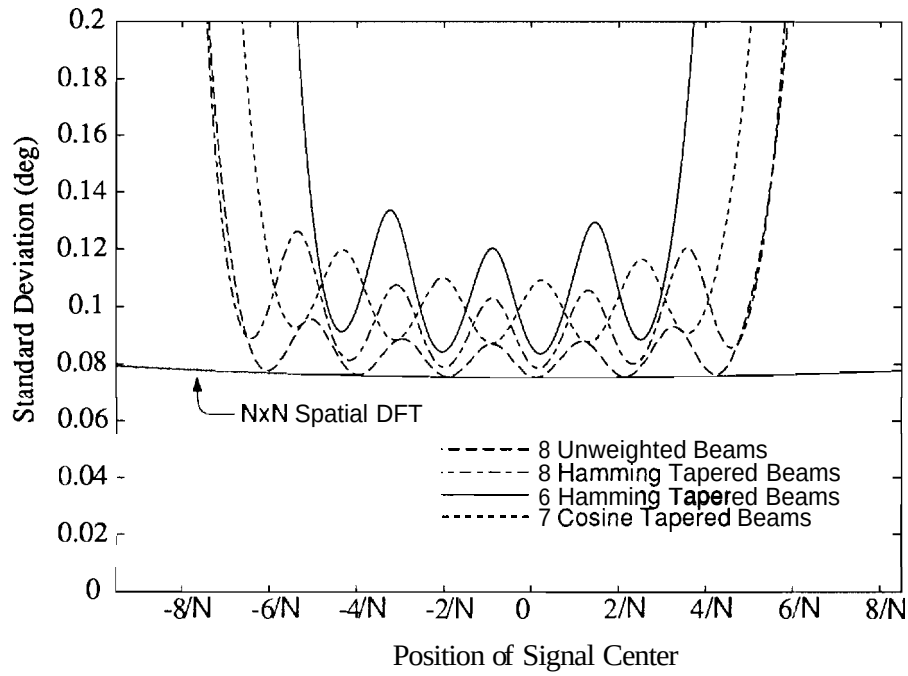

Figure 3.10 Theoretical std. dev. of left signal estimate for various beamforming preprocessors.

3.6 Summary

In this chapter, the asymptotic distribution of the signal subspace eigenvectors corresponding to the real part of the beamspace sample covariance was derived. The operation of processing only the real part is permissible in situations where: the beamforming vectors exhibit conjugate centro-symmetry. The asymptotic statistics were used to show the merit of such a technique with regard to the estimate bias and variance when used in conjunction with beamspace MUSIC. The idea of decomposing only the real part, however, is general in nature so that it applies to all eigenstructure direction finding techniques.

To fully realize the advantages of employing a beamspace preprocessor, one should incorporate a weighting function to insure that clutter and/or strong spatially-distant signals do not degrade the performance of the estimation algorithm. The 'issue of designing beamspace preprocessors to yield an architecture with the lowest resolution threshold was considered in [7, 29]. One such preprocessor is based upon the theory of discrete prolate spheroidal wave functions [39, 25]. In this approach, one would employ a N x $(K + 1)$ beamformer to localize K closely-spaced signals. However, it was determined that such aachitectures, although attractive in terms of the resolution threshold, yield an estimator with a. significantly higher bias and variance when operating above the threshold. Candidate tapering functions that provide considerable rejection levels yet yield comparable bias and variance figures were presented. Note also that these taper functions can be applied to a. set of adjacent spatial FFT beams to yield a computationally efficient procedure.

4. BEAMSPACE DOA ESTIMATION FEATURING MULTIRATE EIGENVECTOR PROCESSING

4.1 Introduction

Chapter 2 was partly concerned with the derivation of an efficient algorithm to reduce the order of the Root-MUSIC polynomial to $2N_b - 2$, which can represent a tremendous computational savings if only a few beams are formed in the direction of a previously detected signal to obtain a refined location estimate. The approach was accomplished by requiring that the beamforming vectors possess common spatial nulls. Notice that, as common to this beamspace Root-MUSIC formulation, the adaptation of ESPRIT to beamspace [40] requires similar restrictions placed upon the form of the beamforming vectors. Aside from this possihly over-restrictive requirement, two other problems associated with the beamspace Root-MUSIC algorithm are observed. First, the technique doesn't exploit the spatially-confined region of operation in the rooting stage of the algorithm, i.e., as the number of sensors comprising the array increases, the spatial extent of the beamforming sector decreases with constant N_b but, yet, the rooting is still defined over all of visible space. Second, the .approach involved the use of an N_b x N_b matrix transformation Q which can be highly ill-conditioned. For example, the condition number of Q for an $N = 138$ element array operated upon by a spatial Discrete Fourier Transform (DFT) beamformer was computed for a varying number of heams and plotted in Figure 4.1. In contrast, the other curve in the figure (Z transformation) corresponds to an alternative approach that is the key result of this chapter, having a. similar implementation for the MUSIC setting but fundamentally different to the approach of Chapter 2. Whereas the condition number associated with the Z-transformation is relatively constant a.t a value near 3 for all beamspace dimensions, the corresponding value for the Q-transformation is large for

even a small number of beams, e.g., for a heamformer comprised of $N_b = 8$ spatial DFT beams, the condition number is approximately $8 \cdot 10^9$.

The main purpose of this chapter is to develop a processing methodology that is based on the transformability of a beamspace noise eigenvector to an element-space counterpart as noted in passing in Appendix D, and also in [7]. In the intended application of beamspace processing, a spatial subband is probed so that the transformed beamspace noise eigenvectors are naturally bandlimited in a spatial sense. This banded characteristic allows for the application of classical multirate digital signal processing to isolate and spatially enlarge the spatial suhhand of interest. Note that this methodology departs from the classic implementation in that the pertinent information lies in the in-hand "signal" nulls instead of peaks in an in-hand spectrum. The aim is to preserve in-hand nulls instead of the more difficult task of preserving sinc patterns associated with the form of a signal dcfincd at the data level. A sensor level decimation scheme would suffer from the problem of preserving signal contributions away from the direction of interest whereas this scheme involves signal features having no components away from the characteristic null in the spectrum.

An important feature of this approach is that there are no restrictive requirements on the form of the beamforming vectors. The technique also results in a Root-MUSIC formulation where the rooting is clefinecl over a spatial window corresponding to the spatial subband probed by the beamforming vectors. Another major advantage is that the technique is computationally robust as the Z matrix transformation applied to the beamspace noise eigenvectors is well conclitioned. e.g., refer to Figure 4.1 where the condition number of a Z transformation is shown for the same array length and a suitable decimation procedure.

As the eigenvector transformation-clccimation proceclure is general in nature, the technique may be applied to any eigenstructure direction finding algorithm. We here consider the Root-MUSIC and ESPRIT [27] forinulations as these techniques are fairly representative of the eigenstructure class of angle estimators; application to other algorithms is straightforward.

The contents of this chapter are as follows. The development of the beamspace noise eigenvector transformation-decimation technique and its application to Root-MUSIC and ESPRIT ideology is contained in Section **4.2.** The theoretical performance of the MUSIC/ESPRIT formulations is developed, in terms of the estimation variance, in Section **4.3,** using tools from Chapter **3.** Finally, the theoretical performance expressions are validated in simulations and the optimality of the technique is observed through a comparison study with the stochastic Cramer-Rao bound in a variety of experiments in Section **4.4.**

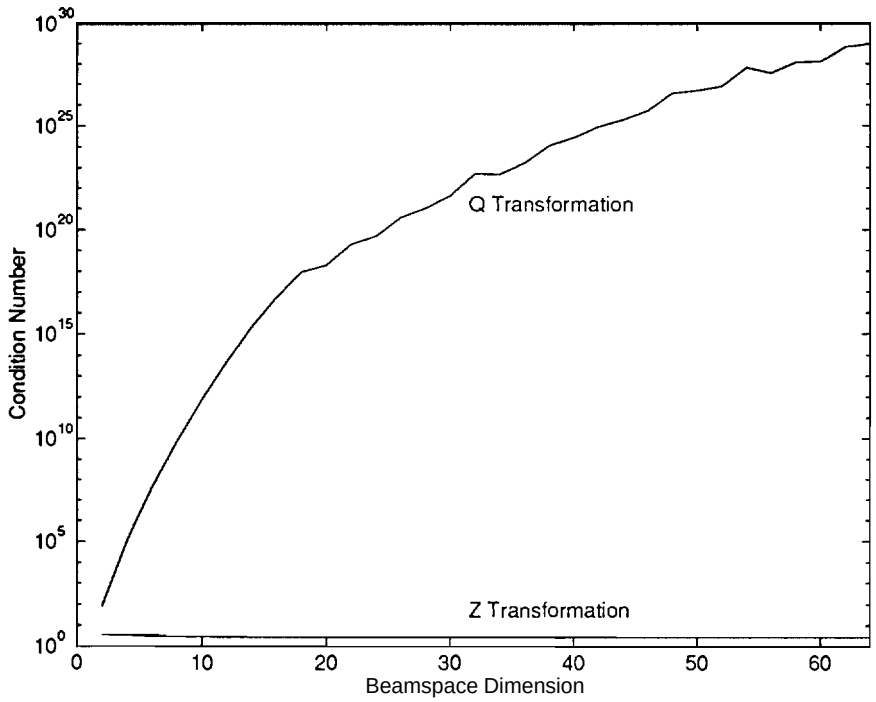

Figure 4.1 Condition number versus number of spatial DFT beams, N_b, for an $N = 128$ sensor array.

4.2 Development of DOA Estimators Featuring Multiriste Eigenvector Processing

In this section, the beamspace Root-MUSIC and TLS-ESPRIT DOA estimators incorporating multirate eigenvector processing are developed. In Section 4.2.1, the basis of the multirate processing technique of bearnspace noise eigenvectors is discussed, and an even more coinputationally efficient version is proposed in Section 4.2.2. Finally the techniques are applied to obtain Root-MUSIC and TLS-ESPRIT DOA estimation algorithms in Sections 4.2.3 and 4.2.4, respectively.

4.2.1 Multirate Noise Eigenvector Processing

A relation necessary for the development of the algorithms presented in this chapter is that a beamspace noise eigenvector can be transformed to a noise eigenvector in element space as noted in Appendix D. Defining

$$\mathbf{v}_i = \mathbf{W}\,\mathbf{e}_i, \qquad [4.1]$$

where e,, $i > K$, is a noise eigenvector of the ideal beamspace covariance, we see that $\mathbf{v}_i$ is indeed an eigenvector lying in the noise subspace of $\mathbf{R}_x$ as evidenced by

$$\mathbf{0} = \mathbf{B}^H\mathbf{e}_i = (\mathbf{W}^H\mathbf{A})^H\,\mathbf{e}_i = \mathbf{A}^H(\mathbf{W}\mathbf{e}_i) = \mathbf{A}^H\mathbf{v}_i \qquad i > K. \qquad [4.2]$$

Since A is an NxK matrix composed of the element space direction vectors which collectively span the signal subspace, v, = W e,, i=K+1,...,N_b, lies in the element space noise subspace. Also, given that e, is unit-length, $\mathbf{v}_i$ is unit-length as guaranteed by the orthonormality of the columns of W. Note, however, that no direct relationship exists between the beamspace and element-space signal subspace eigenvectors and that the $N_b - K$ transformed noise eigenvectors only partially describe the N-dimensional element-space noise subspace.

We now focus the development of the multirate eigenvector prescription to the MUSIC algorithm. To aid in the following development, it will be found useful to work with spatial locations denoted bv $\mu = \frac{2\pi d}{\lambda}\sin\theta$, where λ is the wavelength and d is the

sensor spacing. Thus, for example, the element space manifold vector with an end-sensor phase referencing is expressible as $\mathbf{a}_N(\mu) = \left[1, e^{j\mu}, \ldots, e^{j(N-1)\mu}\right]$. Employing the transformed noise eigenvectors which partially describe the element-space noise subspace, the associated MUSIC null spectrum [26] is appropriately described as

$$S_{MU}(\mu) = \sum_{k=\hat{K}+1}^{N_b} |\mathbf{a}_N^H(\mu)\,\mathbf{v}_k|^2. \quad -\pi \leq \mu \leq \pi \qquad [4.3]$$

For the known Vandermonde structure of the array manifold given, it is observed that each term in (4.3) simply has the form of a N-point spatial Discrete Time Fourier Transform (DTFT) of a transforined noise eigenvector,

$$V_k(\mu) = \mathbf{a}_N^H(\mu)\,\mathbf{v}_k = \sum_{n=1}^{N} v_k(n)\, e^{j\mu(n-1)} \quad -\pi \leq \mu \leq \pi \qquad [4.4]$$

where $v_k(n)$ represents the n'th entry in the vector $\mathbf{v}_k$

By selecting the set of beamforming vectors to interrogate some sector of space while attenuating signals that lie elsewhere, the spectrum of the transformed eigenvectors are naturally spatially band-limited. This can be viewed in the null spectrum of a single transformed noise eigenvector as shown in Figure 4.2. The parameters associated with the figure are as follows. N=128 half-wavelength spaced sensors were employed in conjunction with a standard spatial DFT beamformer consisting of eight consecutive beams centered in sine-space at $\sin\theta = 25/N$. For reference purposes, the spatial response of the N_b beams are included in Figure 3.3. There were two equi-powered signals located near mid-band at 10.4° and 11.5°; the locations are labelled on the figure. In addition, a high-strength signal was placed a.t a. distant location of $\sin\theta = 69/N$. A single beamspace noise eigenvector of the ideal covariance was employed to generate the results in the figure. Note that the presence of the other null within the band edges, indicative of a signal present at the corresponding angle, will "disappear" as the collective set of transformed noise eigenvectors are used for DOA estimation. Although in-band nulls are of interest, the main point of the figure is that the spectrum exhibits an elevated response in the spatial region where the beams are directed. Also, note that the spatial spectrum is not elevated in the region neighboring the distant signal.

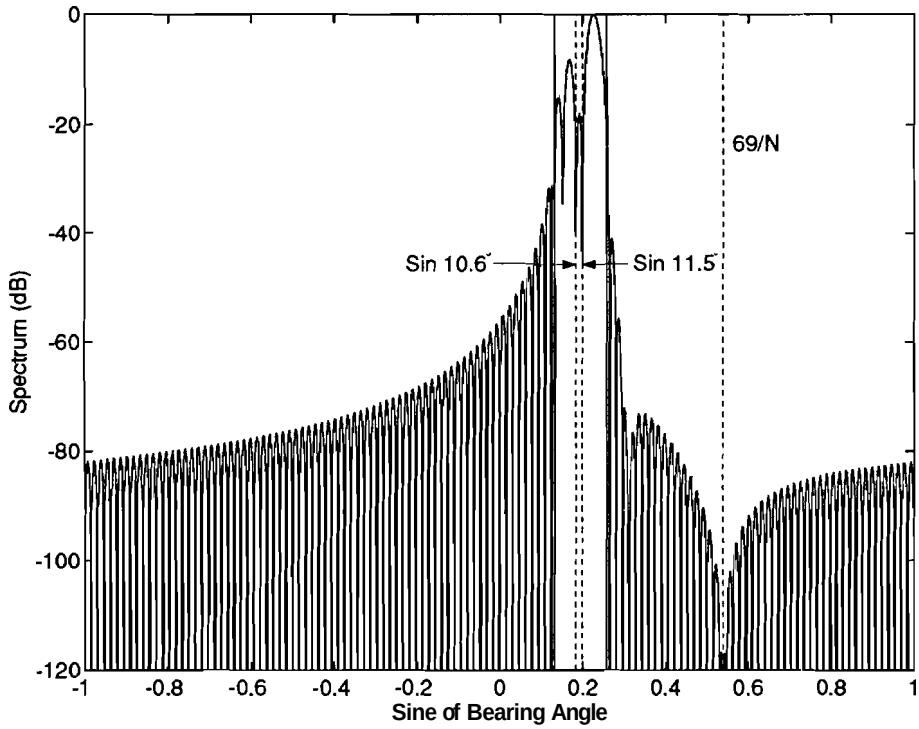

Figure *4.2* Spectrum of a transformed noise eigenvector derived from the decomposition of the ideal beamspace covariance associated with an $N = 128$ sensor ULA operated on by a $N_b = 8$ dimension spatial DFT beamformer centered in space at $25/N$. Two in-band signals were located at $10.6°$ and $11.5'$ and one out-of-band source was located at $\sin\theta = 69/N$.

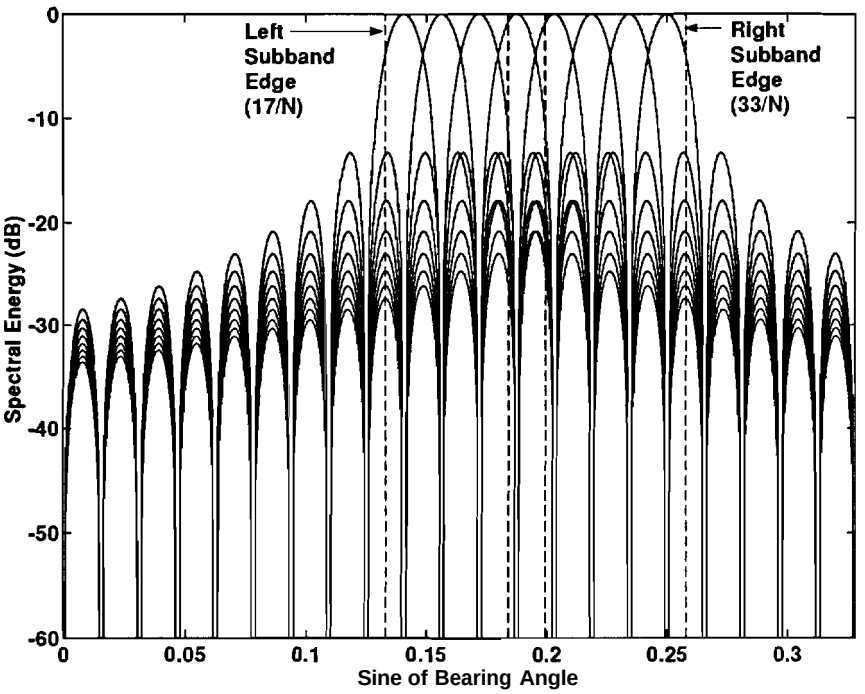

Figure **4.3** Angular responses of $N_b = 8$ successive DFT beamforming vectors. Beamforming sector centered at at $\sin\theta = 25/N$.

The banded nature of the null spectra suggests that a multiirate procedure is in order where the spatial band surrounding $\sin\theta = 25/N$ is spatially base-banded and more sparsely sampled. In other words, one can extract a spatial region of interest from the spectrum and represent the information with :€ewer parameters. Consider decimation by an integer factor D that is less than or equal to the maximum allowable value. For the example employing N_b spatial DFT beams, the maximum decimation factor is $D_{max} = N/N_b$.[1] The sequence associated with the decimated k'th eigenvector is

$$v_D^{(k)}(i+1) = v_k(Di+1) \qquad i = 0, 1, ..., N/D - 1.$$

From classical multirate digital signal processing theory, the spatial spectrum associated with the k'th decimated eigenvector is

$$V_D^{(k)}(\mu) = \sum_{\ell=0}^{D-1} V_k(\frac{u - 2\pi\ell}{D}) \qquad [4.5]$$

where we recognize the periodicity in the variable μ, i.e., $V(\mu + 2\pi n) = V(\mu)$ for integer n. By assuming that the spectrum has negligible amplitude outside of the region of interest, i.e., $V_k(\mu)$ м 0, $|\mu| > \pi/D$, only the $\ell = 0$ term contributes to the sum leading to $V_D^{(k)}(\mu) \approx V_k(\mu/D)$, $-\pi < \mu <$ a.

In the usual application of multirate processing, one must be concerned with the aliasing of signals into the band of interest; here we must insure that aliasing does not result in the "filling in" of signal nulls within the band of interest. Note that signals that lie outside of the spatial band of interest do not affect the spectrum, i.e., in fact, the reduced amplitude in the neighboring region as seen in Figure 4.2 will result in a smaller aliasing contribution. However, the presence of the large distant signals may increase the perceived dimension of the signal subspace (k)in the decomposition of the sample covariance matrix so that their presence is undesired.

If the front-end beamformers have high sidelobes, a spatial filter prior to decimation might be necessary to insure that the null spectrum is not distorted due to

[1]Although the terminology "sampling rate alteration" applies for non-integer D_{max}, we will still refer to the rate conversion operation as "decimation."

aliasing, i.e., the "signal" nulls are not shifted appreciably. The filter should incorporate a sufficient stopband attenuation to limit the degree of aliasing. In contrast, a larger stopband attenuation requires a larger filter length. As the ultimate intention of multirate processing is to reduce the dimension of the transformed/decimated noise eigenvectors, a shorter-length filter is desired. Note that the length of the noise eigenvectors after decimation is $\lceil \frac{N+L-1}{D} \rceil$, where L is the filter length, D is the decimation factor which is less than or equal to $D_{max} = N/N_b$ and $\lceil x \rceil$ refers to the smallest integer greater than or equal to x.

As there is no need for a linear phase requirement, an IIR filter may be employed. The absence of a linear phase requirement in IIR designs should result in a smaller filter length, L, where L is taken as some appropriate effective length of the associated impulse response. Note, however, that the classic IIR low-pass designs such as the Butterworth, Chebyshev, Elliptic, etc., filters incorporate poles that are very near the unit circle so that the associated impulse responses are relatively long. It was determined that these classic designs offer little or no advantages in terms of lengths versus band specifications as compared to such FIR techniques as the Hamming, Hanning, or Blackman windowed low-pass filters (LPF). Also note that a high degree of passband ripple may not pose a significant problem as there is a procedure, to be discussed shortly, for the removal of the ripple that follows the decimation operation.

A major factor in determining an appropriate filter length is the width of the transition band. The simplest means of increasing the width of the transition band, and, hence, shortening the filter length, is to decimate by a factor that is less than the maximum allowable limit D_{max}. This would increase the distance between the edges of the beamforming sector, the region encompassed by the mainlobes of the N_b beams, and the spatial location $\mu = \pi/D$, the location that is scaled-up to the spectral edge ($\mu = \pi$) after decimation. Thus, by designing a filter with a transition band that lies within the spatial zone that is exterior to the passband of the beamforming sector, the aliasing effects are essentially confined to this region which we disregard. Another approach is to simply allow the passband edge to extend within the beamforming

sector as it has been shown in a preceding chapter that beamspace DOA architectures tend to perform rather poorly in terms of estimation bias/variance at the edges of the beamforming sector. This effect is attributable to the reduction in the total signal power, $\mathbf{b}^H(\mu)\mathbf{b}(\mu)$, as the signal nears the edge of the spatial subband. Thus the transition band of the filter may be designed to encompass perhaps 25-50% of the total beamforming sector in which case one would have to allow an .associated overlap amongst subbands probed in succession or in parallel. Due to the characteristic shape of the noise eigenvector spectra, the aliasing effects primarily originate just outside of the pre-decimation subband defined over $\mu \in [-\pi/D, \pi/D]$. Thus specifying that the transition band of the filter be centered at π/D, the aliasing will be primarily present in the edges of the beamforming sector which are disregarded. Returning to the $N_b = 8$ beam example, an N = 128 element Hamming-windowed LPF with a transition band defined over the region $\mu \in [6.5\pi/N, 9.5\pi/N]$, wlhere $\mu = 8\pi/N$ is both the edge of the beamforming sector and the edge of the pre-decimation subband, proved to be a reasonable design. A sketch of the passband associiated with this low pass filter design can be found in Figure 4.4. The filter response is shown along with the MUSIC null spectrum associated with the use of all spatially basebanded transformed noise eigenvectors to show another feature of this filter selection: the interlacing of the nulls which results in a dramatical reduction in the effects of aliasing. As the out-of-band nulls of the basebanded beamspace MUSIC null spectrum are at known data-independent spatial positions corresponding to the common null locations of the beam set of Figure **4.3,** the filter parameters can be selected to produce the null interlacing effect as seen in Figure 4.4. Also note that the use of all beamspace noise eigenvectors in a MUSIC formulation resulted in the removal of the non-signal in-band spatial null that was present in the single transformed noise eigenvector spectrum of Figure 4.2. The resulting filtered eigenvector MUSIC null spectrum is shown in Figure 4.5 and the corresponding decimated MUSIC null spectrum is included in Figure 4.6.

With the modulation (spatial basebanding), filtering, and decimation operations notated by $\mathbf{M}$, $\mathcal{F}$, and $\mathcal{D}$, respectively, the decimated/transformed noise eigenvectors

are then $\boldsymbol{\nu}_i = \mathcal{D}\mathcal{F}\mathrm{M}\{\mathrm{W}\mathbf{e}_i\}$, $i > \mathrm{K}$. As decimation, filtering, and modulation are linear operations, these may be performed a priori on the N_b columns of W as evidenced in

$$\boldsymbol{\nu}_i = \mathcal{D}\mathcal{F}\mathcal{M}\left\{\sum_{k=1}^{N_b} \mathbf{w}_k e_i(k)\right\} = \sum_{k=1}^{N_b} [\mathcal{D}\mathcal{F}\mathcal{M}\{\mathbf{w}_k\}]\, e_i(k) = \sum_{\mathrm{k=1}}^{N_b} \mathbf{z}_k e_i(k) = \mathbf{Z}\mathbf{e}_i, \tag{4.6}$$

where

$$\mathbf{Z} = \left[\mathbf{z}_1 \vdots \right. \qquad\qquad = DFM\{\mathrm{W}). \tag{4.7}$$

Hence, the matrix Z of dimension N_Z x N_b, where $N_Z = \lceil \frac{N+L-1}{D} \rceil$, may be computed a priori and applied to the beamspace noise eigenvectors $\mathbf{e}_i$, $i = K + 1, \ldots, N_b$. In the more general case of sampling rate conversion where the desired "decimation" factor is not an integer but can be expressed as a ratio of two integers $\mathrm{D} = M_D/M_I$, the corresponding matrix Z is computed as

$$\mathbf{Z} = \mathcal{D}_{M_D}\mathcal{F}\mathcal{I}_{M_I}\mathcal{M}\{\mathbf{W}\}, \tag{4.8}$$

where $\mathcal{D}_{M_D}$ represents a decimation operation by a factor of M_D and $\mathcal{I}_{M_I}$ refers to an interpolation operation by a factor of M_I. Note that the filter frequency design specifications are appropriately modified to reflect the positioning following the interpolator. Also, due to the modulation operation, the matrix Z can be employed for a common beam set steered to any sector of space. In this mode of operation, the estimates of the signal μ locations provided by the algorithm are relative to the center of the beamforming sector.

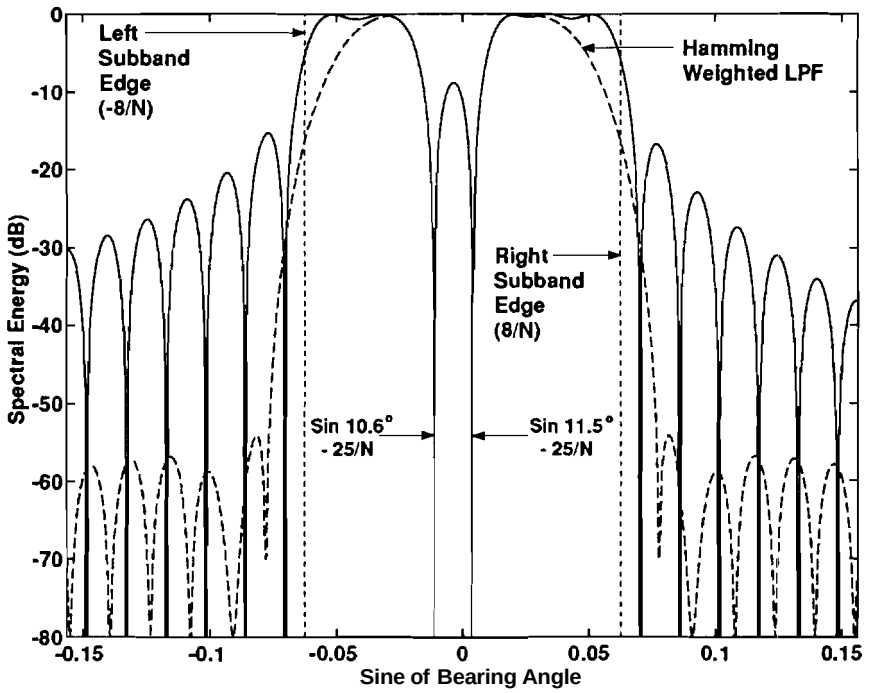

Figure 4.4 MUSIC null spectrum after modulation to baseband and filter response associated with the L = 128 length Hamming-weighted LPF.

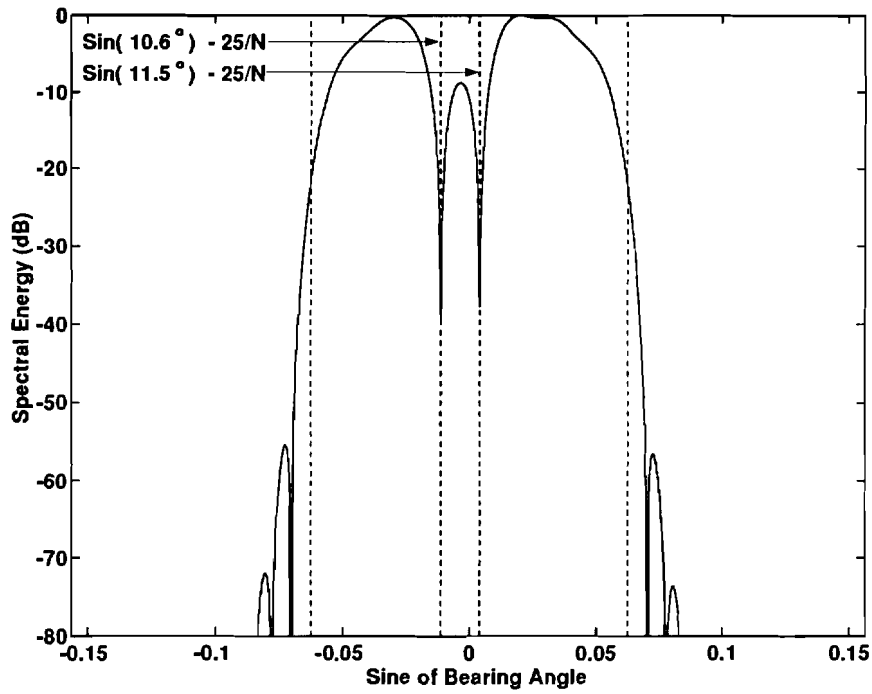

Figure 4.5 MUSIC null spectrum after Hamming-window based bandpass filtering.

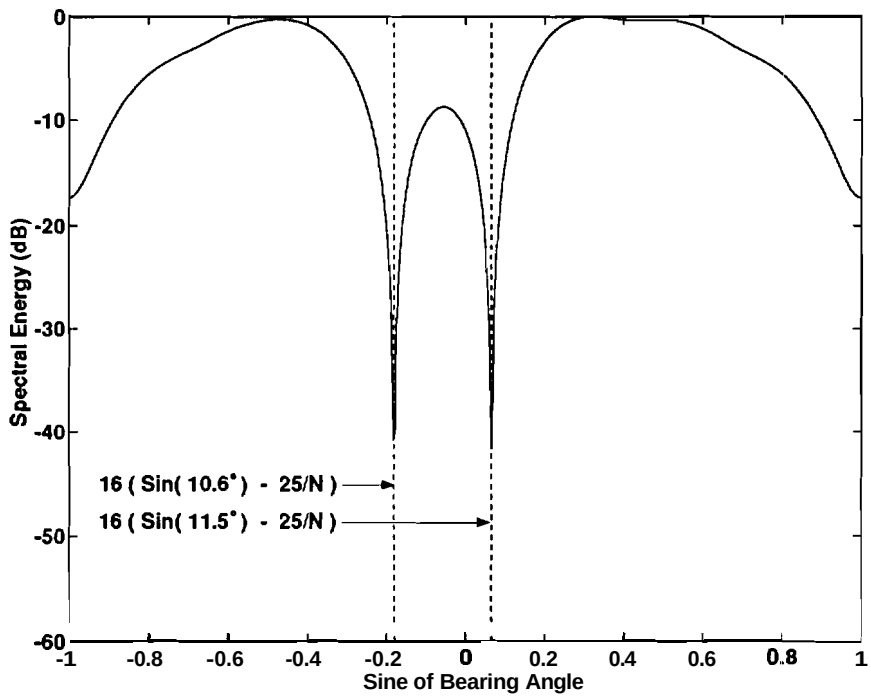

Figure 4.6 MUSIC null spectrum after decimation by factor of $128/8 = 16$.

4.2.2 Incorporation of Filter Deconvolution

As the inclusion of a properly designed filter will result in negligible aliasing effects, it is possible to reduce the row-dimension of the matrix Z, and hence the order of the polynomial that ultimately needs to be rooted. This computational advantage is accomplished through the deconvolution of the decimated filter sequence from each column of $\mathbf{Z}$ as substantiated in this section.

Denoting the spatial DTFT of the i'th transformed and decimated beamspace noise eigenvector as $V_{DFM}^{(i)}(\mu)$, we find, as similar to the form in equation (4.4),

$$V_{DFM}^{(i)}(\mu) = \sum_{k=1}^{N_Z} \nu_i(k)\, e^{j\mu(k-1)}. \qquad [4.9]$$

The above form offers an alternative view of the decimation procedure where the spatial spectrum $V_{DFM}^{(i)}(\mu)$ is expressed in terms of the DTFT's of the filter and the i'th modulated-transformed eigenvector. Defining the DTFT's

$$V_M^{(i)}(\mu) = \sum_{k=1}^{N} v_M^{(i)}(k)\, e^{j\mu(k-1)} \qquad [4.10]$$

$$H(\mu) = \sum_{k=1}^{L} h(k)\, e^{j\mu(k-1)} \qquad [4.11]$$

where $\mathbf{v}_M^{(i)} = \mathrm{M}\{\mathbf{We}_i\} = \mathrm{M}\{\boldsymbol{\nu}_i\}$ and $\boldsymbol{h}$ is an Lx1 vector composed of the entries of the filter impulse response. One can express $V_{DFM}^{(i)}(\mu)$ as

$$V_{DFM}^{(i)}(\mu) = \frac{1}{D} \sum_{\ell=0}^{D-1} H\left(\frac{\mu - 2\pi\ell}{D}\right) V_M^{(i)}\left(\frac{\mu - 2\pi\ell}{D}\right). \qquad [4.12]$$

Notice that the form of (4.12) implies an integer-valued decimation factor D. Modifications for the more general cases where the sampling rate alteration is expressible as a non-reducible ratio of two integers, $\mathrm{D} = M_D/M_I$, are readily incorporated into the procedure and will be addressed later in this section.

Assuming that aliasing effects are negligible, the $\ell = 0$ term (region surrounding baseband) dominates so that the following approximations are equally valid

$$\begin{aligned} V_{DFM}^{(i)}(\mu) &\approx \frac{1}{D} H\left(\frac{\mu}{D}\right) V_M^{(i)}\left(\frac{\mu}{D}\right) \\ &\approx \frac{1}{D}\left[\sum_{\ell=0}^{D-1} H\left(\frac{\mu - 2\pi\ell}{D}\right)\right] V_M^{(i)}\left(\frac{\mu}{D}\right). \end{aligned} \qquad [4.13]$$

Observe that the bracketted term in the latter approximation is simply the DTFT of the decimated impulse response of the filter sequence, $h_D(\mathrm{k}) = h(D\,k)$. Acceptance of the above approximations suggests that one is capable of removing the effects of the filter from the decimated null spectrum. Thus, we may acquire the pertinent (signal) information associated with the eigenvector spectrum by viewing an alternate spectrum, denoted $V^{(i)}_{G^{-1}DFM}(\mu)$, given as

$$V^{(i)}_{G^{-1}DFM}(\mu) \approx \frac{V^{(i)}_{DFM}(\mu)}{\sum_{\ell=0}^{D-1} H\left(\frac{\mu-2\pi\ell}{D}\right)}. \qquad [4.14]$$

Equivalently, the spectral division can be accomplished by deconvolving the decimated filter sequence out of the i'th decimated eigenvector, $\mathbf{Ze}_i$. As the deconvolution operation is also linear, one can simply deconvolve the decimated filter impulse response out from each column of $\mathbf{Z}$ to form a matrix $\mathbf{Z}'$. Denote the deconvolution operator as $\mathcal{G}^{-1}$ so that $\mathbf{Z}' = \mathcal{G}^{-1}\mathcal{D}\mathcal{F}M\ \{\mathrm{W}\}$. Recall that $\mathbf{Z}$ is an N_ZxN_b matrix where $N_Z = \lceil \frac{N+L-1}{D} \rceil$. Assuming that the deconvolution is exact, the size of $\mathbf{Z}'$ is $N_{Z'}$xN_b, where $N_{Z'} = \lceil \frac{N+L-1}{D} \rceil - \lceil \frac{L}{D} \rceil + 1$. As the imperfect filtering introduces a small degree of aliasing, the deconvolution is not exact. Therefore, there exists a remainder term that must be considered such that the resultant process may not be causal. Numerically it is better to carry out the deconvolution by way of spectral division. In this case, the DTFT of a given column of $\mathbf{Z}$ is divided, point-wise, by the DTFT of the decimated filter sequence so that the inverse DTFT of the result provides the associated deconvolved column of $\mathbf{Z}'$. Depending upon the values of N and N_b, simulations have shown that possibly one or two extra points on either side of the $N_{Z'}$ points should be appended to each column of $\mathbf{Z}'$. A suitable criterion employed in simulation studies is that all points whose magnitudes greater than 5-10% of the maximum value should be included in $\mathbf{Z}'$.

Returning to the example cited earlier where the beamforming matrix corresponding to an N=128 element ULA with d = $\lambda/2$ and N_b=8 beams is operated on by an L = 128 length Hamming-windowed LPF and then maximally decimated, the dimensionality of the $\mathbf{Z}$ matrix is N_ZxN_b, $N_Z = \lceil \frac{N+L-1}{D} \rceil = 16$. Assuming perfect

deconvolution, the associated value of $N_{Z'}$ is 9. Adopting the 10% criteria in the selection of the row-dimension of $\mathbf{Z}'$, it was found that one extra value per column was needed. By way of spectral division employing the FFT/IFFT algorithms, the extra values were the last samples of the IFFT, which were wrapped-around to form the first row of $\mathbf{Z}'$.

In the case of non-integer decimation where the factor D is expressible as a ratio of two integers as $\mathrm{D} = M_D/M_I$, a similar procedure can be implemented. Referring to Equation (4.12)) the spectrum $V_M^{(i)}(\cdot)$ is replaced by the pre-filtered spectrum $V_{IM}^{(i)}(\cdot)$ defined by the DTFT of the i'th transformed, modulated, and interpolated (M_I) noise eigenvector. The applicable decimation factor in (4.12) is then M_D. Note that the filter frequency-band specifications are selected to reflect the presence of the interpolation stage. As a result, for the matrix $\mathbf{Z}$ defined by $\mathbf{Z} = \mathcal{D}_{M_D}\mathcal{F}\mathcal{I}_{M_I}\mathrm{M}\{\mathrm{W}\}$, the N_b columns of the matrix $\mathbf{Z}'$ are found by deconvolving the decimated filter impulse response (decimated by the factor M_D) out from the corresponding columns of $\mathbf{Z}$.

The reduced row dimension of $\mathbf{Z}'$ relative to that of $\mathbf{Z}$ ultimately results in a computational savings for DOA estimation at the expense of a slight performance degradation as to be shown in a subsequent section. The application of multirate noise eigenvector processing to the MUSIC algorithm is analyzed in Section 4.2.3 while an application to the TLS-ESPRIT algorithm is considered in Section 4.2.4. The two algorithms are considered as representative of the class of eigenstructure DOA estimators. Extensions to other DOA estimation algorithms are easily accomplished.

4.2.3 Root-MUSIC Incorporating Multirate Eigenvector Processing

The multirate eigenvector technique is simply incorporated into the MUSIC algorithm of Schmidt [26]. As the transformed beamspace eigenvectors, We;, $i > K$, are orthogonal to the element-space manifold vectors corresponding to a signal arrival angle, $\mathbf{a}_N(\mu_k)$, k $\leq K$, the following condition holds

$$\mathbf{Z}\mathbf{e}_i = \mathcal{D}\mathcal{F}\mathcal{M}\{\mathbf{W}\mathbf{e}_i\} \perp \mathcal{D}\mathcal{F}\mathcal{M}\{\mathbf{a}_N(\mu_k)\} \quad i > K,\ k \leq K. \qquad [4.15]$$

Assuming that the filter is ideal with a cutoff at the spatial location $\mu = \pi/D$, it is easily observed that the in-band signal nulls are preserved through the decimation operation such that

$$(\mathcal{DFM}\{\mathbf{We}_i\})^H(\mathcal{DFM}\{\mathbf{a}_N(\mu_k)\}) = (\mathbf{Ze}_i)^H\mathbf{a}_{N_Z}(D\mu_k) = 0 \quad i > K,\ k \leq K. \tag{4.16}$$

If the filter is properly designed to limit aliasing yet pass all in-bandl signals, equation *(4.16)* is a reasonably accurate approximation. Thus a suitable MUSIC null spectrum can be defined as

$$\mathcal{N}_{MU}(\mu) = \sum_{k=K+1}^{N_b} \left|\mathbf{a}_{N_Z}^H(D\mu)\ (\mathbf{Z}\hat{\mathbf{e}}_k)\right|^2 = \mathbf{a}_{N_Z}^H(D\mu)\mathbf{Z}\hat{\mathbf{E}}_n\hat{\mathbf{E}}_n^H\mathbf{Z}^H\mathbf{a}_{N_Z}(D\mu), \tag{4.17}$$

where the estimated noise eigenvectors define

$$\hat{\mathbf{E}}_n = \left[\hat{\mathbf{e}}_{K+1} \vdots \hat{\mathbf{e}}_{K+2} \vdots \ldots \vdots \hat{\mathbf{e}}_{N_b}\right] \tag{4.18}$$

and $\mathbf{a}_{N_Z}(Dp)$ is an N_Z-dimensional element space manifold vector. The MUSIC DOA estimates are estimated as the peaks of the spectrum, $\mathcal{S}_{MU}(\mu) = 1/\mathcal{N}_{MU}(\mu)$, i.e.,

$$\hat{\mu}_k = \max_{\mu} \mathcal{S}_{MU}(\mu) = \min_{\mu} \mathcal{N}_{MU}(\mu) \quad i \leq K, \tag{4.19}$$

where the true angles, $\hat{\theta}_k$ are computed from $\hat{\mu}_k$ via $\hat{\theta}_k = \sin^{-1}(\hat{\mu}_k\lambda/2\pi dD)$, $k \leq K$.

Due to the Vandermonde structure of $\mathbf{a}_{N_Z}(D\mu)$, the spectral search for the estimation of the DOA angles as suggested in equation *(4.19)* can be converted to the rooting of polynomial a la Root-MUSIC. The technique is included in the summary of the algorithm included below. Note that the Root-MUSIC algorithm employing the deconvolved version of Z, $\mathbf{Z}' = \mathcal{G}^{-1}\mathcal{DFM}\{\mathbf{W}\}$, is defined in a similar way where $\mathbf{Z}'$ and $N_{Z'}$ are substituted for $\mathbf{Z}$ and N_Z, respectively.

Summary of Root-MUSIC Application Algorithm

1. form the N_Z x N_b decimated-filtered-modulated beamforming matrix a-priori: $\mathbf{Z} = \mathcal{D}\mathcal{F}\mathcal{M}\{\mathrm{W}\}$

2. EVD of $\hat{\mathbf{R}}_y = \sum_{m=1}^{M} \mathrm{y(m)y^H(m)/M}$, where $\mathbf{y}(m) = \mathrm{W^H x(m)}$, m=1,...,M.

3. estimate number of sources, K, and place N_b-$\hat{K}$ "smallest" eigenvectors as columns of $\mathbf{E}_n$

4. with $p_k = \sum_{i=0}^{k} \mathbf{P}(N_Z - k + \mathrm{i}, \mathrm{i} + 1)$, k=0,1,...,$N_Z$-1, where $\mathrm{P} = \mathrm{Z}\,\mathbf{E}_n\mathbf{E}_n^H\,\mathrm{Z^H}$, construct

$$p(z) = p_0 + p_1 z + \ldots + p_{N_Z-1} z^{N_Z-1} + \ldots + p_1^* z^{2N_Z-3} + p_0^* z^{2N_Z-2}$$

5. root $p(z)$, select K signal roots: $\hat{\theta}_k = sin^{-1}(angle\{\hat{z}_k\}\lambda/2\pi dD)$ k = 1, 2, ..., K

Comparing the above prescription to the approach delineated in Chapter 2, the $N_Z \times N_b$ transformation $\mathbf{Z}$ replaces an N_b x N_b matrix Q. The only disadvantage is a slight increase in computation as the polynomial to be rooted is slightly higher in order. However, the dimension N_Z can be selected to be only slightly larger than N_b if the deconvolution operation, $\mathcal{G}^{-1}$, is incorporated. The advantages of using the $\mathbf{Z}$ approach over that of $\boldsymbol{Q}$ are robustness to the computational accuracy of the rooting algorithm and removal of the over-restrictive structural requirements on the type of beamformer employed.

The accuracy of the $\mathbf{Z}$ and Z' transformations was assessed by observing the signal root locations when the ideal sample covariance is decomposed for use in the Root-MUSIC algorithm. The parameters of the array, beamformer, and decimator are those presented earlier in the example of Figures 4.2-4.6. The resulting root locations are shown in Figure 4.7 and the actual signal root locations for the two transformation types are included in the figure. The extremely accurate signal-root placement associated with the use of $\mathbf{Z}$ suggests that the orthogonality criterion $\mathbf{Z}\mathbf{e}_i \perp \mathbf{a}_{N_Z}(D\mu_k)$,

$i > K$, k $\leq K$, is valid. Also note that the effects of the filter can be removed via deconvolution without appreciably affecting the performance of the algorithm as indicated by the locations of the roots associated with the use of $\mathbf{Z}'$.

To visualize the removal of the passband ripple as induced by the filter when deconvolution is employed, an example involving an FIR filter designed via the Parks-McClellan [41] algorithm with a "large" passband ripple was analyzed. In addition, to verify the validity of the general multirate procedure, an N = 90 sensor array with $N_b = 6$ beams was used in a scenario involving decimation by a non-integer fraction D = 11.25 = 45/4 which is less than the maximum allowable value of $D_{max} = N/N_b = 15$. The filter was designed to be of length 270 – note that the filtering is accomplished at the output of the interpolator stage ($D_I = 4$). The sub-maximal decimation factor allowed for a wide filter transition band, $(1/4)(5/N)\pi \leq \mu \leq (1/4)(11/N)\pi$, and, combined with a frequency band weighting favoring a high stopband attenuation, resulted in a 67 dB stopband attenuation with a 1.8 dB passband ripple. A plot of the spatial responses of the filter (dashed line) and interpolated beamformers (solid line) is presented in Figure 4.8. The beamforming weight vectors were interpolated, by a factor of 4, to allow a visual comparison with the filter response curve.

Figure 4.9 shows the response of the $N_b = 6$ transformed, filtered, and decimated beamforming vectors along with the spectrum of the decimated filter. Note that the decimated filter magnitude spectrum (dashed curve) appears to follow the shape of the beam peaks.

The spectral MUSIC algorithm was employed with an ideal noise-only beamspace covariance matrix to compare the effects of using **Z** or **Z'.** As this situation is effected using $\mathbf{E}_n\mathbf{E}_n^H = \mathbf{I}$, the MUSIC spectrum characterizes the imparted distortion to a white noise input spectrum by the inclusion of filtering or filtering with deconvolution. Figure 4.10 shows the MUSIC spatial spectra for a noise-only input employing the **Z** and $\mathbf{Z}'$ techniques. The results show that the deconvolution operation was effective in removing the filter shape from the spectrum leaving only a sl'ight ripple that is

representative of the finite spatial window associated with the beamformer. Again, the deviation at the edges of the spatial spectrum from the anticipated constant level is expected: the beamforming sector does not extend to the edge of the band $\mu = \pi/D$.

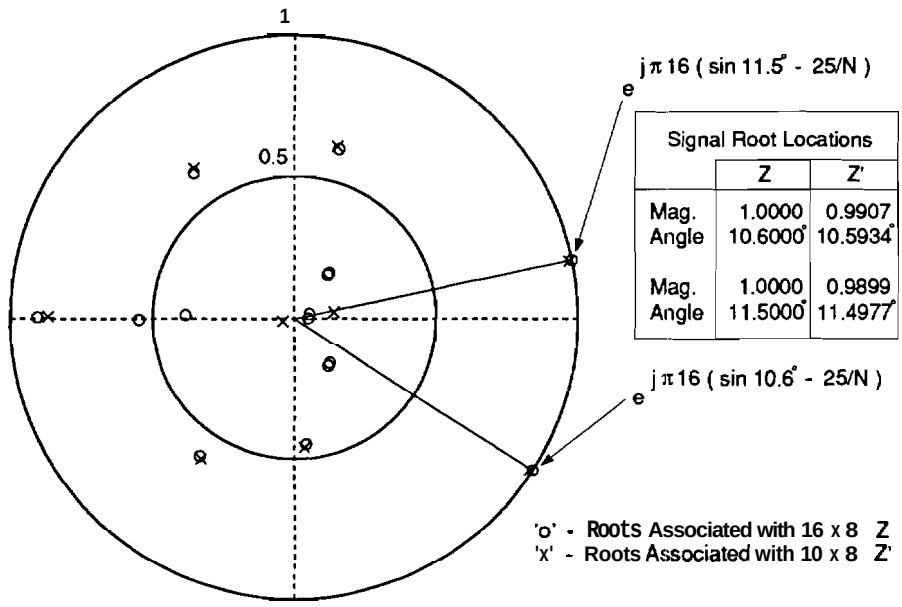

Figure 4.7 Roots using transformed-modulated-filtered-decimated noise eigenvectors for both the Z and (deconvolved) Z' transformations,. Quiescent root locations computed with the use of the ideal beamspace covariance. True signal locations: 10.6' and 11.5'.

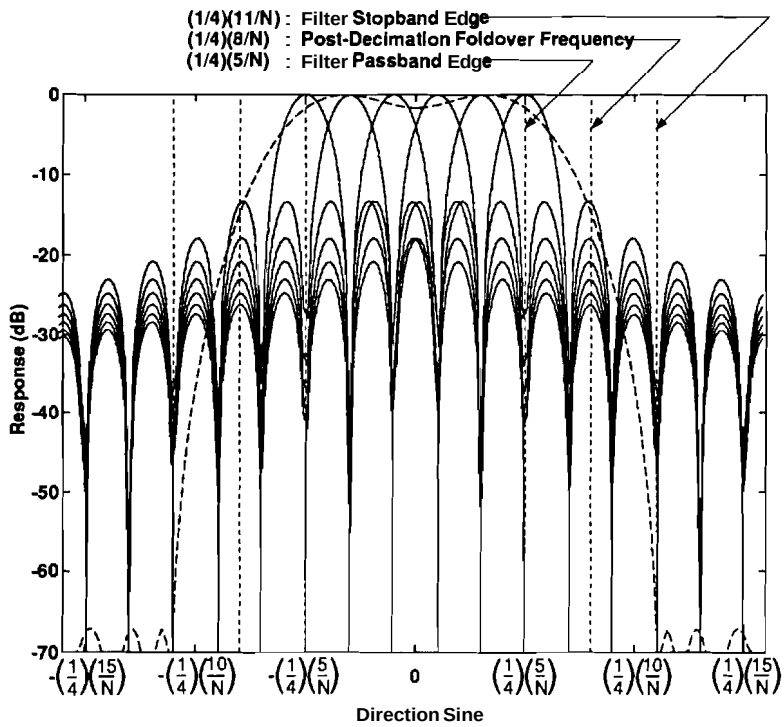

Figure ***4.8*** Spatial responses of an L = 270 length equi-ripple filter and interpolated $N_b = 6$ beam set derived from an $N = 90$ sensor array. The spatial foldover frequency for the sub-maximal decimation architecture is located at $\sin\theta = (1/4)(8/N)$.

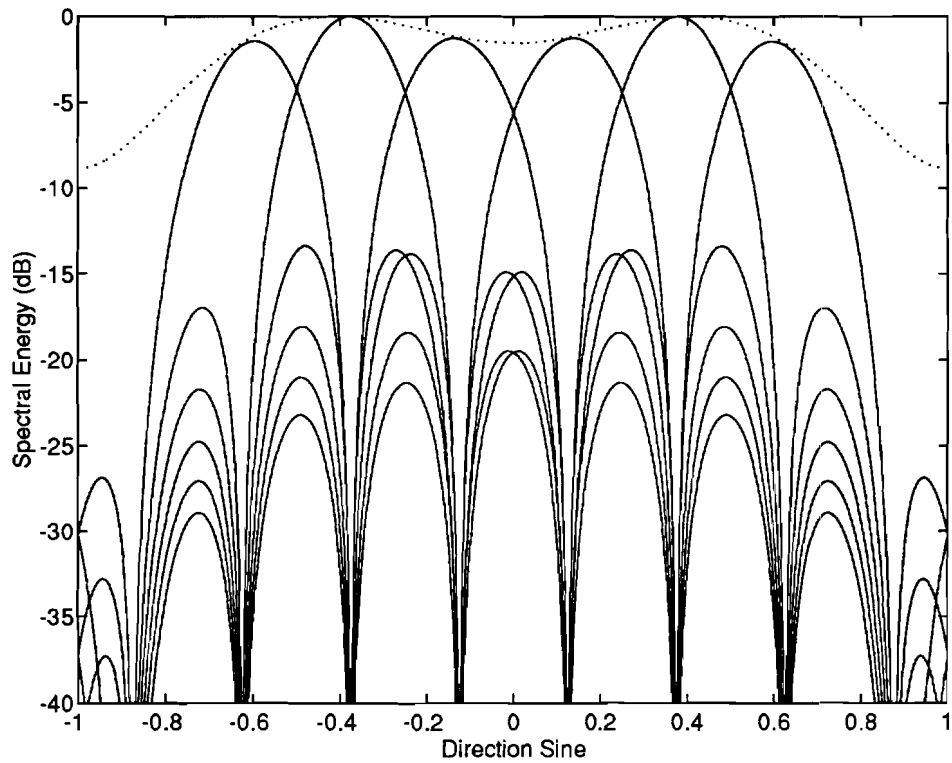

Figure 4.9 Decimated filter/beamformer spectra associated with the filter/beam set of Figure 4.8.

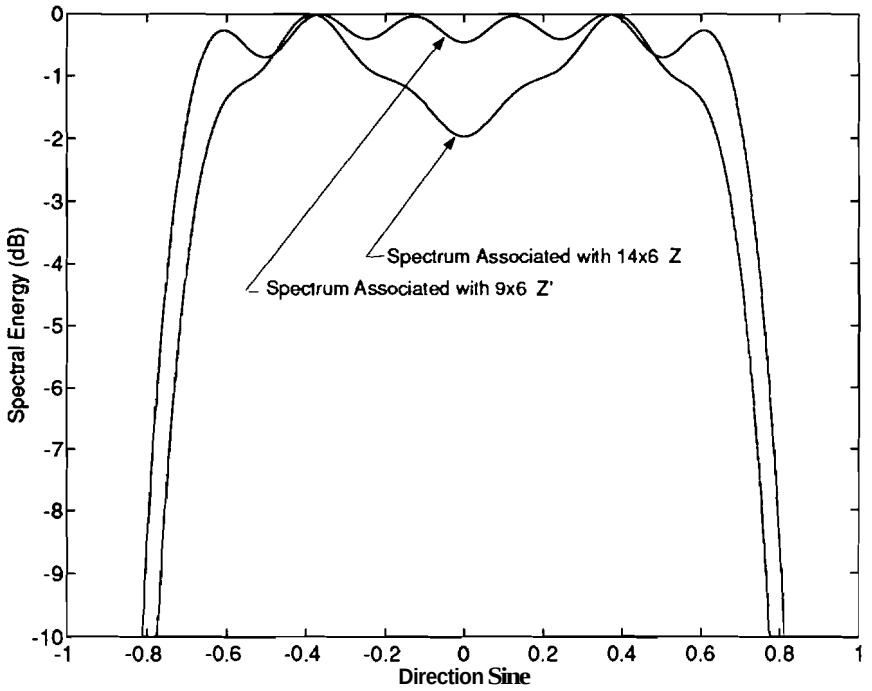

Figure 4.10 MUSIC spectra associated with ideal white-noise beamspace covariance with the use of the Z and $\mathbf{Z}'$ transformations derived from the beamforming/filter architecture of Figure 4.8.

4.2.4 TLS-ESPRIT Incorporating Multirate Eigenvector Processing

As with the beamspace Root-MUSIC algorithm of Chapter 2, the beamspace ESPRIT formulation of Xu, et.al. [40] requires a rather restrictive specification on the form of the beamforming vectors. As we will see in this section, the commonplace uniformly-spaced line array of sensors allows an ESPRIT application of the transformed-decimated beamspace eigenvector approach of Section 4.2.2.

Given the N_b-K transformed and decimated noise eigenvectors, define an $N_Z \times ([N_Z - N_b] + \mathrm{K})$ matrix $\mathbf{E}_{Z_s}$ whose columns form a subspace that; is orthogonal to that formed from the vectors $\mathbf{Ze}_i$, $i > K$. An efficient means of computing $\mathbf{E}_{Z_s}$ is by way of a QR decomposition of ZE,. Note that the standard ESPRIT approach employs a matrix whose K columns span an estimate of the signal subspace; here we have a set of vectors in $\mathbf{E}_{Z_s}$ whose span encompasses the (decimated element-space) subspace, since $N_Z > N_b$. Assuming aliasing effects to be negligible, we have

$$\text{span}\{\mathbf{a}_{N_Z}(D\mu_k),\ \mathrm{k} = 1, \ldots, K\} \subset \text{range}\{\mathbf{E}_{Z_s}\}. \qquad [4.20]$$

Although beamspace signal eigenvectors are not transformable to their element space counterparts, there is an alternative means of finding a set of vectors that are related to the beamspace signal eigenvectors and also span the orthogonal subspace of span $\{\mathbf{Ze}_i, i = K + 1, \ldots, N_b\}$. The N_Z x N_b matrix transformation Z has full column rank so that the orthogonal subspace of span $\{\mathbf{Ze}_i, i = K + 1, \ldots, N_b\}$ is expressible as a collection of $N_Z - N_b$ spanning vectors which are orthogonal to the columns of Z as well as to the K vectors lying in the column space of Z. A permissable set of vectors which span the orthogonal subspace are the columns of

$$\mathbf{E}_{Z_s} = \left\lfloor \mathbf{Z}(\mathbf{Z}^H\mathbf{Z})^{-1}\mathbf{e}_1 \vdots \ldots \vdots \mathbf{Z}(\mathbf{Z}^H\mathbf{Z})^{-1}\mathbf{e}_K \vdots \boldsymbol{\beta}_1 \vdots \ldots \vdots \boldsymbol{\beta}_{N_Z - N_b} \right\rfloor, \qquad [4.21]$$

where $\{\boldsymbol{\beta}_1, \ldots, \boldsymbol{\beta}_{N_Z - N_b}\}$ is a set of vectors that span the subspace orthogonal to the column space of Z. Notice that the set of vectors in (4.21) are not orthogonal but still are adequate for use in ESPRIT. In addition to the computational savings in avoiding a QR-decomposition, construction of $\mathbf{E}_{Z_s}$ according to (4.21) also allows one to derive

the theoretical angle estimation performance using available asymptotic expressions for the beamspace eigenvector statistics as we shall see in Section **4.3.**

We will return to the "over-specification" issue of the decimated signal subspace in this section and show that judicious beamforming and filter design allows for proper operation of a suitably defined ESPRIT algorithm. Assuming that the beamforming and filtering operations produce little aliasing effects so that equation ***(4.20)*** is a reasonably accurate approximation, we may define a TLS-ESPRIT procedure to estimate the directions of the K signal arrivals based upon the Vandermon.de form of $\mathbf{a}_{N_Z}(\cdot)$. The algorithm is summarized as follows.

Summary of TLS-ESPRIT Application Algorithm

1. form $N_Z \times N_b$ decimated-filtered-modulated beamforming matrix a-priori: $\mathbf{Z} = \mathcal{D}\mathcal{F}\boldsymbol{M}\ \{\boldsymbol{W}\}$. form a set of vectors, $\boldsymbol{\beta}_i$, $i = 1, \ldots, N_Z - N_b$, that span a subspace orthogonal to range$\{\mathbf{Z}\}$.

2. EVD of $\hat{\mathbf{R}}_y = \sum_{m=1}^{M} \mathbf{y}(m)\mathbf{y}^H(m)/M$, where $\mathbf{y}(m) = \mathbf{W}^H\mathbf{x}(m)$ m=1,...,M.

3. estimate number of sources, K, and form the matrix $\mathbf{E}_{Z_s}$ composed of vectors which span the estimated decimated signal subspace:

$$\hat{\mathbf{E}}_{Z_s} = \left[\mathbf{Z}(\mathbf{Z}^H\mathbf{Z})^{-1}\hat{\mathbf{e}}_1 \vdots \ldots \vdots \mathbf{Z}(\mathbf{Z}^H\mathbf{Z})^{-1}\hat{\mathbf{e}}_{\hat{K}} \vdots \boldsymbol{\beta}_1 \vdots \ldots \vdots \boldsymbol{\beta}_{N_Z - N_b}\right]$$

4. form $(N_Z - 1)$ x $2(N_Z - N_b + \boldsymbol{k})$ matrix $\hat{\mathbf{E}}_{xy} \doteq \left[\hat{\mathbf{E}}_1 \,|\, \hat{\mathbf{E}}_2\right]$ where $\hat{\mathbf{E}}_1$ and $\hat{\mathbf{E}}_2$ are the first and last N_Z-1 rows of $\hat{\mathbf{E}}_{Z_s}$, and compute the $2(N_Z - N_b + I;')$ x $2(N_Z - N_b + I?)$ EVD $\hat{\mathbf{E}}_{xy}^H\hat{\mathbf{E}}_{xy} = \hat{\mathbf{E}}\hat{\boldsymbol{\Sigma}}\hat{\mathbf{E}}^H$

5. partition E into $(N_Z - N_b + I?)$ x $(N_Z - N_b + \hat{K})$ submatrices:

$$\hat{\mathbf{E}} = \begin{bmatrix} \hat{\mathbf{E}}_{11} & \hat{\mathbf{E}}_{12} \\ \hat{\mathbf{E}}_{21} & \hat{\mathbf{E}}_{22} \end{bmatrix}.$$

6. compute the $(N_Z - N_b + \hat{K}) \times (N_Z - N_b + \hat{K})$ EVD $\mathbf{T}\Phi\mathbf{T}^{-1} = -\hat{\mathbf{E}}_{12}\hat{\mathbf{E}}_{22}^{-1}$

7. for those K nearly unit-magnitude eigenvalues $\lambda_i = \Phi_{ii}$, estimate the corresponding signal arrival direction as $\hat{\theta}_k = sin^{-1}(angle\{\lambda_i\}\lambda/2\pi dD)$

4.2.4.1 *Location of Extraneous Roots Created by Filtering*

A major concern is that the extra column dimension of $\mathbf{E}_{Z_s}$ over the K-dimensional signal subspace will result in the declaration of ambiguous signals. First of all, note that we've already at this point estimated the number of signal arrivals. Here, an argument is presented that suggests that the extraneous roots will not lie near the unit circle. This claim is also verified via a simulation example in Section 4.4.

First, note that in the case of ideal decimation where the filter exhibits a perfect low-pass nature, equation ***(4.20)*** applies. Recall that the k'th diagonal element of Φ has unit magnitude, $\Phi_k = e^{jD\mu_k}$. Now consider the inclusion. of a linear filter in the decimation operation. The aliasing effects caused by decimation will result in an ESPRIT signal eigenvalue that will not have a unit magnitude characteristic, even if the ideal beamspace covariance matrix is available. However, a judicious filter and beamformer design will result in an approximate unit-magnitude eigenvalue characteristic.

In addition to ESPRIT eigenvalues directly corresponding to signals, assume that there is an extraneous unit magnitude eigenvalue, $A_,$, i.e.,

$$\Gamma_1 \mathbf{E}_{Z_s} - \lambda_* \Gamma_2 \mathbf{E}_{Z_s} = \mathbf{0}.$$

This suggests that, in addition to the Vandermonde components arising from the true signals, a Vandermonde vector corresponding to the angle ***Dp,*** also lies in the decimated signal subspace. Equivalently, $\mathbf{a}_{N_Z}^H(D\mu_*)$ is orthogonal to the range of ZE,, so that

$$\mathbf{a}_{N_Z}^H(D\mu_*) \left[\mathbf{Z}\mathbf{E}_n\mathbf{E}_n^H\mathbf{Z}^H \right] \mathbf{a}_{N_Z}(D\mu_*) = 0.$$

Thus the spectrum of every transformed and decimated beamspace noise eigenvector exhibits a null at the spatial location $D\mu_*$. By design, there are no common in-band beamformer nulls and the filter response is also non-zero across the spatial sector of interest so that λ_* must be an ESPRIT eigenvalue associated with a signal arrival.

Refer to Figure 4.6 where a Hamming-weighted LPF was employed as the decimation filter applied to noise eigenvectors generated from an $N_b = 8$ spatial DFT beamformer. The filter has an associated spatial response that is relatively flat across the subband and there are no common in-band nulls in the set of beamforming vectors. Note that the only nulls in the MUSIC null spectrum correspond to signal arrival angles. The behavior at the edges of the band is expected from the presence of a root near π at a radius of 0.9 as shown in Figure 4.7. As a result of the relationship between the ESPRIT eigenvalues and the roots generated from Root-MUSIC, it is anticipated that an extraneous ESPRIT eigenvalue will lie in the complex plane near the unit circle at π and that all other non-signal eigenvalues will be sufficiently displaced from the unit circle. This is acceptable since these eigenvalues are discarded anyway as a result of previous discussion. In summary, an ESPRIT eigenvalue with a nearly unit magnitude suggests the presence of a signal at an associated spatial angle as long as the filter and beamforming vectors are judiciously designed.

4.3 Theoretical Performance Analysis

As previously observed, the use of conjugate centro-symmetric beamforming in conjunction with uniformly-spaced linear arrays with phase referencing at the array center results in a purely real-valued beamspace manifold. The real-valued property of the manifold allows one to decompose only the real part of the sample covariance matrix to determine the signal or noise subspaces. In addition to the obvious computational advantages of a real-valued decomposition, a performance benefit is realized through the decorrelation of correlated signals. In uncorrelated signal environments, the real and complex-valued procedures result in similar performances in terms of estimation variance; however, the bias is, in general, smaller with the use of real

covariance processing. As a result of these advantages as well as the applicability of either approach with regard to the Root-MUSIC and ESPRIT based procedures incorporating eigenvector decimation, the theoretical performance of the two algorithmic approaches are derived for the case of real-covariance processing. Extension for the case of complex processing is readily determined.

As before, define $\Delta\mathbf{e}_i = \hat{\mathbf{e}}_i - \mathbf{e}_i$, i=1,...,K as the error in the i'th eigenvector due to the use of a sample estimate of the covariance matrix where $\hat{\mathbf{e}}_i$ and $\mathbf{e}_i$ are the respective i'th eigenvectors obtained from the beamspace sample covariance matrix and the ideal covariance, under some common uniqueness criterion. The distribution of $\Delta\mathbf{e}_i$ was shown in Appendix D to be asymptotically Gaussian with zero mean and covariance

$$\mathcal{E}\{M\,\Delta\mathbf{e}_k\Delta\mathbf{e}_\ell^T\} = \sum_{\substack{m=1\\m\neq k}}^{N_b}\sum_{\substack{n=1\\n\neq \ell}}^{N_b} \frac{\Gamma_{mn\ell k}}{(\lambda_k-\lambda_m)(\lambda_\ell-\lambda_n)}\mathbf{e}_m\mathbf{e}_n^T,\quad k,\ell=1,\ldots,K \quad [4.22]$$

$$\begin{aligned}\Gamma_{mn\ell k} = \frac{1}{2}\{\ & \lambda_k\lambda_\ell\delta_{m\ell}\delta_{nk} + \lambda_k\lambda_m\delta_{mn}\delta_{k\ell} \\ & + (\mathbf{e}_m^T\mathbf{R}_I\mathbf{e}_\ell)(\mathbf{e}_k^T\mathbf{R}_I\mathbf{e}_n)(1-\delta_{m\ell})(1-\delta_{kn}) \\ & + (\mathbf{e}_m^T\mathbf{R}_I\mathbf{e}_n)(\mathbf{e}_k^T\mathbf{R}_I\mathbf{e}_\ell)(1-\delta_{mn})(1-\delta_{k\ell})\}\end{aligned} \quad [4.23]$$

$$\mathbf{R}_I = \mathcal{I}m\{\mathbf{R}\} = \mathbf{B}\,\mathcal{I}m\{\mathbf{P}_S\}\,\mathbf{B}^T. \quad [4.24]$$

To allow for the use of previous MUSIC and ESPRIT [42] performance analyses, it is assumed that the aliasing effects are negligible. As noted earlier, the assumption is valid when the decimation operation includes a judiciously designed filter. This condition may be verified by observing the placement of the (signal) MUSIC roots/ESPRIT eigenvalues in the case of a known ideal covariance. Once again, the Root-MUSIC signal locations for the motivational example shown in Figure **4.7** confirm the validity of the assumption, particularly in the case where deconvolution is not employed.

4.3.1 Performance Analysis of Root-MUSIC Formulation

The asymptotic variance of the Root-MUSIC estimator is readily obtained using available results when assuming orthogonality between the transformed-filtered-decimated beamspace noise eigenvectors and the decimated element-space manifold, i.e., $\mathbf{Z}\,\mathbf{e}_i \overset{\perp}{\sim} \mathbf{a}_{N_Z}(\theta_k)$, k $= 1,...,K$, $i = K+1,...,N_b$. By observing that the spectral and Root-MUSIC formulations offer the same asymptotic performance in terms of the variance as shown in [10], the expression for the spectral MUSIC estimate variance employing real-covariance processing in Chapter 3 can be easily amended to the case at hand. Specifically, the null spectrum can be written as

$$\begin{aligned}\mathcal{N}_{MU}(\theta) &= \mathbf{a}_{N_Z}^H(\theta)\left\{\sum_{i=K+1}^{N_b}(\mathbf{Z}\hat{\mathbf{e}}_i)(\mathbf{Z}\hat{\mathbf{e}}_i)^H\right\}\mathbf{a}_{N_Z}(\theta)\\ &= \mathbf{a}_{N_b}^H(\theta)\,\mathbf{Z}\left\{\mathbf{I}_{N_b}-\sum_{i=K+1}^{N_b}\hat{\mathbf{e}}_i\,\hat{\mathbf{e}}_i^T\right\}\mathbf{Z}^H\,\mathbf{a}_{N_b}(\theta). \qquad [4.25]\end{aligned}$$

Observing the results in Chapter 3, the asymptotic variance of the Root-MUSIC estimator is easily shown to be expressed by

$$\mathcal{A}\mathrm{Var}\{\hat{\theta}_i\} = \frac{\sum_{k=1}^{K}\frac{\lambda_k\sigma_n^2}{(\lambda_k-\sigma_n^2)^2}\left|\mathbf{e}_k^T\mathbf{Z}^H\mathbf{a}_{N_Z}(\theta_i)\right|^2}{M\,\dot{\mathbf{a}}_{N_Z}^H(\theta_i)\mathbf{Z}\mathbf{E}_n\mathbf{E}_n^T\mathbf{Z}^H\dot{\mathbf{a}}_{N_Z}(\theta_i)}\quad i=1,...,K, \qquad [4.26]$$

where M is the number of snapshots, $\dot{\mathbf{a}}_{N_Z}(\theta_i)$ is the derivative of $\mathbf{a}_{N_Z}(\theta)$ with respect to the location parameter θ and evaluated at $\theta = \theta_i$, and $(\lambda_k\,,\,\mathbf{e}_k)$, k=1,...,K, are the signal eigenvalues and corresponding eigenvectors of the real part of the ideal beamspace covariance matrix.

4.3.2 Performance Analysis of ESPRIT Formulation

The alternate expression in equation (4.21) for the decimated signal subspace involving the transformed beamspace signal eigenvectors and a non-random basis for the orthogonal subspace of the columns of Z allows for an asymptotic analysis of the ESPRIT formulation. The error in the matrix whose columns form a basis for the decimated signal subspace, $\Delta\mathbf{E}_{Z_s}$, is simply

$$\Delta\mathbf{E}_{Z_s} = \left[\mathbf{Z}(\mathbf{Z}^H\mathbf{Z})^{-1}\Delta\mathbf{e}_1\,\vdots\,\ldots\,\vdots\,\mathbf{Z}(\mathbf{Z}^H\mathbf{Z})^{-1}\Delta\mathbf{e}_K\,\vdots\,\mathbf{0}_{N_Z\times(N_Z-N_b)}\right]. \qquad [4.27]$$

In this form, the error is only a function of the error in the eigenvectors associated with the signal eigenvalues of the beamspace covariance. This allows for an asymptotic variance analysis similar to that found in [42]. The analysis in [42] is valid for the Least-Squares (LS) and Total Least-Squares (TLS) versions of ESPRIT. The variance analysis, for real beamspace covariance processing, is included in Appendix E. The asymptotic variance associated with the i'th angle estimate in the case of uncorrelated sources is

$$\begin{aligned}
\mathcal{E}\{(\Delta\theta_i)^2\} &= \left[\frac{\lambda}{2\pi d D\cos\theta_i}\right]^2 \frac{1}{2M}\left[\sum_{k=1}^{K}\frac{\sigma_n^2\lambda_k}{(\lambda_k-\sigma_n^2)^2}\left|\mathrm{Im}\left\{x_i(k)\mathbf{E}_n^T\boldsymbol{\alpha}_i\right\}\right|^2\right. \\
&+ \sum_{k=1}^{K}\sum_{\substack{\ell=1\\ \ell\neq k}}^{K}\frac{\lambda_k\lambda_\ell}{(\lambda_k-\lambda_\ell)^2}\left(\mathrm{Im}\left\{x_i(\ell)\mathbf{e}_k^T\boldsymbol{\alpha}_i\right\}^2\right. \\
&- \left.\left.\mathrm{Im}\left\{x_i(\ell)\mathbf{e}_\ell^T\boldsymbol{\alpha}_i\right\}\mathrm{Im}\left\{x_i(k)\mathbf{e}_k^T\boldsymbol{\alpha}_i\right\}\right)\right], \qquad [4.28]
\end{aligned}$$

$$\boldsymbol{\alpha}_i = (\mathbf{Z}^H\mathbf{Z})^{-1}\mathbf{Z}^H[\boldsymbol{\Gamma}_1 - z_i^*\boldsymbol{\Gamma}_2]^H([\boldsymbol{\Gamma}_1\mathbf{E}_{Z_s}]^\dagger)^H\mathbf{q}_i, \qquad [4.29]$$

$$\mathbf{E}_n = \left[\mathbf{e}_{K+1}\vdots\ldots\vdots\mathbf{e}_{N_b}\right], \qquad [4.30]$$

where † denotes pseudoinverse, $\mathbf{x}_i$ and $\mathbf{q}_i$ are the right and left eigenvectors associated with the i'th (signal) eigenvalue of $\mathrm{F} = (\boldsymbol{\Gamma}_1\mathbf{E}_{Z_s})^\dagger\boldsymbol{\Gamma}_2\mathbf{E}_{Z_s}$, and $\boldsymbol{\Gamma}_1$ and $\boldsymbol{\Gamma}_2$ are $(N_Z - 1)$ x N_Z matrices that select the first and last $N_Z - 1$ rows of a matrix with N_Z rows, respectively. Note that the expressions contained in Appendix E may be applied to the more general case of correlated signals; only the result for the uncorrelated signal scenario is summarized here due to its simpler form.

4.4 Computer Simulations

A number of simulations were conducted to assess the validity of the noise eigenvector transformation/decimation techniques with regard to angle estimation. Specifically, the theoretical and empirical standard deviations of the Root-MUSIC and TLS-ESPRIT estimators were compared in a variety of source/processing scenarios. Also, the performance of the decimation approach was compared to the stochastic Cramer-Rao Lower Bound [26, 43].

Common to all experiments, 600 trials were employed to derive the empirical results and only $M = 16$ snapshots were used to estimate the beamspace covariance matrix. Although this situation can hardly be classified as asymptotic in the number of snapshots, the theoretical performance curves were observed to compare rather closely to the derived experimental results.

The empirical standard deviations were computed in a variety of scenarios involving one or two uncorrelated, closely-spaced signals. A MUSIC root or ESPRIT eigenvalue was classified as arising from a signal if the root/eigenvalue location was within a 0.15 radial distance from the unit circle and lying in an angular (decimated) region encompassing 85% of the unit circle, i.e., in the region $[-0.85\pi, 0.85\pi]$. All trial cases, including those unresolved situations where only one signal was observed in the neighborhood of a signal pair, were used to compute the location statistics.

Experiment 1: The simulation parameters of this experiment associated with the array, beamformer, and decimation components are similar to those outlined in the example of Section 3, namely, an $N = 128$ element ULA with half-wavelength spacing was operated on with an $N_b = 8$ channel spatial DFT beamformer. The spatial window was centered at broadside so that the spatial region $-N_b/N \leq \sin\theta \leq N_b/N$ was probed. An $L = 128$ length Hamming-weighted low-pass filter was employed in the decimation procedure configured for maximal decimation, i.e., $D = N/N_b$.

Two half-Rayleigh spaced signals of equal power were embedded in additive complex Gaussian noise so that a sensor level 10 dB SNR was achieved. To assess the effects of signal placement within the spatial beamforming sector on the estimation variance, the center of the signal set was shifted from baseband ($\sin 0 = 0$) to the edge of the window ($\sin 0 = 8/N$). The empirical standard deviation of the two Root-MUSIC angle estimators, i.e., those formed using the matrix $\mathbf{Z}$ as well as the deconvolved version $\mathbf{Z}'$, were computed. Note that the dimension of $\mathbf{Z}$ was 16×8 while $\mathbf{Z}'$ was formed by adding one additional (remainder) row to the required $(N_b + 1) \times N_b$ matrix to form a 10 x 8 eigenvector transformation. The results are shown, along

with the theoretical prediction as obtained from equation (4.26) and the stochastic Cramer-Rao Lower bound [26, 43] in Figure 4.11.

Several comments relating to Figure 4.11 are in order. Although the number of snapshots is relatively small, the theoretical performance curve is still a reasonably accurate representation of the empirically derived result. The rippled nature of the variance curves is due to the limited number of beams that are implemented in the approach. This characteristic is the result of a varying spatial power gain as similar to that depicted in Figure 4.10. As noted earlier, the degradation in performance near the band edge suggests the need for sub-band overlap if one is interested in the detection and localization of all signals across the visible spatial spectrum. The variance of the estimate at the extreme right edge is not shown as the experimental and theoretical curves exhibit an exponential rise. In the central region of the band, however, the eigenvector transformation-decimation technique is seen to produce an accurate estimate in this Root-MUSIC formulation as evidenced by the closeness of the results to the Cramer-Rao Bound. Note that the curves related to the theoretical variance associated with the use of Z and the Cramer-Rao Bound overlap.

Experiment 2: Employing the same decimation transformations as in Experiment 1, the variance of the Root-MUSIC estimators were observed for a varying SNR for two signals located at $10.6°$ and $11.5°$, as used in the motivational example of Figures 4.2 through 4.7. The empirical and theoretical standard deviations were computed and are depicted in Figure 4.12.

Note that the theoretically derived curve, defined for the 16 x 8 transformation $\mathbf{Z}$, closely tracks the corresponding empirical counterpart at moderate to high SNR values. The deviation at the lower SNR values is attributed to the signal-merging effects in the resolution threshold regime of operation as noted in Chapter 3. Although the stochastic Cramer-Rao Bound is based upon the statistics of the available beamspace data and does not assume the presence of any sub-optimal techniques such as decimation, the Root-MUSIC procedure incorporating decimation is readily

observed to essentially offer the optimum performance associated with un-biased estimators. Also, the similarity between the empirical variance curves corresponding to the competing approaches ($\mathbf{Z}$ versus $\mathbf{Z}'$) suggests that the computational savings associated with the smaller Root-MUSIC polynomial via the use of $\mathbf{Z}'$ is not obtained at the expense of a higher estimation variance. In fact, simulations have shown that the estimation variance is usually smaller for decimation architectures incorporating deconvolution. However, the imperfect deconvolution usually results in an induced estimate bias as will be observed in Experiment 3.

Experiment 3: The main purpose of this experiment is to show that the filtering operation in the decimator may not be warranted in certain situations. A single signal was positioned at 1° and the bias performance was studied for the use of two beamforming architectures. In one situation, $N_b = 6$ DFT beams were formed from an N = 36 element ULA. The beamspace to element-space eigenvector transformation was configured for maximal decimation, D = 6, with and without the use of a Parks-McClellan equiripple FIR filter exhibiting approximately 50 dB attenuation in the stopband region. In the other beamforming scenario, a practical application of $N_b = 6$ Taylor weighted beams [45], exhibiting a 50 dB sidelobe level, were spaced at the half-power points and employed in a similar scheme involving the use/absence of additional filtering in the decimation operation. Note that the latter approach will produce an angle estimate exhibiting a substandard resolution ability due to the attendant wider mainlobes relative to DFT beams. However, this methodology is often required in practice to reduce the deleterious effects of sidelobe clutter, i.e., the masking of signals within a given beam by a strong clutter signal in the sidelobes of the beam. The beam spacing/aperture weighting associated with this case results in no common spatial nulls amongst the beam set so that the application of past beamspace MUSIC (Chapter 2) and ESPRIT [40] formulations is precluded.

The empirically derived mean location estimates were determined for a varying SNR for various schemes incorporating the two beamforming architectures and are

plotted in Figure 4.13. Again, the purpose here is not to compare the two beamforming approaches, rather, it is to observe the effects on performance of the inclusion of a filter in the decimation operation. Also, the inclusion of a filter increases the order of the polynomial to be rooted thereby increasing computation and creating extraneous roots. With reference to Figure 4.13, note that the use of a filtering operation in the decimator with no additional deconvolution stage results in essentially an unbiased estimator for both beamforming architectures. As observed in the results, the Taylor-based sensor weighting provides sufficient attenuation so that a negligible aliasing effect is incurred, i.e., the induced estimation bias is small. However, with the filter incorporated into the decimation operation, the imperfect deconvolution stage imparts a small bias of $-0.02''$. Thus the filtering operation is unnecessary as evidenced in the bias plot and a smaller standard deviation should be realized on account of the smaller dimension of the resulting Root-MUSIC polynomial.

Essentially the opposite is observed for the case of unweighted spatial DFT beamforming. Here the sidelobe levels are large so that aliasing effects are present as evidenced by the top curve indicating a $0.05°$ bias in the unfiltered mode of operation. With filtering as well as a deconvolution stage included in the decimation operation, a smaller bias of $0.025''$ is realized. The need for filtering is evident from observing the required dimension of the transformation $\mathbf{Z}'$. Comparing the necessary row dimension of the decimation transformation incorporating deconvolution, $\mathbf{Z}'$ for the unweighted DFT and Taylor beamformers, the required sizes were 10×6 and 7×6, respectively. These required sizes were determined according to the criteria discussed in Section 4.2.

Experiment 4: In this experiment, we test the validity of the TLS-ESPRIT formulation of the noise eigenvector transformation-decimation procedure and verify the theoretical variance expression of Section 4.3, equation (4.28). The source/processing parameters are the same as those of Experiment 2.

The theoretical and empirical standard deviation were computed over a varying SNR and the results are depicted in Figure 4.14. The results show that the performance predictor of Section 4.3 accurately tracks the empirical results. Also, the variance associated with the decimation architecture incorporating a filter deconvolution stage outperforms the "undeconvolved" counterpart. To verify the conjecture that the quiescent locations of the extraneous eigenvalues are sufficiently away from the unit circle, the ESPRIT eigenvalues were calculated in the absence of noise and plotted in Figure 4.15. Note that only the eigenvalues interior to the unit circle are plotted as the closest exterior eigenvalue is located at a radius of 5.4 (associated with the Z transformation). Referring to Figure 4.15, in the absence of deconvolution, two "signal" eigenvalues appear at the correct location and the eigenvalue closest to the unit circle of the remaining is located at a radius of 0.62 and an angle very near π. When deconvolution is incorporated, the closest non-signal eigenvalue is located at π at a radius of 0.09. However, the signal eigenvalues exhibit a small bias at the perceived (translated) angular locations of 10.587' and 11.465'.

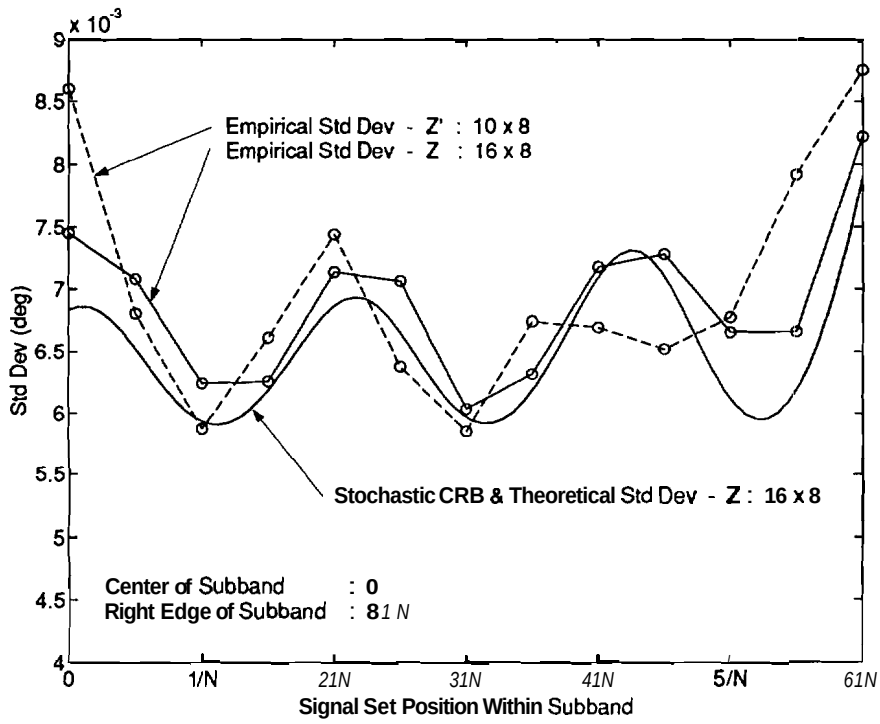

Figure 4.11 Experiment 1: Empirical and theoretical left signal standard deviation versus spatial position of a 10dB, half-Rayleigh spaced signal set. Central position of signal set varied from mid-band to $6/N$. The $N_b = 8$ spatial DFT beams were formed on an N = 128 sensor ULA.

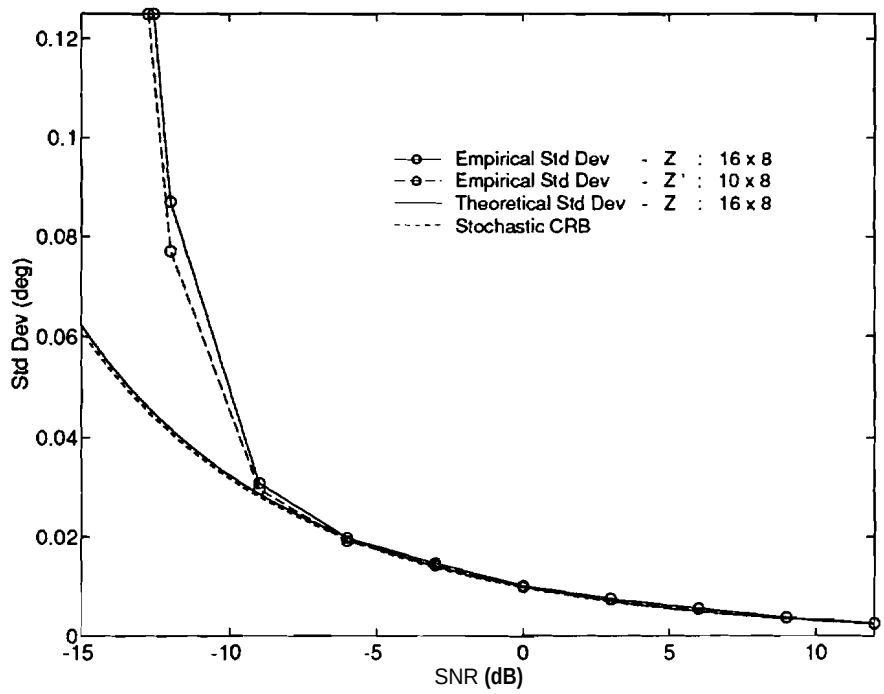

Figure 4.12 Experiment 2: Left signal standard deviation versus source SNR for the two in-band signal, $N_b = 8$ beam example scenario depicted in Figure **4.3.**

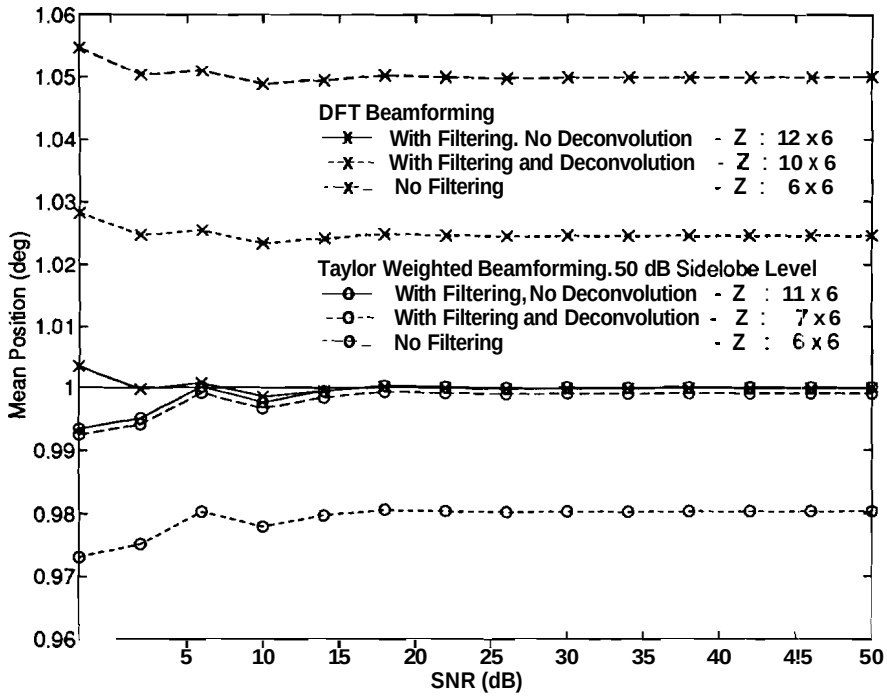

Figure 4.13 Experiment 3: Location bias versus source SNR for an $N_b = 6$ beam pre-processor (un-weighted DFT or Taylor-weighted beamformers) operating on an N = 36 sensor ULA. The mean angle estimate for a signal located at 1° was computed over 600 trials.

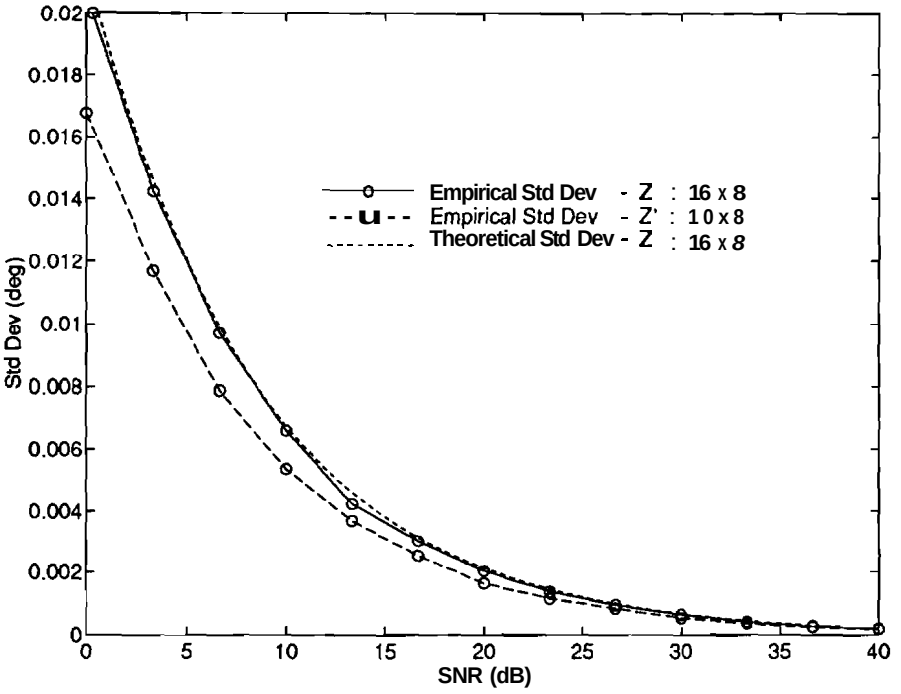

Figure 4.14 Experiment 4: TLS-ESPRIT left signal standard deviation versus source SNR for the two signal example of Figure 4.12.

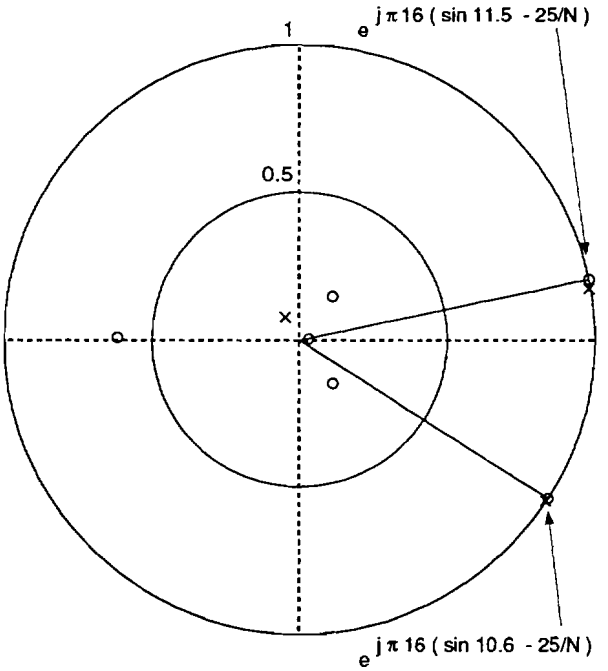

Figure 4.15 Experiment 4: Quiescent locations of the TLS-ESPRIT eigenvalues associated with the decomposition of the ideal beamspace covariance input.

4.5 Conclusions

In this chapter, a novel approach to angle estimation in the beamspace domain was developed. The approach offers a computationally attractive and non-restrictive procedure relative to the type of beamformer employed that is easily implemented in the MUSIC and ESPRIT algorithms. Theoretical expressions for the estimate variance were obtained in an asymptotical analysis and confirmed in a variety of simulations. Although the technique was applied to the uniform linear array geometry, an extension to a two-dimensional array to provide simultaneous azimuth/elevation angle estimates is evident and currently under investigation.

5. CONCLUDING REMARKS

In this report, two computationally efficient formulations of a beamspace Root-MUSIC algorithm were developed. Although similar implementations were obtained, the two methodologies were designed under fundamentally different approaches. The first approach of Chapter 2 resulted in a slightly more efficient implementation, relative to the algorithm in Chapter 4, but at the expense of a restrictive constraint placed on the form of the beamforming transformation.

A conjugate centro-symmetric structural requirement on the form of the beamforming vectors was shown to allow for a real-valued decomposition of the beamspace sample covariance to derive information on the estimated signal subspace. The constraint is not a severe one as a symmetric weighting/sensor placement is commonly used in practice. Although the performance benefit of incorporating real-valued processing in a MUSIC formulation was somewhat discussed in Chapter 2, the performance analysis in Chapter 3 provided detailed insight into the merit of such a processing approach. The derived large-sample statistics for the signal subspace eigenvectors of the real part of the beamspace sample covariance matrix were employed to develop the theoretical estimate bias/variance of the algorithms in Chapters 2 and 4. The accompanying simulations verified the theoretical expressions and served to validate the merit of the two algorithms.

Two extensions of this work are currently under investigation. First, as mentioned in Section 4.5, the multirate noise eigenvector processing technique may be applied to a two-dimensional planar array of sensors situated in a rectangular lattice to provide the elevation and azimuth coordinates of an impinging wavefront. In this mode, the beams are pointed to spatial locations in a two-dimensional grid and decimation is performed along the vertical and horizontal axes of the array. Another extension to

the algorithm of Chapter 4 is the incorporation of procedures to allow for adaptive beamforming, where beams are adaptively derived to exhibit nulls in the (out-of-sector) locations corresponding to interfering sources.

A sensitivity comparison between the two approaches is also under consideration. The application to data from a digital line array would allow a comparison between the two techniques with regard to the sensitivity in the presence of sensor placement perturbations, mutual coupling, etc. It is anticipated that the algorithm of Chapter 4 will be found to be more robust due to the absence of the common-null beamforming constraint.

BIBLIOGRAPHY

[1] A. J. Barabell, "Improving the Resolution Performance of Eigenstructure-Based Direction-Finding Algorithms," in Proc. of *1983* IEEE Int'l. Conf. on Acoust., Speech, and Sig. Proc., pp. 336-339, May 1983.

[2] G. Bienvenu and L. Kopp, "Decreasing High Resolution Method Sensitivity by Conventional Beamformer Prepocessing," in Proc. of *1984* IEEE Int'l Conf. on Acoust., Speech, and Sig. Proc., pp. 33.2.1-33.2.4, April 1984.

[3] Y. Bresler and A. Macovski, "Exact Maximum Likelihood Parameter Estimation of Superimposed Exponential Signals in Noise," IEEE Trans. Acoust., Speech, and Signal Proc., vol. ASSP-34, no. 5, pp. 1081-1089, Oct. 1986.

[4] C. L. Byrne and A. K. Steele, "Sector-focused stability for high-resolution array processing," in Proc. of *1987* IEEE Int'l. Conf. on Acoust., Speech, and Sig. Proc., pp. 2340-2343, April 1987.

[5] G. Golub and C. Van Loan, Matrix Computations, John Hopkins University Press, Baltimore, MD, Chap. 12, 1983.

[6] H. Lee and M. Wengrovitz, "Improved High-Resolution Direction-Finding Through the Use of Inhomogeneous Constraints," in Proc. of Fourth ASSP Workshop on Spect. Est. and Modeling, pp. 152-157, Aug. 1988.

[7] H. Lee and M. Wengrovitz, "Resolution Threshold of Beamspace MUSIC for Two Closely-Spaced Emitters," IEEE Trans. Acoust., Speech, Signal Process., vol. ASSP-38, no. 9, pp. 1545-1559, Sept. 1990.

[8] S. U. Pillai and B. H. Kwon, "Performance Analysis of MUSIC-Type High-Resolution Estimators for Direction Finding in Correlated and Coherent Scenes," IEEE Trans. Acoust., Speech, Signal Process., vol. ASSP-37, no. 8, pp. 1176-1189, Aug. 1989.

[9] B. D. Rao and K. V. S. Hari, "Statistical Performance Analysis of the Minimum Norm Method," IEE Trans. Part F: Radar and Signal Process., June 1989.

[10] B. D. Rao and K. V. S. Hari, "Performance Analysis of Root-MUSIC," IEEE Trans. Acoust., Speech, Signal Process., vol. ASSP-37, no. 12, pp. 1939-1949, Dec. 1989.

[11] R. O. Schmidt, "Multiple emitter location and signal parameter estimation," IEEE Trans. Antennas and Propagation, vol. AP-34, no. 3, pp. 276-280, Mar. 1986.

[12] S. D. Silverstein, W. E. Engeler, and J. A. Tardif, "Multirate Superresolution Line Spectrum Analyzers," IEEE Trans. Circuit and Systems, pp. 449-453, April 1991.

[13] S. D. Silverstein and M. D. Zoltowski, "The Mathematical Basis for Element and Fourier Beam Space MUSIC and Root-MUSIC Algorithms," *Digital* Signal Processing, Academic Press, vol. 1, no. 4, pp. 1-15, July 1991.

[14] M. I. Skolnik, Introduction to Radar Systems, McGraw-Hill, New York, 1980.

[15] B. D. Steinberg, Principles *of* Aperture and Array System Design, John Wiley and Sons, New York, 1976.

[16] M. Wax and T. Kailath, "Detection of Signals by Information Theoretic Criteria," IEEE Trans. Acoust., Speech, Signal Proc., vol. ASSP-33, pp. 387-392, April 1985.

[17] X. L. Xu and K. M. Buckley, "Statistical Performance Comparison of MUSIC in Element Space and Beam-Space," in Proc. *of* 1989 IEEE *Int'l Conf.* on Acoust., Speech, and Signal Process., pp. 2124-2127, May 1989.

[18] M. D. Zoltowski, "High Resolution Sensor Array Signal Processing in the Beamspace Domain: Novel Techniques Based on the Poor Resolution of Fourier Beamforming," in Fourth ASSP Workshop on Spectrum Estimation *and* Modeling, pp. 350-355, Aug. 1988.

[19] M. Zoltowski, G. M. Kautz, and S. D. Silverstein, "Simultaneous Sector Processing Via ROOT-MUSIC For Large Sensor Arrays," in Proc. *Fifth* ASSP *Workshop* on Spect. Est. and Modelling, pp. 317-321, Oct. 1990.

[20] K. M. Buckley and X. L. Xu, "Spatial-Spectrum Estimation in a Location Sector," IEEE Trans. Acoust., Speech, Signal *Proc.*, vol. 38, no. 11, pp. 1842-1852, Nov. 1990

[21] M. Kaveh and A. J. Barabell, "The Statistical Performance of the MUSIC and the Minimum-Norm Algorithms in Resolving Plane Waves in Noise," IEEE *Trans.* Acoust., Speech, and Signal Proc., vol 34, no.2, pp.331-341, April 1986.

[22] V. F. Pisarenko, "The Retrieval of Harmonics from a Covariance Function," Geophys. J. Roy. Astron. *Soc.*, vol 33, pp. 247-266, 1973.

[23] R. Kumaresan and D. W. Tufts, "Estimating the Angle of Arrival of Multiple Plane Waves," IEEE Trans. Aerosp. Electron. *Syst.*, vol. AES-19, pp. 134-139, Jan. 1983

[24] R. Roy and T. Kailath, "ESPRIT-Estimation of Signal Parameters Via Rotational Invariance Techniques," IEEE Trans. Acoust., Speech., Signal Process., vol. ASSP-37, no. 9, pp. 984-995, July 1989.

[25] D. Slepian, "Prolate Spheroidal Wave Functions, Fourier Analysis, and Uncertainty - V: The Discrete Case," The Bell System Technical Journal, vol. 57, no. 5, 1978.

[26] R. O. Schmidt, "A Signal Subspace Approach to Multiple Emitter Location and Spectral Estimation," Ph.D. dissertation, Stanford University, Stanford, CA, 1981

[27] A. Paulraj, R. Roy, and T. Kailath, "Estimation of Signal Parameters via Rotational Invariance Techniques - ESPRIT," in Proc. *19-th* Asilomar Conf. on Signals, Systems and Computers, pp. 83-89, Nov. 1985.

[28] P. Stoica and A. Nehorai, "Comparative Performance Study of Element-Space and Beam-Space MUSIC Estimators," Circuits Systems *Signal* Process, vol. 10, no. 3, pp. 285-292, 1991.

[29] X.-L. Xu and K. M. Buckley, "An Analysis of Beam-Space Source Localization," IEEE Trans. on Signal Processing, vol. 41, pp. 501-504, Jan. 1993.

[30] J. E. Evans, J. R. Johnson, and D. F. Sun, "Applications of Advanced Signal Processing Techniques to Angle of Arrival Estimation in ATC Navigation and Surveillance System," M.I.T. Lincoln Lab., Lexington, MA, Tech. Report, Nov. 1982.

[31] T. Shan, M. Wax, and T. Kailath, "On Spatial Smoothing for Direction of Arrival Estimation of Coherent Signals," IEEE Trans. *Acoust.,* Speech, Signal Process., vol. ASSP-33, pp. 806-811, Aug. 1985.

[32] R. T. Williams, S. Prasad, A. K. Mahalanabis, and L. H. Sibul, "An Improved Spatial Smoothing Technique for Bearing Estimation in a Multipath Environment," IEEE Trans. Acoust., Speech, Signal Process., vol. ASSP-36, pp. 425-432, Apr. 1988.

[33] P. Stoica and A. Nehorai, "MUSIC, Maximum Likelihood, and Cramer-Rao Bound," IEEE Trans. Acoust., Speech, Signal Process., vol. ASSP-37, no. 5, pp. 720-741, May 1989.

[34] X.-L. Xu and K. M. Buckley, "Bias Analysis of the MUSIC Location Estimator," IEEE Trans. on Signal Processing, vol. 40, no. 10, pp. 2559-2569, October 1992.

[35] K. Sharman, T. S. Durrani, M. Wax, and T. Kailath, "Asymptotic Performance of Eigenstructure Spectral Analysis Methods," in Proc. of 1984 IEEE *Int'l* Conf. on Acoust., Speech, and Signal Process., pp. 45.5.1-45.5.4, April 1984.

[36] H. Wang and G. H. Wakefield, "Non-Asymptotic Performance Analysis of Eigenstructure Spectral Methods," *in Proc. of 1990 IEEE Int'l Conf. on Acoust., Speech, and Signal Process.*, pp. 2591-2594, 1990.

[37] F. Li and Y. Lu, "Unified Bias Analysis for DOA Estimation Algorithms," *in Proc. of 1993 IEEE Int'l Conf. on Acoust., Speech, and Signal Process.*, vol. IV, pp. 376-379, 1993.

[38] L. V. Blake, *Radar Range - Performance Analysis*, Lexington Books, 1980.

[39] P. Forster and G. Vezzosi, "Application of Spheroidal Sequences to Array Processing," *in Proc. of 1987 IEEE Int'l Conf. on Acoust., Speech, and Signal Process.*, pp. 53.3.1-53.3.4, April 1987.

[40] G. Xu, S. D. Silverstein, R. Roy, and T. Kailath, "Parallel implementation and Performance of Beamspace ESPRIT," *in Proc. of 1984 IEEE Int'l Conf. on Acoust., Speech, and Signal Process.*, pp. 1497-1500, April 1991.

[41] J. G. Proakis and D. G. Manolakis, *Introduction to Digital Signal Processing*, Macmillan, 1988.

[42] B. D. Rao and K. V. S. Hari, "Performance Analysis of ESPRIT and TAM in Determining the Direction of Arrival Plane Waves in Noise," *IEEE Trans. Acoust., Speech, Signal Process.*, vol. ASSP-37, no. 12, pp. 1990-1995, December 1989.

[43] P. Stoica and A. Nehorai, "Performance Study of Conditional and Unconditional Direction-of-Arrival Estimation," *IEEE Trans. Acoust., Speech, Signal Process.*, vol. ASSP-38, no. 10, pp. 1783-1795, October 1990.

[44] T. W. Anderson, *An Introduction to Multivariate Statistical Analysis*, Second ed., John Wiley & Sons, 1984.

[45] T. T. Taylor, "Design of Line-Source Antennas for Narrow Beamwidth and Low Side Lobes," *IRE Transactions on Antennas and Propagation*, pp. 16-28, January 1955.

APPENDICES

Appendix A: Simple Expression for $\mathbf{Q}_R^{(m)}$

A simple, closed-form expression for the $N_b \times 1$ beamspace vector $\mathbf{b}_R^{(m)}(u) = \mathbf{W}_N^{(m)H}\mathbf{a}_N(u)$ is first developed assuming the conjugate centro-symmetric form of the $N \times N_b$ DFT matrix beamformer in *(2.51)*. To this end, consider the inner product of $\mathbf{a}_N(u)$, where u is variable, with $\mathbf{a}_N(u)$ evaluated at some specific angle, say $u = u_k$. By direct substitution

$$\mathbf{a}_N^H(u)\mathbf{a}_N(u_k) = \sum_{i=1}^{N} \exp\left[-j\left(i - \frac{N+1}{2}\right)\pi(u - u_k)\right] = S_N(u - u_k) \qquad [A.1]$$

where $S_N(u)$ is the real-valued periodic sinc function

$$S_N(u) = \frac{\sin\left(\frac{N}{2}\pi u\right)}{\sin\left(\frac{1}{2}\pi u\right)}. \qquad [A.2]$$

It follows then that $\mathbf{b}_R^{(m)}(u)$ may be expressed in terms of shifted periodic sinc functions as

$$\mathbf{b}_R^{(m)}(u) = \mathbf{W}_N^{(m)H}\mathbf{a}_N(u) = \begin{bmatrix} S_N(u - m\frac{2}{N}) \\ S_N(u - [m+1]\frac{2}{N}) \\ \\ S_N(u - [m+N_b-1]\frac{2}{N}) \end{bmatrix} \qquad [A.3]$$

Invoking the banded, Toeplitz structure of $\mathbf{C}_R^{(m)}$ and the fact that $\mathbf{a}_N(u)$ is a scalar multiple of the Vandermonde manifold vector $\mathbf{v}_N(u)$, one arrives at a result similar to *(2.43)*:

$$\mathbf{b}_R^{(m)}(u) = \mathbf{W}_R^{(m)H}\mathbf{a}_N(u) = \mathbf{Q}_R^{(m)H}\mathbf{C}^{(m)H}\mathbf{a}_N(u) = c_R^{(m)}(u)\mathbf{Q}_R^{(m)H}\mathbf{a}_{N_b}(u) \qquad [A.4]$$

where $\mathbf{a}_{N_b}(u)$ is given by equation by *(2.48)* with N replaced by N_b. Here $c_R^{(m)}(u) = \mathbf{c}_R^{(m)H}\mathbf{a}_{N-N_b+1}(u)$, a scalar function of u equal to the DSFT of the sequence $\{\mathbf{c}_R^{(m)}\}$. In Appendix B, it is shown that if N may be factored as $N_b D$ where $D = N/N_b$ is an integer, $c_R^{(m)}(u)$ may be expressed as

$$c_R^{(m)}(u) = (-1)^m \exp\left[-jm\frac{\pi}{D}\right] \exp\left[j\frac{\pi}{2}\frac{(N_b-1)(D-1)}{D}\right] \prod_{n=m}^{m+N_b-1} S_D(u - m\frac{2}{N}) \qquad [A.5]$$

where $S_D(u)$ is defined by (A.2) with N replaced by $D = N/N_b$.

Consider the equality in (A.4) for N_b distinct values of u, i.e.,

$$c_R^{(m)}(u_i)\mathbf{Q}_R^{(m)H}\mathbf{a}_{N_b}(u_i) = \mathbf{b}_R^{(m)}(u_i), \quad i = 1, \ldots, N_b.$$

Collectively, this yields the matrix equation

$$\mathbf{Q}_R^{(m)\,H}\left[\mathbf{a}_{N_b}(u_1)\vdots\mathbf{a}_{N_b}(u_2)\vdots\ldots\vdots\mathbf{a}_{N_b}(u_{N_b})\right]\operatorname{diag}\{c_R^{(m)}(u_1), c_R^{(m)}(u_2), \ldots, c_R^{(m)}(u_{N_b})\} \qquad [A.6]$$

$$= \left[\mathbf{b}_R^{(m)}(u_1)\vdots\mathbf{b}_R^{(m)}(u_2)\vdots\ldots\vdots\mathbf{b}_R^{(m)}(u_{N_b})\right].$$

As long as the beamspace manifold vectors $\mathbf{b}_R^{(m)}(u_i)$, i=1,2,...,N_b, are linearly independent, (A.6) uniquely defines $\mathbf{Q}_R^{(m)}$. In Appendix C, it is shown that this is the case as long as the values u_i, i=1,2,...,N_b, are distinct with none equal to any of the common null locations listed in (2.23). To simplify the solution of (A.6) for $\mathbf{Q}_R^{(m)}$, consider selecting the values u;, i=1,2,...,N_b, such that $\mathbf{a}_{N_b}(u_i)$, i=1,2,...,N_b, are mutually orthogonal. Any set of N_b angles equi-spaced by $2/N_b$ will suffice. One is immediately tempted to choose $u_i = (i-1)2/N_b$, i=1,2,...,N_b. However, since N_b is assumed to be factor of N, i.e., $N = N_bD$, at least one member of this particular set of u values will lie at a common null location for which $\mathbf{b}_R^{(m)}(u)$ is identically zero. To insure against this and yet retain mutual orthogonality, these values are offset by $2k/N$ where $k \in \{1, 2, \ldots, N_b - 1\}$. It has been determined that an offset of $(N_b - 1)/N$ works best. Thus, with $u_i = (N_b - 1)/N + (i-1)2/N_b$, i=1,2,...,$N_b$, (A.6) is easily manipulated to yield a simple expression for $\mathbf{Q}_R^{(m)}$:

$$\mathbf{Q}_R^{(m)} = \frac{1}{N_b}\left[\mathbf{a}_{N_b}(u_1)\vdots\ldots\vdots\mathbf{a}_{N_b}(u_{N_b})\right]\operatorname{diag}\{1/c_R^{(m)}(u_1), \ldots, 1/c_R^{(m)}(u_{N_b})\}$$

$$\cdot\left[\mathbf{b}_R^{(m)}(u_1)\vdots\ldots\vdots\mathbf{b}_R^{(m)}(u_{N_b})\right]^T. \qquad [A.7]$$

The computation in (A.7) may be simplified by observing that the first matrix on the right-hand side of (A.7) is related to the N_b point DFT matrix, denoted $\mathbf{W}_{N_b}$, through a diagonal, unitary matrix. The diagonal elements of the latter matrix account for the offset of $(N_b - 1)/N$ in the DFT bins and the relationship between

$\mathbf{a}_N(u)$ and $\mathbf{v}_N(u)$ in *(2.50)*. In addition, the product of $1/c_R^{(m)}(u_i)$ with $\mathbf{b}_R^{(m)}(u_i)$ may be simplified invoking the expressions for $\mathbf{b}_R^{(m)}(u)$ and $c_R^{(m)}(u)$ in *(A.3)* and (A.5), respectively. Ultimately, *(A.7)* may be simplified as in *(2.38)* where γ_m is defined as

$$\gamma_m = (-1)^m \exp\left[-jm\frac{\pi}{D}\right] \exp\left[j\frac{\pi}{2}\frac{(N_b-1)(D-1)}{D}\right]. \qquad \text{[A.8]}$$

Appendix B: Simple Expression for DSFT of Coefficient Vector for Common Roots Polynomial

Given that $\mathbf{a}_{N-N_b+1}(u)$ is defined by (2.48) with N replaced by N – N_b + 1, it follows that $c_R^{(m)}(u) = \mathbf{c}_R^{(m)H}\mathbf{a}_{N-N_b+1}(u)$ is the Discrete Space Fourier Transform (DSFT) of the coefficient vector of the common roots polynomial of order N – N_b defined in (2.29) (normalized to exhibit conjugate centro-symmetry) multiplied by $\exp[-j\pi u(N - N_b)/2]$ in accordance with (2.50). Therefore,

$$c_R^{(m)}(u) = \exp\left(-j\frac{N-N_b}{2}\pi u\right)\prod_{n=m+N_b}^{m+N-1}\exp\left(-j\pi n\frac{1}{N}\right)\left(\exp\left[j\pi u\right] - \exp\left[j\pi n\frac{2}{N}\right]\right) \quad [B.1]$$

Recall that it is assumed that N_b is selected such that D = N/N_b is an integer. In this case, consider grouping the N – N_b roots into N_b sets having $D - 1$ roots each as signified by the following factorization

$$c_R^{(m)}(u) = \eta_m \exp\left(-j\frac{N-N_b}{2}\pi u\right)\prod_{n=m}^{m+N_b-1}\prod_{k=1}^{D-1}\left(\exp\left[j\pi u\right] - \exp\left[j\pi(n+N_bk)\frac{2}{N}\right]\right) \quad [B.2]$$

where

$$\begin{aligned}\eta_m &= \prod_{n=m}^{m+N_b-1}\prod_{k=1}^{D-1}\exp\left(-j\pi(n+N_bk)\frac{1}{N}\right)\\ &= \exp\left(-jm\frac{\pi}{N}\right)\exp\left(-jm\frac{\pi}{2}\frac{[N_b-1]}{D}\right)\exp\left(-jm\frac{\pi}{2}[D-1]\right)\end{aligned} \quad [B.3]$$

where we have used the identity

$$\prod_{k=1}^{K-1}\exp\left(kx\right) = \exp\left(\frac{x}{2}K[K-1]\right). \quad [B.4]$$

Factoring the half-angle out of each term in the product on the right-hand side of (B.2) yields

$$c_R^{(m)}(u) = \eta_m\varrho\prod_{n=m}^{m+N_b-1}\prod_{k=1}^{D-1}\exp\left(j\pi\left[\frac{u}{2}+\frac{n+N_bk}{N}\right]\right)2j\sin\left(\pi\left[\frac{u}{2}-\frac{n+N_bk}{N}\right]\right) \quad [B.5]$$

$$= \eta_m\varrho\prod_{n=m}^{m+N_b-1}\prod_{k=1}^{D-1}\exp\left(j\pi\left[\frac{u}{2}+\frac{n+N_bk}{N}\right]\right)2(-j)\sin\left(\pi\left[\frac{n}{N}-\frac{u}{2}\right]+\frac{k\pi}{D}\right)$$

where $\varrho = \exp\left(-j\frac{N-N_b}{2}\pi u\right)$. Using the identity

$$\frac{\sin(Kx)}{\sin(x)} = 2^{K-1}\prod_{k=1}^{K-1}\sin\left(x + \frac{k\pi}{D}\right) \qquad [B.6]$$

and the one in (B.4), simple algebraic manipulation yields

$$c_R^{(m)}(u) = (-1)^m \exp\left(\frac{-jm\pi}{D}\right)\exp\left(\frac{j\pi}{2}\frac{[N_b-1][D-1]}{D}\right)\prod_{n=m}^{m+N_b-1}\frac{\sin\left(\frac{D\pi}{2}\left[u - n\frac{2}{N}\right]\right)}{\sin\left(\frac{\pi}{2}\left[u - n\frac{2}{N}\right]\right)}. \qquad [B.7]$$

Appendix C: On the Distribution of the Real Part of the Beamspace Sample Covariance Matrix in the Case of Uncorrelated Gaussian Sources

Recall that N_b denotes the number of beams formed and K the number of sources. Irrespective of the tapering employed, the beamspace snapshot vector has the following general structure:

$$\mathbf{y}(n) = \mathbf{B}\mathbf{s}(n) + \mathbf{n}(n) \quad n = 1, ..., M \tag{C.1}$$

where B is N_b x IC, $\mathbf{s}(n)$ is K x 1, $\mathbf{n}(n)$ is N_b x 1, and M is the total number of snapshots. (Note that the superscript (m)'s and tildes have been dropped for notational simplicity.) B is the beamspace DOA matrix and is real-valued as proved in (2.56). The components of $\mathbf{s}(n)$ are the complex source amplitudes at the n-th snapshot, denoted $s_k(n)$, k = 1,..., K. As in [7], it is assumed that $s_k(n)$, $k = 1, ..., K$, are statistically independent, zero-mean, circular Gaussian random variables with $\mathcal{E}\{|s_k(n)|^2\} = \sigma_k^2$, k = 1,..., IC. The source covariance matrix is $\mathbf{P}_S = \text{diag}\{\sigma_1^2, \sigma_2^2, \ldots, \sigma_K^2\}$. Under these conditions, one can decompose $\mathbf{s}(n)$ into its real and imaginary parts as

$$\mathbf{s}(n) = \mathbf{s}_r(n) + j\mathbf{s}_i(n) \quad n = 1, ..., M \tag{C.2}$$

so that $\mathbf{s}_r(n)$ and $\mathbf{s}_i(n)$ are statistically independent and identically distributed (i.i.d.) with

$$\mathcal{E}\{\mathbf{s}_r(n)\mathbf{s}_r^T(n)\} = \mathcal{E}\{\mathbf{s}_i(n)\mathbf{s}_i^T(n)\} = \frac{1}{2}\mathbf{P}_S \quad n = 1, ..., M \tag{C.3}$$

Similarly, with respect to the noise, it is assumed that the elements of $\mathbf{n}(n)$ are samples of statistically independent, zero-mean, circular Gaussian random variables having a common variance of σ_n^2. Note that this assumes the use of orthonormal weight vectors in forming the beamspace snapshot vector. Similar to the above, one can decompose $\mathbf{n}(n)$ into its real and imaginary parts as

$$\mathbf{n}(n) = \mathbf{n}_r(n) + j\mathbf{n}_i(n) \quad n = 1, ..., M \tag{C.4}$$

so that $\mathbf{n}_r(n)$ and $\mathbf{n}_i(n)$ are i.i.d. with

$$\mathcal{E}\{\mathbf{n}_r(n)\mathbf{n}_r^T(n)\} = \mathcal{E}\{\mathbf{n}_i(n)\mathbf{n}_i^T(n)\} = \frac{1}{2}\sigma_n^2\mathbf{I}_{N_b} \quad \text{n} = 1, ..., M. \tag{C.5}$$

Finally, it is assumed that $\mathbf{s}(n)$, n = 1, ..., M, are i.i.d., $\mathbf{n}(n)$, n = 1, ..., M, are i.i.d., and $\mathbf{s}(n)$ and $\mathbf{n}(n)$ are statistically independent, n = 1, ...M.

The real part of the beamspace sample covariance matrix may be expressed in terms of the real and imaginary parts of each beamspace snapshot vector as

$$\mathcal{R}e\{\hat{\mathbf{R}}_y\} = \mathcal{R}e\left\{\frac{1}{M}\sum_{n=1}^{M}(\mathbf{y}_r(n) + j\mathbf{y}_i(n))(\mathbf{y}_r(n) - j\mathbf{y}_i(n))^T\right\} \qquad [C.6]$$

$$= \frac{1}{M}\sum_{n=1}^{M}\mathbf{y}_r(n)\mathbf{y}_r^T(n) + \frac{1}{M}\sum_{n=1}^{M}\mathbf{y}_i(n)\mathbf{y}_i^T(n)$$

where, exploiting the fact that B is real-valued, $\mathbf{y}_r(n)$ and $\mathbf{y}_i(n)$ may be expressed as

$$\mathbf{y}_r(n) = \mathcal{R}e\{\mathbf{y}(n)\} = \mathbf{B}\mathbf{s}_r(n) + \mathbf{n}_r(n) \qquad [C.7]$$

$$\mathbf{y}_i(n) = \mathcal{I}m\{\mathbf{y}(n)\} = \mathbf{B}\mathbf{s}_i(n) + \mathbf{n}_i(n). \qquad [C.8]$$

It follows from previous assumptions that $\mathbf{y}_r(n)$ and $\mathbf{y}_i(n)$ are i.i.d. with

$$\mathcal{E}\{\mathbf{y}_r(n)\mathbf{y}_r^T(n)\} = \mathcal{E}\{\mathbf{y}_i(n)\mathbf{y}_i^T(n)\} = \frac{1}{2}\mathbf{B}\mathbf{P}_S\mathbf{B}^T + \frac{1}{2}\sigma_n^2\mathbf{I}_{N_b} = \frac{1}{2}\mathbf{R}_y \quad n = 1, ..., M. \qquad [C.9]$$

Now, in accordance with (C.6) $M\,\mathcal{R}e\{\hat{\mathbf{R}}_y\}$ may be expressed as $\sum_{n=1}^{2M} z(n)z^T(n)$ where $\mathbf{z}(n) = \mathbf{y}_r(n)$, n=1,...,M, and $\mathbf{z}(M + n) = \mathbf{y}_i(n)$, n=1,...,M. From (C.7), (C.8), and (C.9), $\mathbf{z}(n)$ are independent and identically distributed as $\mathcal{N}(\mathbf{0}, 1/2\mathbf{R}_y)$, where $\mathcal{N}(\mu, B)$ denotes the multivariate Gaussian distribution with mean vector μ and covariance matrix B. It follows then that $M\,\mathcal{R}e\{\hat{\mathbf{R}}_y\}$ is Wishart distributed with 2M degrees of freedom. This is in contrast to $M\,\hat{\mathbf{R}}_y$ which is complex Wishart distributed with M degrees of freedom.

Appendix D: Derivation of the Asymptotic Distribution of the Signal Subspace Eigenvalues/Eigenvectors

Here the asymptotic distribution of the signal subspace eigenvalues and corresponding eigenvectors of the real part of the sample covariance matrix are derived. The performance prediction of eigenstructure direction of arrival algorithms based upon the Wishart distribution of the sample covariance matrix first appeared in [21], adapting tools from the statistical community, e.g., [44]. As is different in the case at hand, the real part of the beamspace sample covariance matrix is not Wishart distributed, but the analysis follows closely to the case of element-space processing in conjunction with a single forward/backward average as reported in [8]. Although there is a direct relationship between the sample covariance matrices obtained by taking the real part in beamspace and that obtained with a single forward-backward average in element-space, the results in [8] cannot be manipulated to apply here - there is no one-to-one relationship between the signal subspace eigenvectors in the two methodologies. It can be shown that a relationship does exist between the signal subspace eigenvectors, however, when the beamforming preprocessor is a full-rank, N x N matrix; but we focus on the use of beamforming architectures that transform the element-space data to a lower dimensional space. Presented here is an outline of the derivation regarding the distribution of the signal subspace eigenvectors.

As defined in the text, the real part of the true beamspace covariance matrix is spectrally decomposed as

$$\mathcal{R}e\{\mathbf{R}_y\} = \mathbf{B}\,\mathcal{R}e\{\mathbf{P}_S\}\,\mathbf{B}^T + \sigma_n^2\mathbf{I} = \mathbf{E}\boldsymbol{\Lambda}\mathbf{E}^T \qquad [D.1]$$

where

$$\mathbf{E} = [\,\mathbf{e}_1 \vdots \mathbf{e}_2 \vdots \ldots \vdots \mathbf{e}_{N_b}\,] \qquad N_b \text{ x } N_b,$$

$$\boldsymbol{\Lambda} = diag(\,\lambda_1,\,\lambda_2,\,\ldots,\,\lambda_{N_b}\,), \quad \text{and}$$

$$\lambda_1 > \lambda_2 > \ldots > \lambda_K > \lambda_{K+1} = \lambda_{K+2} = \ldots = \lambda_{N_b}.$$

Knowledge of the signal/noise subspace needed for the MUSIC prescription is derived from the real part of the sample beamspace covariance matrix

$$\mathcal{R}e\{\hat{\mathbf{R}}_y\} = \mathcal{R}e\left\{\frac{1}{M}\sum_{m=1}^{M}\mathbf{y}(m)\mathbf{y}^H(m)\right\}$$

$$= \frac{1}{2M}\sum_{m=1}^{M}\left[\,\mathbf{y}(m)\mathbf{y}^H(m) + (\mathbf{y}(m)\mathbf{y}^H(m))^*\,\right] = \hat{\mathbf{E}}\hat{\boldsymbol{\Lambda}}\hat{\mathbf{E}}^T \qquad [D.2]$$

where

$$\mathbf{E} = [\,\hat{\mathbf{e}}_1 \vdots \hat{\mathbf{e}}_2 \vdots \ldots \hat{\mathbf{e}}_{N_b}\,],$$

$$\hat{\boldsymbol{\Lambda}} = diag(\,\hat{\lambda}_1,\,\hat{\lambda}_2,\,\ldots,\,\hat{\lambda}_{N_b}\,), \quad \text{and}$$

$$\hat{\lambda}_1 > \lambda_2 > \ldots > \hat{\lambda}_K > \hat{\lambda}_{K+1} > \ldots > \hat{\lambda}_{N_b}.$$

As before, all estimated quantities originating from the sample covariance matrix are denoted with a "^". Recall that the choice of the eigenvectors is riot unique; the noise-only subspace is characterized by repeated eigenvalues so that the set of noise eigenvectors simply need to span the particular subspace while the eigenvectors corresporiding to the unique signal subspace eigenvalues may be multiplied by some unit magnitude scalar to maintain the unit length constraint. Here we will work with real-valued eigenvectors and need only, for a unique specification of the desired end result, stipulate that the eigenvectors satisfy a diagonal entry constraint

$$\mathbf{e}_{ii}, \quad \mathbf{Y}_{ii} > 0 \quad \text{where} \quad \mathrm{Y} = \mathbf{E}^T\hat{\mathbf{E}}. \qquad [D.3]$$

The asymptotic distribution of the eigenstatistics will be found to be completely expressible in terms of the elements of the mean and covariance of the matrix

$$\mathbf{U} = \sqrt{M}(\mathbf{T} - \boldsymbol{\Lambda}) \qquad [D.4]$$

where

$$\mathrm{T} = \mathbf{E}^T\,\mathcal{R}e\{\hat{\mathbf{R}}_y\}\,\mathrm{E} = \mathbf{E}^T\hat{\mathbf{E}}\hat{\boldsymbol{\Lambda}}\hat{\mathbf{E}}^T\mathbf{E} = \mathbf{Y}^T\hat{\boldsymbol{\Lambda}}\mathbf{Y}^T. \qquad [D.5]$$

The matrix E diagonalizes $\mathcal{R}e\{\mathbf{R}_y\}$ to $\boldsymbol{\Lambda}$ as in (D.l). Thus U essentially represents an error matrix driven by the finite sample estimate of the covariance when operated

on by E. Substitution of (D.2) leads to

$$\mathbf{U} = \frac{1}{2\sqrt{M}} \left(\sum_{m=1}^{M} \mathbf{z}(m)\mathbf{z}^H(m) + (\mathbf{z}(m)\mathbf{z}^H(m))^* \right) - \sqrt{M}\boldsymbol{\Lambda} \qquad [D.6]$$

where

$$\mathbf{z}(m) = \mathbf{E}^T\mathbf{y}(m), \quad \mathbf{z}^*(m) = \mathbf{E}^T\mathbf{y}^*(m) \quad \in \mathcal{C}^N.$$

The signal amplitude and noise processes are assumed to spatially and temporally independent and governed by zero-mean circular Gaussian random processes, hence $\mathbf{z}(m)$ and $\mathbf{z}^*(m)$ are zero-mean Gaussian processes with covariance E^TR,E and $\mathbf{E}^T\mathbf{R}_y^*\mathbf{E}$, respectively. Direct application of the central limit theorem suggests that the limiting distribution of the elements of U are normal. The mean of U is easily shown to be zero. As as result of the independency from snapshot to snapshot, we have

$$\mathcal{E}\{\mathbf{u}_{ij}\mathbf{u}_{k\ell}^*\} = \frac{1}{4M} \sum_{m=1}^{M} \Big[\mathcal{E}\{\mathbf{z}_i(m)\mathbf{z}_j^*(m)\mathbf{z}_k(m)\mathbf{z}_\ell^*(m)\} + \mathcal{E}\{\mathbf{z}_i(m)\mathbf{z}_j^*(m)\mathbf{z}_k^*(m)\mathbf{z}_\ell(m)\} + \mathcal{E}\{\mathbf{z}_i^*(m)\mathbf{z}_j(m)\mathbf{z}_k(m)\mathbf{z}_\ell^*(m)\} + \mathcal{E}\{\mathbf{z}_i^*(m)\mathbf{z}_j(m)\mathbf{z}_k^*(m)\mathbf{z}_\ell(m)\} \Big] - \lambda_i\lambda_k\delta_{ij}\delta_{k\ell} \qquad [D.7]$$

Through the use of the gaussian expansion of four zero-mean jointly gaussian variables $\mathbf{x}_i$, $i = 1 - 4$,

$$\mathcal{E}\{\mathbf{x}_1\mathbf{x}_2\mathbf{x}_3\mathbf{x}_4\} = \mathcal{E}\{\mathbf{x}_1\mathbf{x}_2\}\mathcal{E}\{\mathbf{x}_3\mathbf{x}_4\} + \mathcal{E}\{\mathbf{x}_1\mathbf{x}_3\}\mathcal{E}\{\mathbf{x}_2\mathbf{x}_4\} + \mathcal{E}\{\mathbf{x}_1\mathbf{x}_4\}\mathcal{E}\{\mathbf{x}_2\mathbf{x}_3\},$$

and the relations

$$\mathcal{E}\{\mathbf{z}_p(m)\mathbf{z}_q^*(m)\} = \mathbf{e}_p^T\mathbf{R}_y\mathbf{e}_q = \mathbf{e}_q^T\mathbf{R}_y^*\mathbf{e}_p$$

$$\mathcal{E}\{\mathbf{z}_p(m)\mathbf{z}_q(m)\} = \mathbf{0} \quad \forall p, q$$

one obtains, after simplification,

$$\mathcal{E}\{\mathbf{u}_{ij}\mathbf{u}_{k\ell}^*\} = \frac{1}{2}\mathcal{R}e\{ (\mathbf{e}_i^T\mathbf{R}_y\mathbf{e}_\ell)(\mathbf{e}_j^T\mathbf{R}_y^*\mathbf{e}_k) \} + \frac{1}{2}\mathcal{R}e\{ (\mathbf{e}_i^T\mathbf{R}_y\mathbf{e}_k)(\mathbf{e}_j^T\mathbf{R}_y^*\mathbf{e}_\ell) \} \doteq \Gamma_{ij\ell k} \quad [D.8]$$

Notice that the signal subspace eigenvectors of the complex covariance $\mathbf{R}_y$ as well as those of only the real part, $\mathcal{R}e\{\mathbf{R}_y\}$, span the same space, namely, the subspace

spanned by the columns of B. Thus we have

$$\mathbf{e}_i^T \mathbf{R}_y \mathbf{e}_j = 0, \quad i \leq K,\ j > K.$$

Making use of this property as well as the orthogonality of the noise eigenvectors suggests that

$$\mathbf{e}_k^T \mathbf{R}_y \mathbf{e}_i = \lambda_k \delta_{ik} + j\, \mathbf{e}_k^T \mathbf{R}_I \mathbf{e}_i (1 - \delta_{ik})$$

where $\mathbf{R}_I = \mathcal{I}m\{\mathbf{R}_y\}$, leading to

$$\Gamma_{ij\ell k} = \frac{1}{2} \left\{ \lambda_k \lambda_\ell \delta_{kj} \delta_{\ell i} + \lambda_k \lambda_\ell \delta_{ki} \delta_{\ell j} + (\mathbf{e}_k^T \mathbf{R}_I \mathbf{e}_j)(\mathbf{e}_\ell^T \mathbf{R}_I \mathbf{e}_i)(1 - \delta_{kj})(1 - \delta_{\ell i}) + (\mathbf{e}_k^T \mathbf{R}_I \mathbf{e}_i)(\mathbf{e}_\ell^T \mathbf{R}_I \mathbf{e}_j)(1 - \delta_{ki})(1 - \delta_{\ell j}) \right\} \quad [D.9]$$

Notice that the terms involving the imaginary part of the beamspace covariance matrix, $\mathbf{R}_I$, represent the only structural difference to that found in the complex processing case as studied in [21, 33, 34].

The ultimate goal is to relate the mean and variance of the eigenvalues and eigenvectors of the sample covariance matrix to the elements of U. The taken approach is to define the first order perturbation of Y in W as

$$\mathbf{Y} = \mathbf{I}_{N_b} + \frac{1}{\sqrt{M}} \mathbf{W}. \quad [D.10]$$

As we are only allowed to determine the perturbation in the eigenquantities related to the non-repeated eigenvalues in the signal subspace, we partition the various matrices as

$$\mathbf{\Lambda} = \begin{bmatrix} \mathbf{\Lambda}_1 & \mathbf{0} \\ \mathbf{0} & \sigma_n^2 \mathbf{I}_{N_b - K} \end{bmatrix}, \quad \mathbf{U} = \begin{bmatrix} \mathbf{U}_{11} & \mathbf{U}_{12} \\ \mathbf{U}_{21} & \mathbf{U}_{22} \end{bmatrix}, \quad \text{and}$$

$$\mathbf{W} = \begin{bmatrix} \mathbf{W}_{11} & \mathbf{W}_{12} \\ \mathbf{W}_{21} & \mathbf{W}_{22} \end{bmatrix}.$$

The partitioning of these matrices are such that the dimension of the upper left hand elements is that of the signal subspace, namely K. As a result we see that,

$$\mathbf{Y} = \begin{bmatrix} \mathbf{Y}_{11} & \mathbf{Y}_{12} \\ \mathbf{Y}_{21} & \mathbf{Y}_{22} \end{bmatrix} = \begin{bmatrix} \mathbf{I}_K + \frac{1}{\sqrt{M}} \mathbf{W}_{11} & \frac{1}{\sqrt{M}} \mathbf{W}_{12} \\ \frac{1}{\sqrt{M}} \mathbf{W}_{21} & \mathbf{Y}_{22} \end{bmatrix} \quad [D.11]$$

The derivation of the statistics of the sample-based eigenvalues and eigenvectors is accomplished in two parts. The first involves equating the first order perturbation terms in T via (D.4), (D.5), and (D.11) as

$$\mathbf{T} = \begin{bmatrix} \boldsymbol{\Lambda}_1 + \frac{1}{\sqrt{M}}\mathbf{U}_{11} & \frac{1}{\sqrt{M}}\mathbf{U}_{12} \\ \frac{1}{\sqrt{M}}\mathbf{U}_{21} & \sigma_n^2\mathbf{I}_{N_b-K} + \frac{1}{\sqrt{M}}\mathbf{U}_{22} \end{bmatrix} = \begin{bmatrix} \boldsymbol{\Lambda}_1 & \mathbf{0} \\ \mathbf{0} & \sigma_n^2\mathbf{Y}_{22}\mathbf{Y}_{22}^T \end{bmatrix} +$$

$$\frac{1}{\sqrt{M}} \begin{bmatrix} \boldsymbol{\Lambda}_1\mathbf{W}_{11}^T + \sqrt{M}\,\Delta\boldsymbol{\Lambda}_1 + \mathbf{W}_{11}\boldsymbol{\Lambda}_1 & \boldsymbol{\Lambda}_1\mathbf{W}_{12}^T + \sigma_n^2\mathbf{W}_{12}\mathbf{Y}_{22}^T \\ \mathbf{W}_{21}\boldsymbol{\Lambda}_1 + \sigma_n^2\mathbf{Y}_{22}\mathbf{W}_{12}^T & \sqrt{M}\,\mathbf{Y}_{22}\Delta\boldsymbol{\Lambda}_2\,\mathbf{Y}_{22}^T \end{bmatrix} + o(\frac{1}{\sqrt{M}}), \quad [D.12]$$

where $\Delta\boldsymbol{\Lambda}_i = \hat{\boldsymbol{\Lambda}}_i - \mathrm{A};,\ _2 = 1,2$ and $o(\frac{1}{\sqrt{M}})$ represents those terms of order less than $\sqrt{M}$. Equating the upper- and bottom-left hand partitioned terms and discarding the higher order terms leads to

$$\mathbf{U}_{11} = \boldsymbol{\Lambda}_1\mathbf{W}_{11}^T + \sqrt{M}\,\Delta\boldsymbol{\Lambda}_1 + \mathbf{W}_{11}\boldsymbol{\Lambda}_1, \quad \text{and} \quad [D.13]$$

$$\mathbf{U}_{21} = \mathbf{W}_{21}\boldsymbol{\Lambda}_1 + \sigma_n^2\mathbf{Y}_{22}\mathbf{W}_{12}^T \quad [D.14]$$

Additional asymptotic relations are obtained through

$$\mathbf{I}_{N_b} = \mathbf{Y}\mathbf{Y}^T = \begin{bmatrix} \mathbf{I}_K & \mathbf{0} \\ \mathbf{0} & \mathbf{Y}_{22}\mathbf{Y}_{22}^T \end{bmatrix} + \frac{1}{\sqrt{M}} \begin{bmatrix} \mathbf{W}_{11}^T + \mathbf{W}_{11} & \mathbf{W}_{21}^T \\ \mathbf{W}_{21} + \mathbf{Y}_{22}\mathbf{W}_{12}^T & \mathbf{0} \end{bmatrix} + o(\frac{1}{\sqrt{M}}), \quad [D.15]$$

leading to

$$\mathbf{W}_{11} + \mathbf{W}_{11}^T = \mathbf{0} \quad [D.16]$$

$$\mathbf{W}_{21} + \mathbf{Y}_{22}\mathbf{W}_{12}^T = \mathbf{0} \quad [D.17]$$

Assembling equations (D.13), (D.14), (D.16), and (D.17) yields

$$\sqrt{M}\,\Delta\lambda_i = \sqrt{M}\,(\hat{\lambda}_i - \lambda_i) = \mathbf{u}_{ii} \quad \text{for } i = 1,2,\ldots,K, \quad \text{and} \quad [D.18]$$

$$\mathbf{w}_{ij} = \begin{cases} 0 & i = 1,\ldots,K \quad j = i \\ \frac{\mathbf{u}_{ij}}{\lambda_j - \lambda_i} & i,\ j = 1,\ldots,K \quad i \neq j \\ \frac{\mathbf{u}_{ij}}{\lambda_j - \sigma_n^2} = \mathbf{w}_{ji}^* & i = K+1,\ldots,N_b \quad j = 1,\ldots,K \end{cases} \quad [D.19]$$

With the aid of (D.18), the asymptotic bias of the error in the signal eigenvalues is shown to be zero to order $\frac{1}{\sqrt{M}}$, i.e., $\mathrm{E}\{\hat{\lambda}_i - \lambda_i\} = o(\frac{1}{\sqrt{M}})$, $i = 1,\ldots,\mathrm{K}$, while the associated covariance is

$$\begin{aligned} \mathcal{AE}\{M\,\Delta\lambda_i\Delta\lambda_j\} &= \Gamma_{ijji} \\ &= \frac{1}{2}\left\{\lambda_i\lambda_j(1+\delta_{ij}) - |\,\mathbf{e}_i^T\mathbf{R}_I\mathbf{e}_j|^2\right\}. \end{aligned} \qquad [D.20]$$

Notice that

$$\sqrt{M}\,\Delta\mathbf{E} = \sqrt{M}\,[\,\hat{\mathbf{E}} - \mathbf{E}\,] = \sqrt{M}\mathbf{E}\,[\,\mathbf{Y} - \mathbf{I}\,] = \mathbf{E}\mathbf{W}, \qquad [D.21]$$

so that

$$\hat{\mathbf{e}}_i = \mathbf{e}_i + \frac{1}{\sqrt{M}}\sum_{\substack{j=1\\ j\neq i}}^{N_b} \mathbf{w}_{ji}\mathbf{e}_j. \qquad [D.22]$$

Accounting for the orthogonality of the eigenvectors by dividing (D.22) by $|\,\hat{\mathbf{e}}_i\,|$ and finding the associated mean and covariance yields, after simplification,

$$\begin{aligned} \mathcal{AE}\{M\,\Delta\mathbf{e}_i\} &= -\frac{1}{2}\sum_{\substack{k=1\\ k\neq i}}^{N_b} \frac{\Gamma_{kkii}}{(\lambda_i - \lambda_k)^2}\,\mathbf{e}_i \\ &= \frac{1}{2}\sum_{\substack{k=1\\ k\neq i}}^{N_b} \frac{|\,\mathbf{e}_i^T\mathbf{R}_I\mathbf{e}_k\,|^2}{(\lambda_i - \lambda_k)^2}\,\mathbf{e}_i, \quad \text{and} \end{aligned} \qquad [D.23]$$

$$\mathcal{AE}\{M\,\Delta\mathbf{e}_i\Delta\mathbf{e}_j^T\} = \sum_{\substack{k=1\\ k\neq i}}^{N_b}\sum_{\substack{\ell=1\\ \ell\neq j}}^{N_b} \frac{\Gamma_{k\ell ji}}{(\lambda_i - \lambda_k)(\lambda_j - \lambda_\ell)}\,\mathbf{e}_k\mathbf{e}_\ell^T \qquad [D.24]$$

$$= \frac{\delta_{ij}}{2}\left\{\sum_{\substack{k=1\\ k\neq i=j}}^{N_b} \frac{\lambda_k\lambda_i\,\mathbf{e}_k\mathbf{e}_i^T}{(\lambda_i - \lambda_k)^2} + \sum_{\substack{k=1\\ k\neq i,j}}^{K}\sum_{\substack{\ell=1\\ \ell\neq i,j}}^{K} \frac{(\mathbf{e}_k^T\mathbf{R}_I\mathbf{e}_j)(\mathbf{e}_i^T\mathbf{R}_I\mathbf{e}_\ell)}{(\lambda_i - \lambda_k)(\lambda_j - \lambda_\ell)}\mathbf{e}_k\mathbf{e}_\ell^T\right\}$$

$$+ \frac{(1-\delta_{ij})}{2}\left\{\frac{-\lambda_i\lambda_j\,\mathbf{e}_j\mathbf{e}_i^T}{(\lambda_i - \lambda_j)^2} + \sum_{\substack{k=1\\ k\neq i}}^{K}\sum_{\substack{\ell=1\\ \ell\neq j,k}}^{K} \frac{(\mathbf{e}_i^T\mathbf{R}_I\mathbf{e}_j)(\mathbf{e}_k^T\mathbf{R}_I\mathbf{e}_\ell)}{(\lambda_i - \lambda_k)(\lambda_j - \lambda_\ell)}\mathbf{e}_k\mathbf{e}_\ell^T\right\}$$

Appendix E: Asymptotic Variance of ESPRIT Formulation

Given that z_i is a (signal) unit-magnitude eigenvalue of the matrix

$$\mathbf{F} = (\mathbf{\Gamma}_1\mathbf{E}_{Z_s})^{\dagger}(\mathbf{\Gamma}_2\mathbf{E}_{Z_s}) = [(\mathbf{\Gamma}_1\mathbf{E}_{Z_s})^H(\mathbf{\Gamma}_1\mathbf{E}_{Z_s})]^{\dagger}(\mathbf{\Gamma}_1\mathbf{E}_{Z_s})^H(\mathbf{\Gamma}_2\mathbf{E}_{Z_s}), \qquad [E.1]$$

with $\mathbf{x}_i$ and $\mathbf{q}_i$ the corresponding right and left eigenvectors, Rao and Hari [42] showed that, to $o(M^{-1})$,

$$\Delta z_i = \mathbf{q}_i^H \Delta\mathbf{F}\,\mathbf{x}_i. \qquad [E.2]$$

The error in $\mathbf{F}$, $\Delta\mathbf{F}$, due to the finite sample estimation of the beamspace covariance matrix is

$$\mathrm{A}\,\mathrm{F} = (\mathbf{\Gamma}_1\mathbf{E}_{Z_s})^{\dagger}(\mathbf{\Gamma}_2\Delta\mathbf{E}_{Z_s}) - (\mathbf{\Gamma}_1\mathbf{E}_{Z_s})^{\dagger}(\mathbf{\Gamma}_1\Delta\mathbf{E}_{Z_s})\mathbf{F}, \qquad [E.3]$$

which is applicable to either the Least Squares (LS) or Total Least Squares (TLS) versions of ESPRIT. Substituting the form of $\Delta\mathbf{E}_{Z_s}$ in equation (4.27) into equation (E.2), one obtains

$$\mathcal{E}\{\,|\Delta z_i|^2\,\} = \boldsymbol{\alpha}_i^H \left[\sum_{k=1}^{K}\sum_{\ell=1}^{K} x_i(k)\,x_i^*(\ell)\,\mathcal{E}\{\Delta\mathbf{e}_k\,\Delta\mathbf{e}_\ell^T\}\right]\boldsymbol{\alpha}_i \qquad [E.4]$$

$$(z_i^*)^2\mathcal{E}\{\,(\Delta z_i)^2\,\} = \boldsymbol{\alpha}_i^H \left[\sum_{k=1}^{K}\sum_{\ell=1}^{K} x_i(k)\,x_i(\ell)\,\mathcal{E}\{\Delta\mathbf{e}_k\,\Delta\mathbf{e}_\ell^T\}\right]\boldsymbol{\alpha}_i^*, \qquad [E.5]$$

where $\boldsymbol{\alpha}_i$ and the signal eigenvector error statistics were stated in equations (4.29) and (4.22), respectively. Following [42], these quantities are then substituted into

$$\mathcal{E}\{\,(\Delta\theta_i)^2\,\} = \left[\frac{\lambda}{2\pi dD\cos\theta_i}\right]^2 \left[\frac{\mathcal{E}\{\,|\Delta z_i|^2\,\} - \mathrm{Re}\{\,(z_i^*)^2\,\mathcal{E}\{\,(\Delta z_i)^2\,\}\}}{2}\right]. \qquad [E.6]$$

to yield the desired theoretical asymptotic estimation variance.

In the case of uncorrelated signals, the asymptotic error in the signal subspace eigenvectors reduces to

$$\mathcal{E}\{\,\Delta\mathbf{e}_k\,\Delta\mathbf{e}_\ell^T\,\} = \frac{\delta_{k\ell}}{2M}\sum_{\substack{m=1\\ m\neq k}}^{N_b}\frac{\lambda_k\lambda_m}{(\lambda_k-\lambda_m)^2}\,\mathbf{e}_m\mathbf{e}_m^T - \frac{(1-\delta_{k\ell})}{2M}\frac{\lambda_k\lambda_\ell}{(\lambda_k-\lambda_\ell)^2}\,\mathbf{e}_\ell\mathbf{e}_k^T. \qquad [E.7]$$

After substituting and simplifying, the asymptotic variance of the ESPRIT angle estimate for uncorrelated sources reduces to

$$\begin{aligned}\mathcal{E}\{(\Delta\theta_i)^2\} &= \left[\frac{\lambda}{2\pi dD\cos\theta_i}\right]^2 \frac{1}{2M}\left[\sum_{k=1}^{K}\frac{\sigma_n^2\lambda_k}{(\lambda_k-\sigma_n^2)^2}\left|\mathrm{Im}\left\{x_i(k)\mathbf{E}_n^T\boldsymbol{\alpha}_i\right\}\right|^2\right. \\ &+ \sum_{k=1}^{K}\sum_{\substack{\ell=1\\ \ell\neq k}}^{K}\frac{\lambda_k\lambda_\ell}{(\lambda_k-\lambda_\ell)^2}\left(\mathrm{Im}\left\{x_i(\ell)\mathbf{e}_k^T\boldsymbol{\alpha}_i\right\}^2\right. \\ &- \left.\left.\mathrm{Im}\left\{x_i(\ell)\mathbf{e}_\ell^T\boldsymbol{\alpha}_i\right\}\mathrm{Im}\left\{x_i(k)\mathbf{e}_k^T\boldsymbol{\alpha}_i\right\}\right)\right], \qquad \text{[E.8]}\end{aligned}$$

where $\mathbf{E}_n$ is an $N_b \times (N_b - K)$ matrix composed of the noise eigenvectors associated with the ideal beamspace covariance.